

July 2018

Synthesis and Characterization of Alpha-Hematite Nanomaterials for Water-Splitting Applications

Hussein Alrobei

University of South Florida, alrobei@mail.usf.edu

Follow this and additional works at: <https://scholarcommons.usf.edu/etd>



Part of the [Mechanical Engineering Commons](#)

Scholar Commons Citation

Alrobei, Hussein, "Synthesis and Characterization of Alpha-Hematite Nanomaterials for Water-Splitting Applications" (2018).
Graduate Theses and Dissertations.
<https://scholarcommons.usf.edu/etd/7661>

This Dissertation is brought to you for free and open access by the Graduate School at Scholar Commons. It has been accepted for inclusion in Graduate Theses and Dissertations by an authorized administrator of Scholar Commons. For more information, please contact scholarcommons@usf.edu.

Synthesis and Characterization of Alpha-Hematite Nanomaterials for Water-Splitting
Applications

by

Hussein Alrobei

A dissertation submitted in partial fulfillment
of the requirements for the degree of
Doctor of Philosophy
Department of Mechanical Engineering
College of Engineering
University of South Florida

Co-Major Professor: Ashok Kumar, Ph.D.
Co-Major Professor: Manoj Ram, Ph.D.
Arash Takshi, Ph.D.
Ajit Mujumdar, Ph.D.
Jiangfeng Zhou, Ph.D.

Date of Approval:
June 26, 2018

Keywords: photoelectrochemical, hematite (α -Fe₂O₃), MoS₂, TiO₂, nanocomposite

Copyright © 2018, Hussein Alrobei

DEDICATION

I would like to dedicate this work to my parents, Saad Alrobei and Nashta Alqahtani, and to my wife and kids who have supported me from the very beginning. I would like to thank them for all the effort, support, and love they have given to me. Finally, this work is also dedicated to my home country, Saudi Arabia, for their generous financial support.

ACKNOWLEDGMENTS

I would like to thank Dr. Ashok Kumar for allowing me to work with him as a Ph.D. student. I also worked with him as a TA for various courses: Advanced Materials, Characterization of Materials, and Micro and Nano-manufacturing. In each capacity, as a student and TA, he taught me how to navigate academia. Additionally, I owe sincere gratitude to Dr. Manoj Ram; I am extremely lucky that I had the chance to work with him. I gained immeasurable information personally and scientifically that helped me in my dissertation and in my future endeavor. I would like to thank all professors who taught me throughout my studying, master and Ph.D. courses, at USF as well as all staff in the Mechanical Engineering Department at USF beginning with Dr. Rajiv Dubey, department chair. I am grateful to Dr. Dubey for his financial support that allowed me to present my work at two different conferences. Dr. Rasim Guldiken, a graduate advisor, deserves a special thanks for his dedication to giving graduate students the best instructions and advices. I would also like to thank my committee members Dr. Arash Takshi, Dr. Ajit Mujumdar, and Dr. Jiangfeng Zhou for accepting my request to become committee members and allocating time from their busy schedules to attend my dissertation defense. Many thanks go also the College of Engineering for paying one-year tuition for my NREC training so that I could work on XRD, SEM, and TEM instruments. I had the opportunity to interact with all staff at NREC and it is my pleasure to say thank you for the knowledge and information that I gained through my training. I owe special thanks to my friends Turkey Alamro and Micheal Miccory in the lab who did most of my measurements in the beginning of my research. I would also like to thank the USF president, vice president, all administration employees, professors, and students for everything that I received

in my time here, starting from respect, knowledge, and love. I spent nearly six years at USF, which will remain in my heart. I do not remember one day that me nor my family felt unwelcome due to the positive environment in Tampa Bay and especially at USF.

TABLE OF CONTENTS

LIST OF TABLES	iv
LIST OF FIGURES	v
ABSTRACT.....	ix
CHAPTER 1: INTRODUCTION.....	1
1.1 Problem Description and Motivation.....	1
1.2 Organization of The Dissertation.....	2
CHAPTER 2: LITERATURE REVIEW	5
2.1 Introduction.....	5
2.2 Methods of Hydrogen Production.....	6
2.3 Hydrogen Production by Photoelectrochemical Cells (PEC).....	7
2.4 Mechanism of Photoelectrochemical Cells (PEC).....	9
2.5 Photocatalytic Materials.....	11
2.5.1 Cadmium Sulfide (CdS).....	13
2.5.2 Zinc Oxide (ZnO)	13
2.6 Alpha-Hematite (α -Fe ₂ O ₃).....	14
2.6.1 Introduction and Properties.....	14
2.6.2 Characterization	14
2.6.2.1 X-Ray Diffraction (XRD).....	14
2.6.2.2 Fourier Transform Infrared Spectroscopy (FTIR)	15
2.6.2.3 Scanning Electron Microscopy (SEM)	15
2.6.2.4 Transmission Electron Microscopy (TEM)	16
2.7 Enhanced Water Splitting in α -Hematite	17
2.7.1 Modification Structure	17
2.7.1.1 Nanotube (NTAs) and Nanorod (NRA) Structure	18
2.7.1.2 Nanowire Structure	18
2.7.2 Doping.....	19
2.8 Applications of α -Hematite Photoconduction Material	21
2.8.1 Sensing.....	21
2.8.2 Photovoltaic Cells (PV)	21
2.8.3 Fuel Cell Production	22
2.8.4 Water Purification.....	22
2.8.5 Lithium Batteries	22
2.8.6 Supercapacitor.....	23
2.8.7 Corrosion Resistance	24
2.9 Conclusion	24

CHAPTER 3: ALUMINUM - α -HEMATITE THIN FILMS FOR PHOTOELECTROCHEMICAL APPLICATIONS	26
3.1 Introduction.....	26
3.2 Experimental Details.....	27
3.2.1 Materials	27
3.2.2 Experimental Procedure.....	27
3.2.3 Film Formation of Substrate	29
3.3 Physical Properties Studies	29
3.3.1 UV-Visible Spectroscopy (UV-Vis).....	29
3.3.2 Scanning Electron Microscopy (SEM)	30
3.3.3 X-Ray Diffraction (XRD).....	31
3.3.4 Fourier Transform Infrared Spectroscopy (FTIR).....	32
3.4 Electrochemical Studies.....	33
3.4.1 Cyclic Voltammetry.....	33
3.4.2 Schematic of Hydrogen Production	36
3.5 Conclusion	37
 CHAPTER 4: MOLYBDENUM DISULFIDE α -HEMATITE- NANOCOMPOSITE FILMS FOR PHOTOELECTROCHEMICAL APPLICATIONS	39
4.1 Introduction.....	39
4.2 Experimental Details.....	41
4.2.1 Materials	41
4.2.2 Experimental Procedure.....	41
4.2.3 Film Formation of Substrate	43
4.3 Physical Properties Studies	43
4.3.1 UV-Visible Spectroscopy (UV-Vis).....	43
4.3.2 X-Ray Diffraction (XRD).....	44
4.3.3 Fourier Transform Infrared Spectroscopy (FTIR).....	45
4.3.4 Scanning Electron Microscopy (SEM)	47
4.3.5 Raman Spectroscopy.....	48
4.3.6 Particle Analyzer.....	49
4.4 Electrochemical Studies.....	50
4.4.1 Cyclic Voltammetry.....	50
4.4.2 Chronoamperometry	52
4.4.3 Half-Sweep Potential	53
4.4.4 Schematic of MoS ₂ - α -Fe ₂ O ₃ Reaction Process	54
4.5 Conclusion	55
 CHAPTER 5: P-N PHOTOELECTROCHEMICAL CELL PROPERTIES USING α -HEMATITE -MOLYBDENUM DISULFIDE AS N-ELECTRODE AND POLYHEXYLTHIOPHENE (RRPHTH) - NANODIAMOND (ND) AS P-ELECTRODE.....	56
5.1 Introduction.....	56
5.2 Experimental Details.....	58
5.2.1 Materials	58
5.2.2 Synthesis of Nanomaterials.....	58

5.2.3 Film Formation of Substrate	59
5.2.4 RRPHTH-ND/NaOH/MoS ₂ - α -Fe ₂ O ₃ -Based Photoelectrochemical Cells	59
5.3 Physical Properties Studies	60
5.3.1 Scanning Electron Microscopy (SEM)	60
5.3.2 Fourier Transform Infrared Spectroscopy (FTIR)	61
5.3.3 X-Ray Diffraction (XRD)	62
5.3.4 UV-Visible Spectroscopy (UV-Vis)	63
5.4 Electrochemical Studies	65
5.4.1 Schematic of P-N Configuration-Based Reaction Process	65
5.4.2 Cyclic Voltammetry	66
5.4.3 Chronoamperometry	67
5.5 Conclusion	69
CHAPTER 6: P-N BASED PHOTOELECTROCHEMICAL DEVICE FOR WATER- SPLITTING APPLICATION OF ALPHA-HEMATITE (α -Fe ₂ O ₃)-TITANIUM DIOXIDE (TiO ₂) AS N-ELECTRODE & POLYHEXYLTHIOPHENE (RRPHTH) - NANODIAMOND (ND) AS P-ELECTRODE	71
6.1 Introduction	71
6.2 Experimental Details	72
6.2.1 Materials	72
6.2.2 Synthesis of Nanomaterial	73
6.2.3 Film Formation of Substrate	73
6.3 Physical Properties Studies	74
6.3.1 UV-Visible Spectroscopy (UV-Vis)	74
6.3.2 Fourier Transform Infrared Spectroscopy (FTIR)	77
6.3.3 Raman Spectroscopy	79
6.3.4 Scanning Electron Microscopy (SEM)	81
6.4 Electrochemical Studies	82
6.4.1 Chronoamperometry	82
6.5 Conclusion	83
CHAPTER 7: CONCLUSION	84
7.1 Future Work	85
REFERENCES	87
APPENDIX A: COPYRIGHT PERMISSIONS FOR CHAPTERS 3, 4, AND 6	102
APPENDIX B: COPYRIGHT PERMISSIONS FOR FIGURES	105

LIST OF TABLES

Table 2.1 Different doping materials with alpha-hematite	20
Table 3.1 Amount of chemical used for synthesis of Al- α -Fe ₂ O ₃	28
Table 3.2 UV-vis peaks at nm for various percentages of Al in Al- α -Fe ₂ O ₃ nanomaterial	29
Table 3.3 X-ray diffraction for various percentages of Al in Al- α -Fe ₂ O ₃ nanomaterial	32
Table 4.1 Amount of chemical used for synthesis of MoS ₂ -composite α -hematite	42
Table 4.2 Infrared bands of each MoS ₂ doping to α -Fe ₂ O ₃	46
Table 5.1 Infrared bands of each α -Fe ₂ O ₃ , 0.1% MoS ₂ , and RRPHTTh-ND	62
Table 5.2 X-ray diffraction peaks of each α -Fe ₂ O ₃ , α -Fe ₂ O ₃ +0.1%MoS ₂	63
Table 5.3 UV-vis absorption peaks of each α -Fe ₂ O ₃ , α -Fe ₂ O ₃ +0.1%MoS ₂ , and RRPHTTh-ND	64
Table 6.1 Peaks of each α -Fe ₂ O ₃ -TiO ₂ nanomaterial dried at 300 °C.....	75
Table 6.2 Peaks of each α -Fe ₂ O ₃ -TiO ₂ nanomaterial dried at 500 °C.....	76
Table 6.3 Infrared bands of each α -Fe ₂ O ₃ -TiO ₂	78
Table 6.4 Peaks of each α -Fe ₂ O ₃ -TiO ₂	80

LIST OF FIGURES

Figure 2.1 Our greatest resources: sun and water	6
Figure 2.2 Schematic of hydrogen production using photocatalyst.....	7
Figure 2.3 Schematic of photoelectrochemical cells (PEC)	11
Figure 2.4 Band edge positions of semiconductor materials	12
Figure 2.5 X-ray diffraction pattern of α -Fe ₂ O ₃	14
Figure 2.6 FTIR spectra of α -Fe ₂ O ₃	15
Figure 2.7 SEM images of α -Fe ₂ O ₃	16
Figure 2.8 TEM images of α -Fe ₂ O ₃	16
Figure 2.9 SEM images of various concentrations of α -Fe ₂ O ₃	17
Figure 2.10 Schematic of SnO ₂ NRAs/ α -Fe ₂ O ₃ NTAs composite nanostructure.....	18
Figure 2.11 SEM images of iron wire surface after synthesis	19
Figure 2.12 Schematic of the NW growth in ambient air	19
Figure 2.13 Schematic for various doping materials (Ge, Si, Mn, Sn, Ti) in α -Fe ₂ O ₃	21
Figure 2.14 SEM images of FeO _x -C composite.....	23
Figure 2.15 (a) Schematic of the structure of the supercapacitor (b) CVs of the α -Fe ₂ O ₃ -PANI and PANI electrodes.....	24
Figure 3.1 Synthesized α -hematite (α -Fe ₂ O ₃) and Al- α -Fe ₂ O ₃ materials.....	28
Figure 3.2 UV-vis absorption spectra of Al- α -Fe ₂ O ₃	30
Figure 3.3 Scanning electron micrographs (SEM) of Al doped α -hematite.....	31
Figure 3.4 X-ray diffraction pattern of Al- α -Fe ₂ O ₃	32

Figure 3.5 FTIR spectra of Al- α -Fe ₂ O ₃	33
Figure 3.6 Cyclic voltammetry of Al- α -Fe ₂ O ₃ in 1M NaOH in three electrodes with platinum as reference and Ag/AgCl as reference electrode.....	34
Figure 3.7 Cyclic voltammetry of 20% Al- α - Fe ₂ O ₃ in 1M NaOH in three electrodes with platinum as reference and Ag/AgCl as reference electrode.....	35
Figure 3.8 Cyclic voltammetry of Al- α -Fe ₂ O ₃ with and without light in 1M NaOH in three electrodes with platinum as reference and Ag/AgCl as reference electrode	35
Figure 3.9 Variation of current (A) vs scan rate (V/sec) ^{1/2} for 20% Al- α - Fe ₂ O ₃ in 1M NaOH in three electrodes with platinum as reference and Ag/AgCl as reference electrode	36
Figure 3.10 Schematic of hydrogen production using Al- α -Fe ₂ O ₃ photocatalyst in 1M NaOH	37
Figure 4.1 Synthesized α -hematite (α -Fe ₂ O ₃) and MoS ₂ - α -Fe ₂ O ₃ composite materials	42
Figure 4.2 UV-vis absorption spectra of MoS ₂ with α -hematite nanocomposite.....	44
Figure 4.3 X-ray diffraction pattern of MoS ₂ with α -hematite nanocomposite	45
Figure 4.4 FTIR spectra of MoS ₂ with α -hematite nanocomposite.....	46
Figure 4.5 Scanning electron micrographs (SEM) of MoS ₂ with α -hematite nanocomposite	47
Figure 4.6 Raman spectra of MoS ₂ - α -Fe ₂ O ₃ film sample and ITO substrate with various percentages of MoS ₂ as shown in a and b.....	48
Figure 4.7 Particle size measurement of MoS ₂ - α -Fe ₂ O ₃ nanocomposite materials as a function of MoS ₂ dopant	50
Figure 4.8 Cyclic voltammetry of 1% MoS ₂ with α -Fe ₂ O ₃ nanocomposite without light in 1M NaOH in three electrodes with platinum as reference and Ag/AgCl as reference electrode.....	51
Figure 4.9 Cyclic voltammetry of 1% MoS ₂ with α -Fe ₂ O ₃ nanocomposite with light in 1M NaOH in three electrodes with platinum as reference and Ag/AgCl as reference electrode	52
Figure 4.10 Chronoamperometry photocurrent plot with t(s) ^{-1/2} for oxidation and reduction processes for MoS ₂ - α -Fe ₂ O ₃ film	53

Figure 4.11 Half-sweep potential with and without light for Al- α -Fe ₂ O ₃ and MoS ₂ - α -Fe ₂ O ₃ film with and without light exposure.....	54
Figure 4.12 Schematic of hydrogen production using MoS ₂ -composite α -Fe ₂ O ₃ photocatalyst in 1 M NaOH.....	55
Figure 5.1 Schematic of hydrogen production using MoS ₂ - α -Fe ₂ O ₃ nanocomposite as n-type and RRPHTH-ND as p-type photocatalyst in 1M NaOH	60
Figure 5.2 Scanning electron micrographs (SEM) of (a) α -Fe ₂ O ₃ , (b) α -Fe ₂ O ₃ +0.1%MoS ₂ , and (c) RRPHTH-ND	61
Figure 5.3 FTIR spectra of (a) α -Fe ₂ O ₃ , (b) α -Fe ₂ O ₃ +0.1%MoS ₂ , and (c) RRPHTH-ND.....	62
Figure 5.4 X-ray diffraction pattern of (a) α -Fe ₂ O ₃ , and (b) α -Fe ₂ O ₃ +0.1%MoS ₂	63
Figure 5.5 UV-vis absorption spectra of (a) α -Fe ₂ O ₃ , (b) α -Fe ₂ O ₃ +0.1%MoS ₂ , and (c) RRPHTH-ND	64
Figure 5.6 Schematic of water-splitting application in p-type RRPHTH-ND and n-type MoS ₂ -Fe ₂ O ₃ in water-based electrolyte photoelectrochemical cell under photoexcitation and under potential	65
Figure 5.7 Cyclic voltammetry study of p-type RRPHTH-ND and n-type MoS ₂ -Fe ₂ O ₃ in NaOH 1M-based electrolyte in photoelectrochemical cell with and without light.....	66
Figure 5.8 Current-transient study of p-type RRPHTH-ND and n-type 0.1% MoS ₂ - α -Fe ₂ O ₃ -based electrodes in 1M NaOH-based electrolyte in photoelectrochemical cell with and without light	67
Figure 5.9 Current-transient study of photoelectrochemical cell containing RRPHTH-ND as p-type electrode and 0.1, 0.2, 1, and 5% of MoS ₂ in MoS ₂ - α -Fe ₂ O ₃ as n-type electrode in 1M NaOH-based electrolyte with light switch on and off at applied potential of 1500 mV	68
Figure 5.10 Current-transient study of photoelectrochemical cell containing RRPHTH-ND as p-type electrode and 0.1, 0.2, 1, and 5% of MoS ₂ in MoS ₂ - α -Fe ₂ O ₃ as n-type electrode in 1M NaOH-based electrolyte.....	69
Figure 6.1 UV-vis absorption spectra of α -Fe ₂ O ₃ -TiO ₂ nanomaterials dried at 300 °C.....	76
Figure 6.2 UV-vis absorption spectra of α -Fe ₂ O ₃ -TiO ₂ nanomaterials dried at 500 °C.....	77
Figure 6.3 FTIR spectra of α -Fe ₂ O ₃ -TiO ₂ nanomaterials	79

Figure 6.4 Raman spectra of α -Fe ₂ O ₃ -TiO ₂ nanomaterials	80
Figure 6.5 SEM images of (a) α -Fe ₂ O ₃ (b) TiO ₂ (c) α -Fe ₂ O ₃ + 50% TiO ₂ (d) α -Fe ₂ O ₃ + 5% TiO ₂ (e) α -Fe ₂ O ₃ + 2.5% TiO ₂ dried at 500 °C.....	81
Figure 6.6 Photocurrent response for α -Fe ₂ O ₃ -TiO ₂ nanomaterial sample with 50% of TiO ₂ , heat treatment at 500 °C. (a) working electrode applied with 1000 mV of charge potential, (b) applied with 2000 mV of charge potential	82

ABSTRACT

The recent momentum in energy research has simplified converting solar to electrical energy through photoelectrochemical (PEC) cells. There are numerous benefits to these PEC cells, such as the inexpensive fabrication of thin film, reduction in absorption loss (due to transparent electrolyte), and a substantial increase in the energy conversion efficiency. Alpha-hematite (α - Fe_2O_3) has received considerable attention as a photoanode for water-splitting applications in photoelectrochemical (PEC) devices. The alpha-hematite (α - Fe_2O_3) nanomaterial is attractive due to its bandgap of 2.1eV allowing it to absorb visible light. Other benefits of α - Fe_2O_3 include low cost, chemical stability and availability in nature, and excellent photoelectrochemical (PEC) properties to split water into hydrogen and oxygen. However, α - Fe_2O_3 suffers from low conductivity, slow surface kinetics, and low carrier diffusion that causes degradation of PEC device performance. The low carrier diffusion of α -hematite is related to higher resistivity, slow surface kinetics, low electron mobility, and higher electro-hole combinations. All the drawbacks of α - Fe_2O_3 , such as low carrier mobility and electronic diffusion properties, can be enhanced by doping, which forms the nanocomposite and nanostructure films.

In this study, all nanomaterials were synthesized utilizing the sol-gel technique and investigated using Scanning Electron Microscopy (SEM), X-ray Diffractometer (XRD), UV-Visible Spectrophotometer (UV-Vis), Fourier Transform Infrared Spectroscopy (FTIR), Raman techniques, Particle Analyzer, Cyclic Voltammetry (CV), and Chronoamperometry, respectively. The surface morphology is studied by SEM. X-Ray diffractometer (XRD) is used to identify the crystalline phase and to estimate the crystalline size. FTIR is used to identify the chemical bonds

as well as functional groups in the compound. A UV-Vis absorption spectral study may assist in understanding electronic structure of the optical band gap of the material. Cyclic voltammetry and chronoamperometry were used to estimate the diffusion coefficient and study electrochemical activities at the electrode/electrolyte interface.

In this investigation, the α -Fe₂O₃ was doped with various materials such as metal oxide (aluminum, Al), dichalcogenide (molybdenum disulfide, MoS₂), and co-catalyst (titanium dioxide, TiO₂). By doping or composite formation with different percentage ratios (0.5, 10, 20, 30) of aluminum (Al) containing α -Fe₂O₃, the mobility and carrier diffusion properties of α -hematite (α -Fe₂O₃) can be enhanced. The new composite, Al- α -Fe₂O₃, improved charge transport properties through strain introduction in the lattice structure, thus increasing light absorption. The increase of Al contents in α -Fe₂O₃ shows clustering due to the denser formation of the Al- α -Fe₂O₃ particle. The presence of aluminum causes the change in structural and optical and morphological properties of Al- α -Fe₂O₃ more than the properties of the α -Fe₂O₃ photocatalyst. There is a marked variation in the bandgap from 2.1 to 2.4 eV. The structure of the composite formation Al- α -Fe₂O₃, due to a high percentage of Al, shows a rhombohedra structure. The photocurrent (35 μ A/cm²) clearly distinguishes the enhanced hydrogen production of the Al- α -Fe₂O₃ based photocatalyst.

This work has been conducted with several percentages (0.1, 0.2, 0.5, 1, 2, 5) of molybdenum disulfide (MoS₂) that has shown enhanced photocatalytic activity due to its bonding, chemical composition, and nanoparticle growth on the graphene films. The MoS₂ material has a bandgap of 1.8 eV that works in visible light, responding as a photocatalyst. The photocurrent and electrode/electrolyte interface of MoS₂- α -Fe₂O₃ nanocomposite films were investigated using electrochemical techniques. The MoS₂ material could help to play a central role in charge transfer with its slow recombination of electron-hole pairs created due to photo-energy with the charge

transfer rate between surface and electrons. The bandgap of the MoS₂ doped α -Fe₂O₃ nanocomposite has been estimated to be vary from 1.94 to 2.17 eV. The nanocomposite MoS₂- α -Fe₂O₃ films confirmed to be rhombohedral structure with a lower band gap than Al- α -Fe₂O₃ nanomaterial. The nanocomposite MoS₂- α -Fe₂O₃ films revealed a more enhanced photocurrent (180 μ A/cm²) than pristine α -Fe₂O₃ and other transition metal doped Al- α -Fe₂O₃ nanostructured films.

The p-n configuration has been used because MoS₂ can remove the holes from the n-type semiconductor by making a p-n configuration. The photoelectrochemical properties of the p-n configuration of MoS₂- α -Fe₂O₃ as the n-type and ND-RRPHTh as the p-type deposited on both n-type silicon and FTO-coated glass plates. The p-n photoelectrochemical cell is stable and allows for eliminating the photo-corrosion process. Nanomaterial-based electrodes α -Fe₂O₃-MoS₂ and ND-RRPHTh have shown an improved hydrogen release compared to α -Fe₂O₃, Al- α -Fe₂O₃ and MoS₂- α -Fe₂O₃ nanostructured films in PEC cells. By using p-n configuration, the chronoamperometry results showed that 1% MoS₂ in MoS₂- α -Fe₂O₃ nanocomposite can be a suitable structure to obtain a higher photocurrent density. The photoelectrochemical properties of the p-n configuration of MoS₂- α -Fe₂O₃ as n-type and ND-RRPHTh as p-type resulted 3-4 times higher (450 μ A/cm²) in current density and energy conversion efficiencies than parent electrode materials in an electrolyte of 1M of NaOH in PEC cells.

Titanium dioxide (TiO₂) is known as one of the most explored electrode materials due to its physical and chemical stability in aqueous materials and its non-toxicity. TiO₂ has been investigated because of the low cost for the fabrication of photoelectrochemical stability. Incorporation of various percentages (2.5, 5, 16, 25, 50) of TiO₂ in α -Fe₂O₃ could achieve better efficiencies as the photoanode by enhancing the electron concentration and low combination rate.

Both materials (α -Fe₂O₃, TiO₂) can have a wide range of wavelength which could absorb light in both UV and visible spectrum ranges. TiO₂ doped with α -Fe₂O₃ film was shown as increasing contacting area with the electrolyte, reducing e-h recombination and shift light absorption along with visible region. The α -Fe₂O₃-TiO₂ nanomaterial has shown a more enhanced photocurrent (800 μ A/cm²) compared to metal doped α -Fe₂O₃ photoelectrochemical devices.

CHAPTER 1: INTRODUCTION

1.1 Problem Description and Motivation

Today, worldwide, the search is on-going for alternative energy sources and inventive ways to generate renewable energy with much greater efficiency using free resources of the sun and water. Photomaterials have been studied in many experiments for splitting water into hydrogen and oxygen. α -Fe₂O₃ material is one of the most suitable photomaterials to be used as a photoelectrode in photoelectrochemical cells. The α -Fe₂O₃ is an excellent photomaterial due to ease in synthesis, abundance in nature, low cost, and favorable bandgap (~2.1 eV) that can absorb visible light (42% of sun radiations). This renewable solar energy can be explored to produce powerful hydrogen energy by splitting water using photocatalytic material (α -Fe₂O₃).

The performance of alpha-hematite as photomaterial has been limited by low conductivity, the short electron-hole pair time (<10 ps), and hole diffusion length (2-4 nm), which cause high recombination rates of photo-generated carriers in the bulk. Hematite-based water splitting has lower efficiency than that of the theoretical (12.6 mA/cm²) and has restricted PEC applications. Recent studies have identified that the doping process can enhance the morphology, structure, and shape of the materials. The electronic properties of α -Fe₂O₃ can be improved by doping with different materials such as metal oxide (Al), dichalcogenide material (MoS₂), and co-catalyst material (TiO₂). Aluminum- α -Fe₂O₃ nanocomposite has changed the bandgap to vary from 2.1 to 2.4 eV and there is a marked increase in the photocurrent. MoS₂- α -Fe₂O₃ nanocomposite has a new morphology that resembles a blooming flower due to the presence of MoS₂. The p-n configuration can improve the surface contact, which can produce more photocurrent. TiO₂ has

been used as a photocatalyst since 1970 and it is a photomaterial with bandgap 3.1 eV that can absorb ultraviolet radiation. $\text{TiO}_2\text{-}\alpha\text{-Fe}_2\text{O}_3$ nanocomposite enhances the photocurrent by absorbing both visible light and ultraviolet radiation.

The objectives of this dissertation are to improve/ enhance alpha-hematite material properties by:

- doping with transition metal materials such as aluminum (Al).
- doping with dichalcogenide materials such as molybdenum disulfide (MoS_2).
- using p-n configuration $\text{MoS}_2\text{-}\alpha\text{-Fe}_2\text{O}_3$ as n-type and polyhexylthiophene (RRPHT) - nanodiamond (ND) as p-type
- doping with a co-catalyst such as titanium dioxide (TiO_2)
- using p-n configuration $\text{TiO}_2\text{-}\alpha\text{-Fe}_2\text{O}_3$ as n-type and polyhexylthiophene (RRPHT) - nanodiamond (ND) as p-type

1.2 Organization of The Dissertation

The outline of this dissertation can be summarized as follows.

Chapter 1 explains the problem and the motivation for this dissertation synthesis and characterization of alpha-hematite material for water-splitting applications. This chapter also provides the overall organization of the dissertation and objectives.

Chapter 2 is a literature review that discusses alpha-hematite material for water-splitting applications using photoelectrochemical cells. It also describes methods of hydrogen production and ways to produce hydrogen using photoelectrochemical cells (PEC). This Mechanism of Photoelectrochemical Cells (PEC) was described in detail about the free electrons that can be generated by exposing light on the material. This chapter also provides a brief overview of

applications of proposed materials such as sensing, photovoltaic cells, fuel cells, water purification, lithium batteries, and supercapacitors.

Chapter 3 describes how aluminum- α -hematite thin films can enhance alpha-hematite for photoelectrochemical applications. This chapter introduces the importance of alpha-hematite for water-splitting applications and also how Al doping can increase the conductivity of alpha-hematite. This chapter also provides the synthesis process of the proposed materials by using sol-gel technique in detail. Fabricated nanomaterials were characterized to understand the physical properties by using different tools such as SEM, XRD, UV-Vis, FTIR as well as cyclic voltammetry and chronoamperometry to understand the electrochemical studies.

Chapter 4 explains how molybdenum disulfide α -hematite- nanocomposite films can be enhanced for photoelectrochemical applications. This chapter introduces the importance of the two-dimensional material (MoS_2) and ways various amounts of MoS_2 doped with $\alpha\text{-Fe}_2\text{O}_3$ can affect the morphology and structure of the nanocomposite $\text{MoS}_2\text{-}\alpha\text{-Fe}_2\text{O}_3$. Raman Spectroscopy was used to understand physical properties of $\text{MoS}_2\text{-}\alpha\text{-Fe}_2\text{O}_3$. A particle analyzer was utilized to estimate the particle size in a liquid phase.

Chapter 5 describes how p-n configuration can improve photoelectrochemical cell properties by using α -hematite-molybdenum disulfide as the n-electrode and polyhexylthiophene (RRPHTTh) - nanodiamond (ND) as the p-electrode. It also discusses how p-n configuration prevents the leakage of solvents and eliminates the photo-corrosion process. The mechanism of photoelectrochemical cells explains the process for RRPHTH-ND as p-type and $\text{MoS}_2\text{-}\alpha\text{-Fe}_2\text{O}_3$ n-type in 1 M NaOH electrolyte. The morphology was identified for $\text{MoS}_2\text{-}\alpha\text{-Fe}_2\text{O}_3$ to be blooming flower-like using SEM.

Chapter 6 discusses how the p-n based photoelectrochemical device can enhance the water-splitting application by using alpha-hematite ($\alpha\text{-Fe}_2\text{O}_3$)-titanium dioxide (TiO_2) as the n-electrode and polyhexylthiophene (RRPHTh) - nanodiamond (ND) as the p-electrode. This chapter provides introduction on how TiO_2 is an effective co-catalyst material that can be doped with $\alpha\text{-Fe}_2\text{O}_3$ due to its capability to absorb both visible light and ultraviolet radiation. The sol-gel technique was used to synthesis $\alpha\text{-Fe}_2\text{O}_3$ - TiO_2 nanomaterials. The film coating (n-type) was performed by spinning for TiO_2 - $\alpha\text{-Fe}_2\text{O}_3$ nanocomposite. The other material, (p-type) RRPHTh-ND, was dipped in the solution to create the film.

Lastly, Chapter 7 summarizes the results of using alpha-hematite nanomaterials for water-splitting applications. This dissertation found that $\alpha\text{-Fe}_2\text{O}_3$ is a promising photomaterial for the splitting of water. The conclusion of this chapter discusses suggestion for future research related to $\alpha\text{-Fe}_2\text{O}_3$ material including how to integrate solar cells with photoelectrochemical cells.

CHAPTER 2: LITERATURE REVIEW

2.1 Introduction

With the Earth's extreme weather and evidence of climatic change accumulating/increasing, global efforts have increased dramatically to secure energy sources that are as cheap as fossil fuels but without the unwanted by-products and toxic side effects. This chapter reviews the improvements of hydrogen production and the size of the material particles into the nanomaterial range resulting in capabilities of clean, renewable energy. Attempts have been made to understand the splitting of water into hydrogen and oxygen using alpha-hematite-based nanomaterial in photoelectrochemical based devices. As discussed in this chapter, several methods have been utilized for producing hydrogen it could be the ultimate fuel if produced economically. Hydrogen can be produced from H_2S , H_2O , metal hydrated etc. sources, and although the materials and techniques for hydrogen production have been discussed, the photoelectrochemical technique has been found to be advantageous over other techniques.

Freedom from fossil fuel sources and the pollution and toxins associated with them has become a reality thanks to the implementation of nanotechnology. Researchers are hopeful that clean, renewable, inexpensive and easily obtained energy can be produced using the two most plentiful substances/ materials on the planet: sunlight and water (as shown in Figure 1).

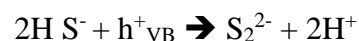
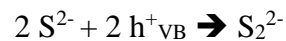
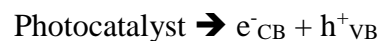


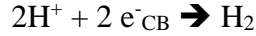
Figure 2.1 Our greatest resources: sun and water (photo credit: personal camera, May 15 2018)

2.2 Methods of Hydrogen Production

Different methods have been employed to split H_2O and H_2S to produce hydrogen gas including thermo-chemical [1-5], plasma-chemical [6-8], thermal [9-11], electrochemical [12-14], and photochemical methods[15-21]. The photochemical method, however, has the greatest potential because it uses a renewable energy source such as solar energy. Figure 2 shows how sunlight is used to drive hydrogen production by separating hydrogen sulfide in a photocatalytic reactor using a process called photo-catalysis [22].

Equations are for the photo-catalysis process:





The net reaction is simply:

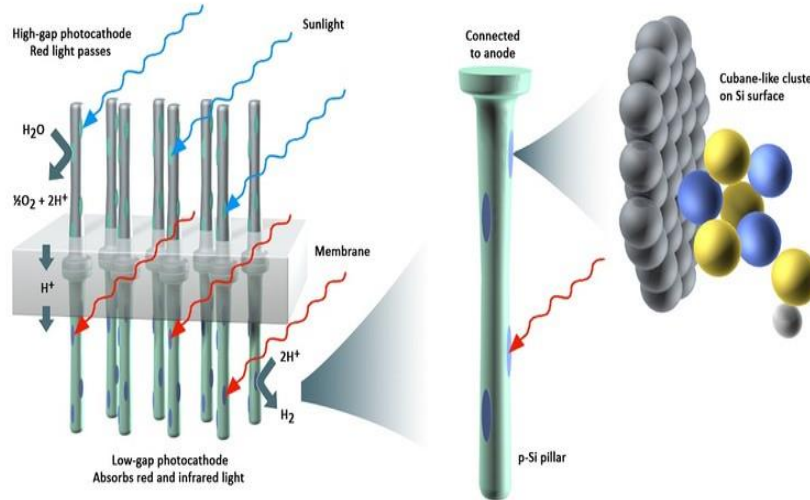
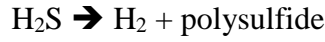
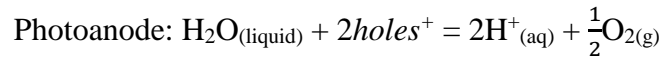


Figure 2.2 Schematic of hydrogen production using photocatalyst [22]

2.3 Hydrogen Production by Photoelectrochemical Cells (PEC)

The process of photolysis to produce hydrogen gas is made possible by the use of solar cells which are referred to as photoelectrochemical cells (PEC). The cells are irradiated with light around the visible region of the solar energy. Then, the cell converts the visible light photons from the solar energy into electricity for the semiconductor anode and cathode immersed in an electrolyte [23]. The photolysis equations of the photo anode reactions are as shown:



In the PEC cells, the semiconductor photo-anode absorbs the light photons themselves in order to facilitate the chemical reactions that take place in the electrolyte being used. Hydrogen

gas is produced in the endothermic reaction, resulting in a net change in reactants. This process involved in the PEC only slightly differs from the normal electrolysis with the involvement of electrons and holes as charge carriers.

A slight modification of this process using photo-catalysis employs the use of photo-electrodes that are exposed to generate electrons and holes in the PEC. The photo-catalysts used as electrodes separate water directly to produce hydrogen and oxygen gas. Modifications of the photo-catalyst structure to produce nano-crystalline coatings in order to improve the yield of hydrogen gas has been explored by Alenzi et al. [24].

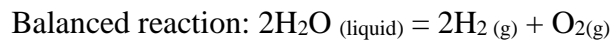
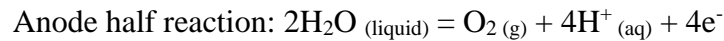
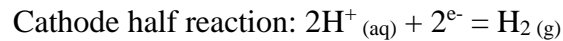
Combining two techniques, the use of solar photoelectrochemical cells (PEC) have each been considered in the production of hydrogen gas. These two techniques have been proven to improve the yield of hydrogen gas even while using cheap sources of electricity obtained by harnessing solar energy and using photoelectrodes in PEC. This has been explored and processed, and the outcome as presented is termed the “Integrated Solar-Nano Hydrogen System”[23]. This process is designed to boost the production of hydrogen gas using these two above named techniques in a single system. Solar energy is harnessed simultaneously by the use of solar cells and the heat collectors [23]. The PECs absorb light photons to be used directly as electricity to reduce water while the heat obtained from the heat collectors may be used to also generate electricity or to increase the temperature of the photoelectrochemical cells [23]. The overall energy cost is economically lower since the maximum benefit is derived from the solar energy used for the two techniques simultaneously in one system.

The direct use of the sun’s irradiation is made possible in the use of PEC that has photoelectrodes which are made from semiconductor materials. Likewise, the use of heat derived from the conversion of solar irradiation is also made possible with the use of semiconductor

materials. These two points stress the importance of semiconductor materials in the production of hydrogen gas from water splitting using cheap, green, and renewable solar energy. Modifications of the semiconductor's structure in order to alter its electronic properties to improve the efficiency of the processes and the yield of hydrogen are considered. These modifications using metallic deposition on the surface of the semiconductor is meant to make the resulting nano-composite crystalline [23].

2.4 Mechanism of Photoelectrochemical Cells (PEC)

The process of electrolysis has been used in generating hydrogen gas with 99% purity using direct current to split water molecules into hydrogen gas and oxygen gas. The cathode and anode of the electrolyzer used is dependent on the electricity generated from the combustion of fossil fuels. The use of solar energy in the generation of hydrogen, however, is in two forms: thermolysis and photo-electrolysis.



The equations above show the cathodic reduction equation, the anodic oxidation equation and the overall equation of the process of electrolysis[23].

Thermolysis uses the energy from the sun to generate heat in materials that are used to generate the hydrogen gas. Before expounding upon the use of photo-electrolysis and thermolysis, an understanding of the use of solar cells and solar energy is necessary.

The sun is composed of extremely hot gases in the form of a sphere 109 times larger than the earth [23]. The estimated temperature of the sun's surface is approximately 5,726K, which travels through the atmosphere before reaching the earth's surface[23]. Travelling through the

atmosphere, solar radiation becomes reflected, scattered, and absorbed by water vapor, clouds, and other particles before reaching the surface of the earth. The average intensity of solar power upon reaching the earth is thus estimated to be 1353 W/m^2 [23].

Solar cells that generate electricity using solar power operate based on the photovoltaic (PV) effect. The PV effect describes a situation where a material generates electricity when light is shone upon it. The materials used in PV cells are semiconductor materials such as silicon and gallium arsenide. The generation of electricity is attained when the energy from the incident light becomes sufficient enough to excite electrons from the valence band of the molecules of the semiconductor material to the conduction band. Generation of electricity from PV cells is simple and does not contribute to environmental degradation.

As shown in Figure 3, the process of photoelectrochemical cells is entrenched in the transfer of an electron from the first side, which is the valence band (VB), to the second side, which is the conduction band (CB), when sufficient light is absorbed by the photomaterial. The electron jumps the bandgap into the conduction band when it becomes excited because of irradiation with light of sufficient wavelength and leaves a hole in the valence band. For the promotion of electrons from the valence band to the conduction band, the wavelength of the absorbed light must be less than or equal to the energy band gap of the semiconductor material. The promotion of an electron into the conduction band leaves a hole previously occupied by the electron in the valence band. Thus, an electron-hole pair is generated by the photo-catalysis process. The generated electron-hole pair can participate in one of many pathways. The pathways useful for splitting H_2S and H_2O to produce hydrogen gas are those involving the loss of electrons in the conduction band and loss of holes in the valence band due to electrochemical processes. These pathways are influenced by

controlling the semiconductor with surface modifications and by adding electrolytes and reactive redox (reduction - oxidation) species.

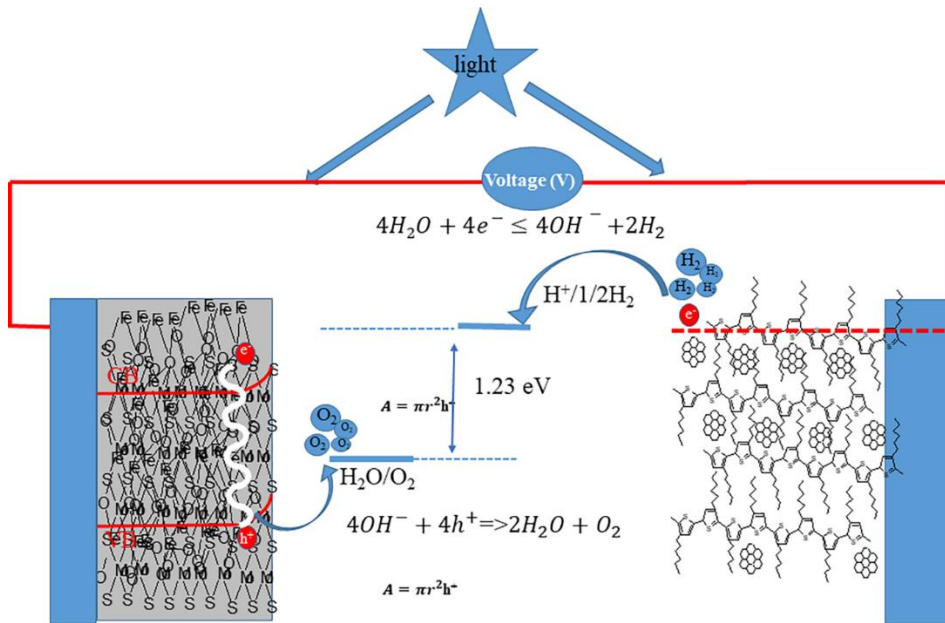


Figure 2.3 Schematic of photoelectrochemical cells (PEC)

2.5 Photocatalytic Materials

In a review, Preethi and Kanmani examined the efficiency of different nanomaterials in hydrogen gas production using photo-catalysis [25]. This review provides a broad overview of the different nanomaterials used for the production of hydrogen gas through the splitting of hydrogen sulfide gas and water molecules [25]. Hydrogen sulfide gas is detrimental to the environment because of its corrosive nature in the form of sulfide. The use of H_2S to produce hydrogen gas is therefore preferred to the splitting of H_2O . This is not only because it helps remove the environmentally harmful hydrogen sulfide gas but also because it is less costly and faster to produce. However, despite this preference and desirability for the use of H_2S in the production of hydrogen gas, the near future depletion of non-renewable energy sources such as coal and fossil fuels, which are the major sources of H_2S , will result in the non-availability of the gas for the production of hydrogen gas [25]. The implication of this is that the splitting of H_2O to produce

hydrogen gas will compensate for the splitting of hydrogen sulfide gas. Different types of nanomaterials have been identified as useful in the production of hydrogen gas. These materials include metal oxide semiconductor materials such as TiO_2 and BaTi_4O_9 and metal sulfide semiconductor materials such as CdS and RuS_2 [25].

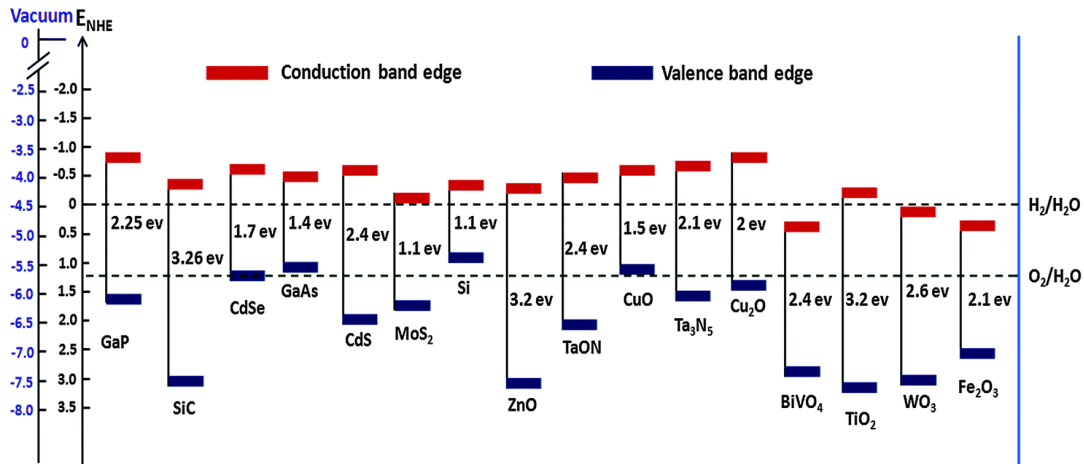


Figure 2.4 Band edge positions of semiconductor materials [26]

Figure 4 shows the conduction band edge and the valence band edge of semiconductor materials. One of the lowest bandgaps is 1.1 eV for silicon, which absorbs infrared radiation, while one of the highest bandgaps is 3.2 eV for TiO_2 , absorbing the UV radiation. Sun light comes in different forms of radiation, with the three most common forms being UV radiation, visible light, and IR radiation. Alpha-hematite material has a low bandgap of 2.1 eV, which can absorb the visible light range containing 42% of the sun light radiation [26].

Most nanomaterials used as photo-catalysts to produce hydrogen gas have been identified as giving a higher yield in the production of hydrogen as compared to bulk materials [25]. Those that do not give a maximum production are still higher in their yield than bulk materials. The technique used to prepare the photo-catalyst plays an important role in the yield of the nanomaterial photo-catalyst. The technique affects the particle size of the catalyst and its crystallinity. The smaller the particle diameter of the catalyst, the more active the catalyst and consequently,

increases the yield of hydrogen production. Improvement in the efficiency of the photo-catalyst is also achieved by doping the nanomaterials with transition elements. The different photo-catalysts that can be used under irradiation by visible light from a lamp include CuFeO_2 , CuLaO_{262} , FeGaO_3 , and $\text{CuCr}_2\text{O}_4/\text{TiO}_2$. These are referred to as spinal photo-catalysts [25].

2.5.1 Cadmium Sulfide (CdS)

Another type of nanomaterial used for the liquid phase of photo-catalysis is cadmium sulfide and other materials related to it. The cadmium sulfide can be used alone or doped with TiO_2 or ZnS in the production of hydrogen gas from hydrogen sulfide dissolved in water or alkali solution. As noted previously, the method of production of the photo catalyst influences the activity of the catalyst. The cadmium sulfide, as a photo-catalyst, is fabricated through hydrothermal and sol-gel techniques to make it highly active for hydrogen gas production from water containing sulfide ions under irradiation with visible light. Cadmium sulfide-based photo-catalysts produce similar results even in a system using hydrogen sulfide dissolved in NaOH electrolyte. The semiconductor has the capability to absorb visible light but not in pure water because it undergoes anodic photodecomposition [25].

2.5.2 Zinc Oxide (ZnO)

Nano structured zinc oxide (ZnO) is also a very stable semiconductor material with photo-catalytic activity needed for photo-catalysis. Because of the high band gap, photo excitation of zinc oxide to produce the electron-hole pair needed for hydrogen gas production from hydrogen sulfide gas requires ultraviolet (UV) light [25]. The use of visible light is, however, made possible when the zinc oxide is doped with copper, which has a low band gap and good crystallinity [25].

2.6 Alpha-Hematite (α -Fe₂O₃)

2.6.1 Introduction and Properties

Alpha-Hematite (α -Fe₂O₃) is the most common naturally approachable semiconducting photocatalyst with bandgap 2.1 eV. The α -Fe₂O₃ can absorb up to 40% of solar spectrum energy. The photoanode based on α -Fe₂O₃ has been used in photoelectrochemical application due to excellent photochemical stability. Moreover, α -Fe₂O₃ has been used for different applications such as sensors, catalyst, pigments, drug delivery, and photoelectrochemical cells [26].

2.6.2 Characterization

2.6.2.1 X-ray Diffraction (XRD)

The hematite nanoparticle has been identified to have rhombohedral structure. The α -Fe₂O₃ NPs shows the metallic iron consisting of the face-centered cubic (FCC) phase. The major peaks are shown in Figure 5 for the α -Fe₂O₃ NPs that have been assigned to be (0 1 2), (1 0 4), (1 1 0), (1 1 3), (0 2 4), (1 1 6), (0 1 8), (2 1 4) and (3 0 0) planes [27].

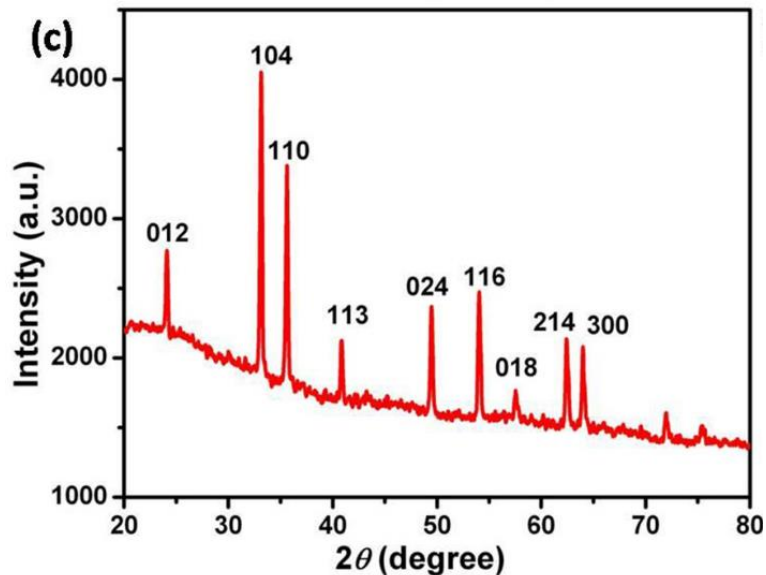


Figure 2.5 X-ray diffraction pattern of α -Fe₂O₃ [27]

2.6.2.2 Fourier Transform Infrared Spectroscopy (FTIR)

The FTIR has been a profound tool to understand the chemical bounds of nanomaterials. Figure 6 shows a 3463 cm^{-1} band due to O-H stretching, with 1631 cm^{-1} due to C=C stretching present in the nanomaterials. However, the presence of bands at 580 and 474 cm^{-1} are due to Fe-O group found in the $\alpha\text{-Fe}_2\text{O}_3$ NP [28].

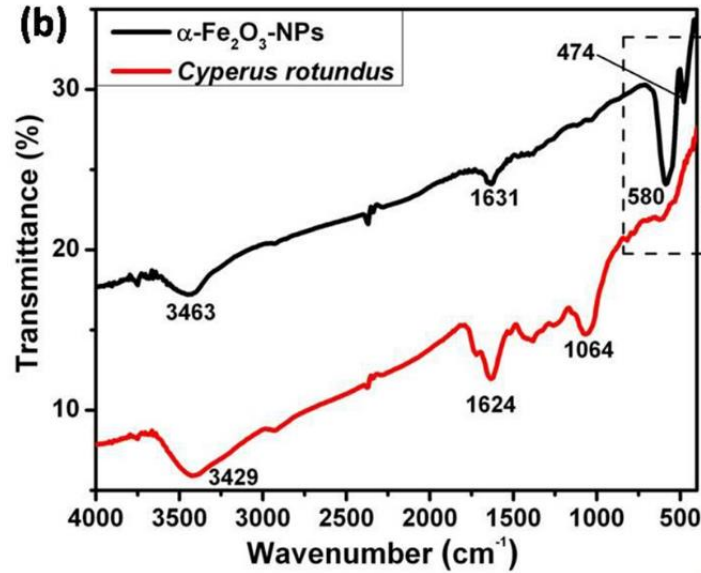


Figure 2.6 FTIR spectra of $\alpha\text{-Fe}_2\text{O}_3$ [28]

2.6.2.3 Scanning Electron Microscopy (SEM)

SEM is a versatile tool to investigate the shape, size, and morphology of nanostructured materials. Figure 7(a) shows the flower-like shape structure while Figure 7(b) shows how the spindle-like nanoparticles form a micro-flower structure [28].

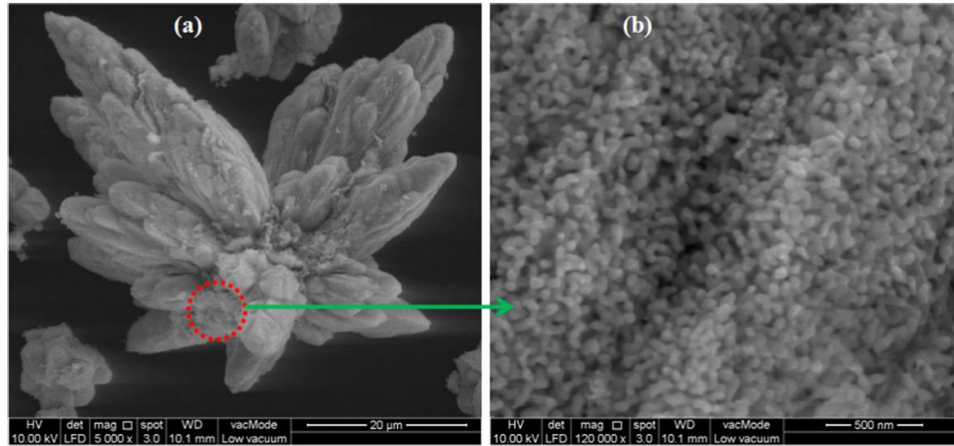


Figure 2.7 SEM images of α -Fe₂O₃ [28]

2.6.2.4 Transmission Electron Microscopy (TEM)

The transmission electron microscopy (TEM) study is a versatile method to understand the size and shape of nanomaterials. The TEM has shown a resolution of 0.2 nm for synthesized hematite nanomaterial (Figure 8(a)). Figure 8(c) observes 2.4 nm in size of mean nanoparticle alpha-hematite material. In addition, TEM shows how the particles are well distributed [29].

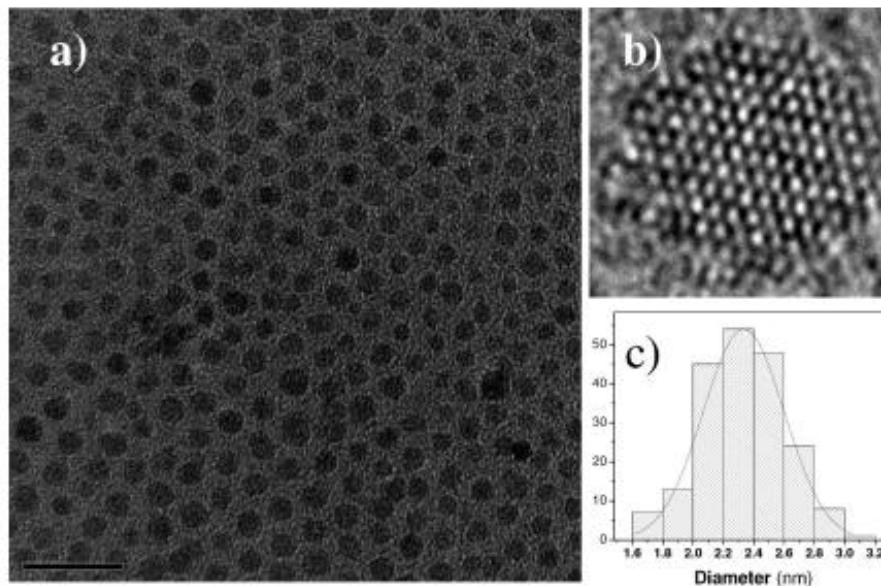


Figure 2.8 TEM images of α -Fe₂O₃ [29]

2.7 Enhanced Water Splitting in α -Hematite

Water splitting using α -hematite has been improved through modification of the structure (shape and size) of the nanomaterials. The properties of α -hematite are largely affected if the structure is nanotube, nanowire, hollow tubular, or spherical structure. However, the self-assembled or array could easily affect the properties of the water splitting application. Doping using soft metal, transition metal, and dichalcogenide have been performed to enhance the physical properties of the nanomaterials. In addition, the composite, or co-catalyst formation with different transition metal oxide with α -hematite, has been attempted to improve the water splitting properties in photoelectrochemical cells [30].

2.7.1 Modification Structure

Different synthesis processes affect the shape and size of the nanomaterial. Lassoed et al. have shown that an increase of precursory (FeCl_3) concentration leads to a size increase of the alpha-hematite nanomaterial [30]. They have shown that $[\text{Fe}^{3+}]$ with 0.05 M revealed the best crystallinity, size, and bandgap of 2.09 eV. Figures (a-d) show the spherical structure of α -hematite varying in size from 21 nm to 82 nm [30].

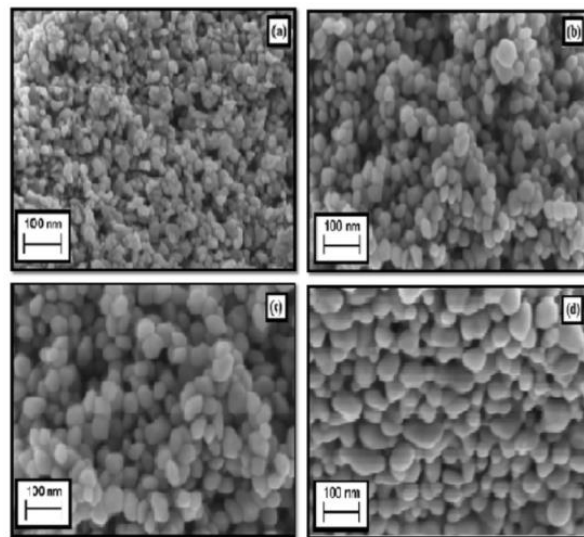


Figure 2.9 SEM images of various concentrations of α - Fe_2O_3 [30]

2.7.1.1 Nanotube (NTAs) and Nanorod (NRA) Structure

As shown in Figure 10, the nanotube of $\alpha\text{-Fe}_2\text{O}_3$ and nanorod of SnO_2 can be synthesized using the hydrothermal process. The nanotubes synthesized for $\alpha\text{-Fe}_2\text{O}_3$ have been found to be ~ 50 nm in diameter with a wall thickness of ~ 10 nm. The imposition of various times affects the size of the nanorod and nanotube. The hydrothermal reaction of one hour has been found to result in a thin and dense nanoparticle layer. However, the reaction time of two hours showed the cuboid nanorods of SnO_2 with a width of approximately of 50 nm [31].

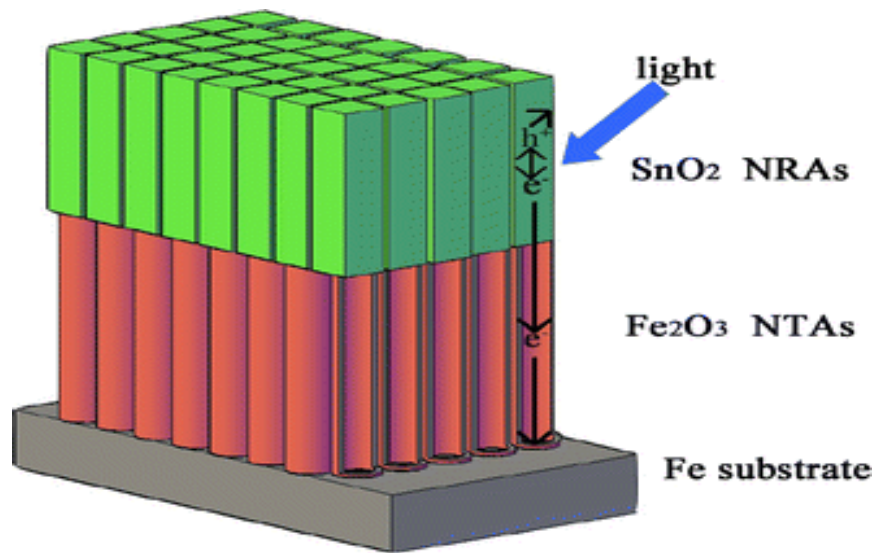


Figure 2.10 Schematic of SnO_2 NRAs/ $\alpha\text{-Fe}_2\text{O}_3$ NTAs composite nanostructure [31]

2.7.1.2 Nanowire Structure

The nanowire of $\alpha\text{-Fe}_2\text{O}_3$ with 1-5 μm length can be synthesized by heating to approximately 700°C in a time scale of seconds. Figure 11 shows the SEM pictures of $\alpha\text{-Fe}_2\text{O}_3$ grown through 100 nm/s. The NW can then be grown in a crystallographic direction. The sword-like shape nanowire growth is controlled through the diffusion process. Figure 12 shows the schematic of nanowire growth in ambient temperature [32].

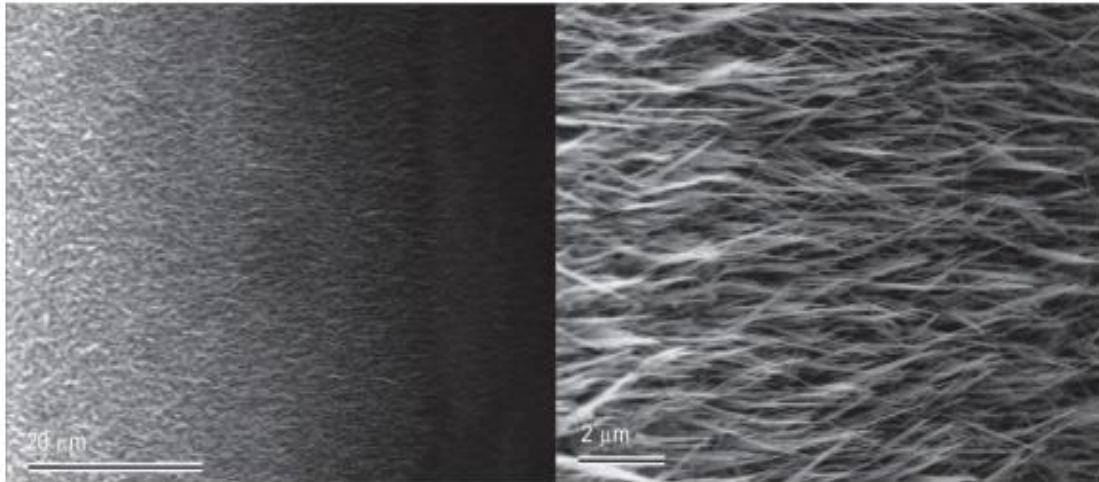


Figure 2.11 SEM images of iron wire surface after synthesis [32]

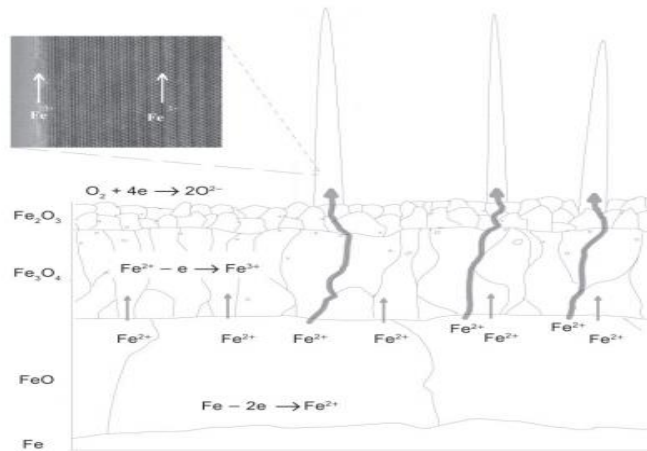


Figure 2.12 Schematic of the NW growth in ambient air [32]

2.7.2 Doping

Doping in general is the tailoring of physical and chemical properties of semiconductors for various applications. Ti, Al, Sn, Mn, Ti, Si, Ge, etc. transition metals have been doped with α - Fe_2O_3 for water-splitting applications. Doping using various transition metals affects the morphology, structure, shape of α - Fe_2O_3 . Moreover, the doping brings a change in lattice of hematite rather than a change on surfaces. The doping is generally organized for superlattice structures or to take a disordered, solid solution state. Clusters in the structure are also caused by

doping as well as changes in magnetic properties (electrochemical, electrical and electronic properties) of α -Fe₂O₃ undoped bulk hematite as shown in Table 2.1. Additionally, the structure, morphology, and size of α -Fe₂O₃ are dependent on the type of dopant. As shown in Figure 13, the germanium and silicon doping in α -Fe₂O₃ observes nanosheets structures, whereas the tin doping reveals peanut-like nanoparticles of α -Fe₂O₃ [33].

Table 2.1: Different doping materials with alpha-hematite.

Doped Material	Synthesis	Properties	Volt	Finding
α -Fe ₂ O ₃ [34]	Hydrothermal		1.5 V	4 μ A cm ⁻²
Au- α -Fe ₂ O ₃ [34]	Hydrothermal	Nanorod (650 nm)	1.5 V	1.16 mA cm ⁻²
CoOOH/(Ti, C)-Fe ₂ O ₃ (CTCF)[35]	facile approach	Nanorods	-	1.85 mA cm ⁻²
Carbon-doped α -Fe ₂ O ₃ [36]	magnetron sputtering	2.13-2.16 eV	0.6V	1.18mA/cm ²
Cr-doped α -Fe ₂ O ₃ [37]		Nanorod arrays		3.5 and 6 times
Co-doped Fe ₂ O ₃ [38]		nanorods	1.23 V	1.25 mA/cm ²
Ti-doped α -Fe ₂ O ₃ [39]	hydrothermal	nanocubes	1.23V	IPCE of 25.2%
Ti-doped (α -Fe ₂ O ₃) [40]	solution growth		1.0 V	0.66 mA cm ⁻²
WO ₃ -doped (α -Fe ₂ O ₃) [41]	doctor blade method		0.8 V	1.18 mA/cm ²
Zirconium-doped α -Fe ₂ O ₃ [42]	electrodeposition method		0.6 V	2.1 mA/cm ²
S-doped Fe ₂ O ₃ [43]		Nanorods array	1.23 V	1.42 mA/cm ²
α -Fe ₂ O ₃ /CdS [44]	facile two-stage method		0.4 V	0.6 mA/cm ²
Fe ₂ O ₃ /BiVO ₄ [45]	metal-organic deposition method		1.23 V	7.0±0.2 mA cm ⁻²
Sn-doped Fe ₂ O ₃ [46]	hydrothermal	nanocorals	1.23 V	1.86 mA/cm ²
Pt-doped Fe ₂ O ₃ [47]	electrodeposition		0.4 V	1.43 mA/cm ²
ZnO/Fe ₂ O ₃ [48]		Core-Shell Nanowires	0.6 V	~0.75 and ~0.5 mA cm ⁻²
Zn-doped α -Fe ₂ O ₃ [49]		Nanotube arrays	0.5 V	40.4 μ A cm ⁻²

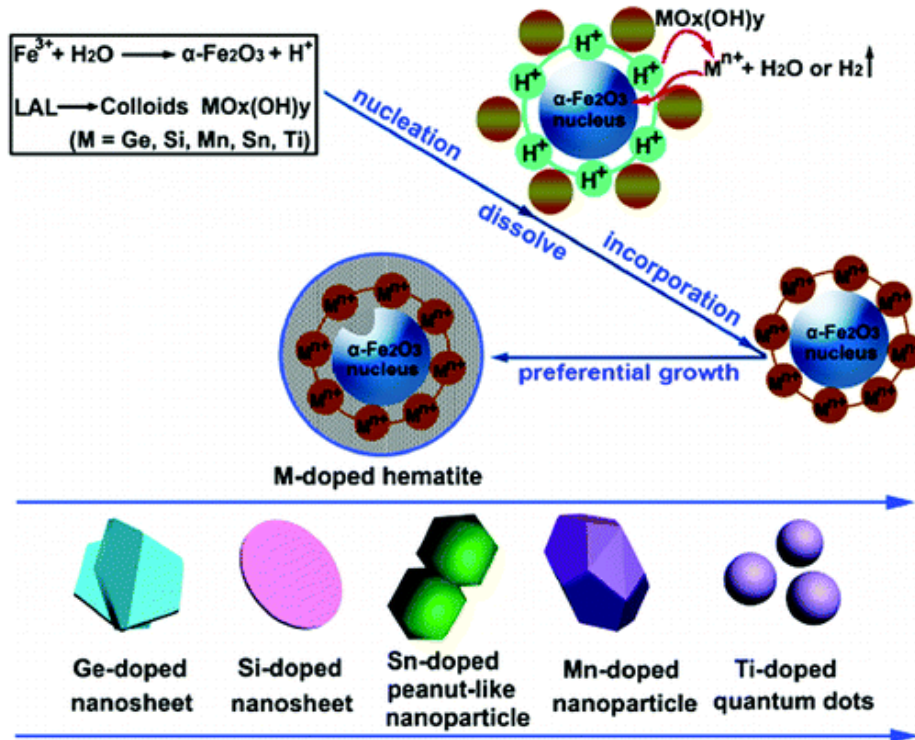


Figure 2.13 Schematic for various doping materials (Ge, Si, Mn, Sn, Ti) in $\alpha\text{-Fe}_2\text{O}_3$ [33]

2.8 Applications of α -Hematite Photoconduction Material

2.8.1 Sensing

The alpha-hematite can be used for the sensing device and Ag can be doped to enhance the electronic properties of alpha-hematite. The results showed that Ag particles enhance the surface of the composite and offer much higher detection of CH_3SH than the bare alpha-hematite. The hematite containing 3% silver shows the sensing of CH_3SH in the range of 20–80 ppm at room temperature [50].

2.8.2 Photovoltaic Cells (PV)

Photovoltaic cells are one of the most important applications globally, and countless materials have been tested to achieve high results. Alpha-hematite is a desirable material for PV because it is cheap, durable, and nontoxic and can absorb visible light from sun irradiation. The size of the material can also affect the absorption intensity; a 400-600 nm area has a higher absorption

intensity than 250-400 nm area. The size decrease from 48 to 5 nm brings changes in the intensity in addition to the shift in absorption band edge at wavelengths from 533 to 488 nm. The increase in magnetic tilt coupling brings the pair excitons, which causes local d-d transition and band tail types of charge-transfer. The band tail charge transfer produces photovoltaic responses due to delocalization [51]

2.8.3 Fuel Cell Production

Alpha-hematite is an abundant material that can be used in various applications. One application that can utilize alpha-hematite is the production of fuel cells using Microbial fuel cell (MFCs) devices. These devices can produce electricity using microorganisms as biocatalysts due to the electrochemical reactions. In this device, the self-assembly technique was used to synthesize alpha-hematite nanorod with chitosan (CS) based on layer-by-layer (LBL). This technique enhanced the modified $(\text{Fe}_2\text{O}_3/\text{CS})_4/\text{ITO}$ anode and produced high electricity of 320% compared to the unmodified anode and also other enhanced anodes [52].

2.8.4 Water Purification

Alpha-hematite is a semi-conducting material with a low band gap and is considered a photo material that can absorb visible light. The alpha-hematite can work for water purification, but it must be doped to enhance its properties. TiO_2 is also a photo-material that can be synthesized with alpha-hematite by using impregnation of Fe^{3+} into meso- TiO_2 followed by calcination at 300 °C. XRD and TEM were used to investigate the morphology and structure [53].

2.8.5 Lithium Batteries

Lithium battery use is a broad subject, and many experiments have been performed to test various materials offering good results; alpha-hematite is one. As shown in Figure 29, the spindle-like porous $\alpha\text{-Fe}_2\text{O}_3$ was synthesized using the metal organic framework (MOF) template. The

spindle structure of α -Fe₂O₃ was investigated for Li storage capacity. The use of MOF enhanced the charge storage in Li-ion batteries due to a high surface area. Figure 22 (a& b) shows SEM images of the FeOx-C composite while Figure 29 (c and d) shows the particle length by using TEM varying from 0.8 μ m to 0.4 μ m.[54]

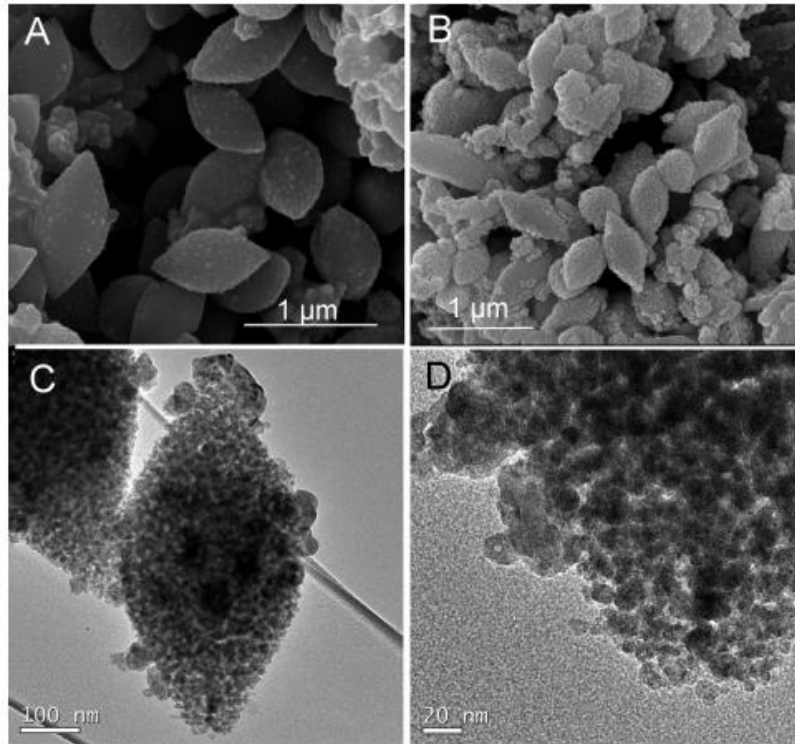


Figure 2.14 SEM images of FeOx-C composite [54]

2.8.6 Supercapacitor

The supercapacitor is one application that uses alpha-hematite after enhancing its properties. PANI can be synthesized with alpha-hematite to have new structure nanowire arrays. The α -Fe₂O₃-PANI core-shell nanowire arrays have been synthesized for use in supercapacitor electrodes as shown in Figure 23 (a). The new structure of alpha-hematite-PANI offers the electrode for supercapacitor application having fast ion and electron transfer, large surface area, and structure stability. As shown in Figure 23 (b), α -Fe₂O₃-PANI nanowire arrays showed the volumetric capacitance of 2.02 mF/cm³ and energy density of 0.35 mWh/cm³. The supercapacitor

from α -Fe₂O₃-PANI nanowire arrays showed high cycling stability with 95.77% retention of capacitance after 10 000 cycles.[55]

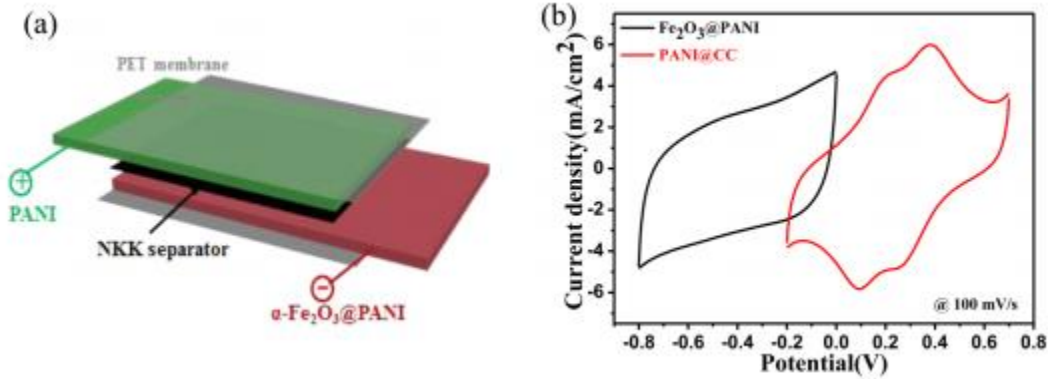


Figure 2.15 (a) Schematic of the structure of the supercapacitor (b) CVs of the α -Fe₂O₃-PANI and PANI electrodes [55]

2.8.7 Corrosion Resistance

Alpha-hematite is useful for corrosion resistance, but it must be enhanced by other materials to yield high results. One of the candidate materials that can enhance properties of alpha-hematite is PANI. Chemical oxidative polymerization of aniline was used to make PANI- α -Fe₂O₃ NCs. The synthesis of PANI- α -Fe₂O₃ NCs reduces the conductivity due to alpha-hematite that hinders PANI conductivity. Potentiodynamic polarization technique was utilized to test the coating (PANI- α -Fe₂O₃ NCs) for the corrosion of 316LN stainless steel in 3.5% NaCl. The test for PANI- α -Fe₂O₃ provides high results for the corrosion resistance [56].

2.9 Conclusion

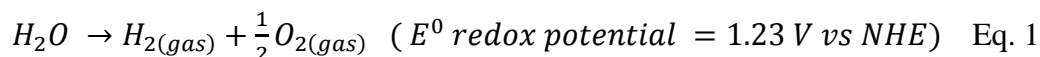
In summary, it be clearly stated that the involvement of photomaterials in the study of hydrogen production for clean energy will be an important element for future research. Doping alpha-hematite with transition metals, dichalcogenide materials and co-catalyst materials can improve the physical and electronic properties. Several synthesis methods exist, but the sol-gel method is easy to work with because it is less expensive and faster than other methods. The use of

nanoparticles, nano-coatings, nano-films, and other nano-products in existing methods of hydrogen generation have effectively demonstrated the premise that increasing the surface area for reaction substantially increases the rate of production and therefore increases the total volume of hydrogen fuel produced per unit of time for any given process.

CHAPTER 3: ALUMINUM - α -HEMATITE THIN FILMS FOR PHOTOELECTROCHEMICAL APPLICATIONS¹

3.1 Introduction

Hydrogen has been considered clean energy because of its high energy density and ease in burning with oxygen to produce water [57]. Hydrogen production using photocatalytic materials under a photoelectrochemical technique is an appealing and cost-effective technique. Water splitting is an endothermic process which requires more than 1.23 V vs NHE (Eq. 1) [57].



So, several photoanodes (WO_3 [58], ZnO [59], TiO_2 [60, 61], and α - Fe_2O_3 [62-65]) have been used in PEC-based water splitting to produce hydrogen. However, α - Fe_2O_3 and metal ion doped α - Fe_2O_3 materials have been considered suitable photoelectrode materials [63, 66-69]. α - Fe_2O_3 is indeed an excellent photoelectrode material due to the ease in synthesis, abundance, low cost, and favorable band gap (~ 2.1 eV) for splitting water to hydrogen [47, 57, 70-72]. α - Fe_2O_3 has high resistivity, shows slow surface kinetics, and possesses low electron mobility and high electron-hole combination due to low carrier diffusion properties [73].

The intrinsic electronic properties of α - Fe_2O_3 can be controlled by doping with different metal ions (Ti, Pt, Mo, Cr, Al, Zn etc.) [73-78]. The metal doped Fe_2O_3 nanorod array has shown nearly 5% higher solar-to-hydrogen conversion efficiency for photoelectrochemical water

¹This chapter has been published “Alrobei, H., A. Kumar, and M.K. Ram, ALUMINUM- α -HEMATITE THIN FILMS FOR PHOTOELECTROCHEMICAL APPLICATIONS. Surface Review and Letters, 2017: p. 1950031” and copyright permission in appendix A.1

splitting than the undoped α -Fe₂O₃ [79]. The smaller sized metal ions (boron and aluminum) in α -Fe₂O₃ have shown improved charge transport properties through strain introduction in the lattice structure, thus increasing the light absorption[80].

Under this manuscript, different percentages of Al ions were used in α -Fe₂O₃ to enhance the hole/electron transport properties, homogenous structure, and stability of the nanomaterial. The low to high percentage of aluminum from 0.5% to 30% in α -Fe₂O₃ structure was introduced to understand the physical properties of Al- α -Fe₂O₃ and their photoelectrochemical properties under light. The concentration of aluminum ions varied from 0.5%, 10%, 20% and 30% of α -Fe₂O₃. The nanomaterials were characterized using X-ray diffraction, SEM, FTIR and UV-vis techniques, respectively. Cyclic voltammetry (CV) and impedance studies were conducted to understand the electrochemical behavior of electrode/electrolyte interface under the influence of light. The chronoamperometry studies on Al- α -Fe₂O₃ were performed to understand the properties of splitting water into hydrogen.

3.2 Experimental Details

3.2.1 Materials

FeCl₃, AlCl₃, NaOH, NH₄OH, and fluorine tin oxide (FTO) coated glass with resistance of ~10 Ω were purchased from Sigma-Aldrich. A centrifuge was used to clean the synthesized nanomaterial from the resulting solution.

3.2.2 Experimental Procedure

The α -Fe₂O₃ and Al- α -Fe₂O₃ nanomaterials were synthesized via sol-gel technique. Eq.2 reveals the synthesis of Al- α -Fe₂O₃ nanomaterial using this technique. Initially, various concentrations of FeCl₃ and AlCl₃ were prepared. Table 1 shows the amount and ratio of chemicals used in the synthesis of Al- α -Fe₂O₃ nanomaterial. NaOH solution of 1M was added to the mixture

solution of $FeCl_3$ and $AlCl_3$ in a round bottom flask and stirred with a magnet. Later, a condenser was connected to the round bottom flask, the solution temperature was raised to 90-100 °C, and the reaction continued for 24 hours. The reaction was terminated after 24 hours, and the solution was cooled at room temperature. The synthesized material was separated using a centrifuge and continuous cleaning with water. The $Al-\alpha-Fe_2O_3$ nanomaterials were initially left drying at room temperature and then dried at various temperatures (100, 200, 300, 400, and 500 °C). In each case, the temperature was maintained in a furnace for one hour. The materials were brought to room temperature and collected in a tight bottle.

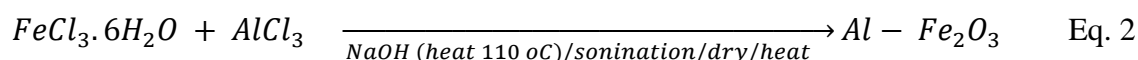


Table 3.1: Amount of chemical used for synthesis of $Al-\alpha-Fe_2O_3$

Chemicals	0.5% $AlCl_3$ w.r.t $FeCl_3$	5% $AlCl_3$ w.r.t $FeCl_3$	10% $AlCl_3$ w.r.to $FeCl_3$	20% $AlCl_3$ w.r.to $FeCl_3$	30% $AlCl_3$ w.r.to $FeCl_3$
$FeCl_3$	0.68 g	6.8 g	6.8 g	6.8 g	6.8 g
$AlCl_3$	0.0266g	0.266g	0.532g	1.064g	1.596g
NaOH	4.8g	4.8g	4.8g	4.8g	4.8g

α -hematite nanomaterial with different percentage of aluminum (Al) ions

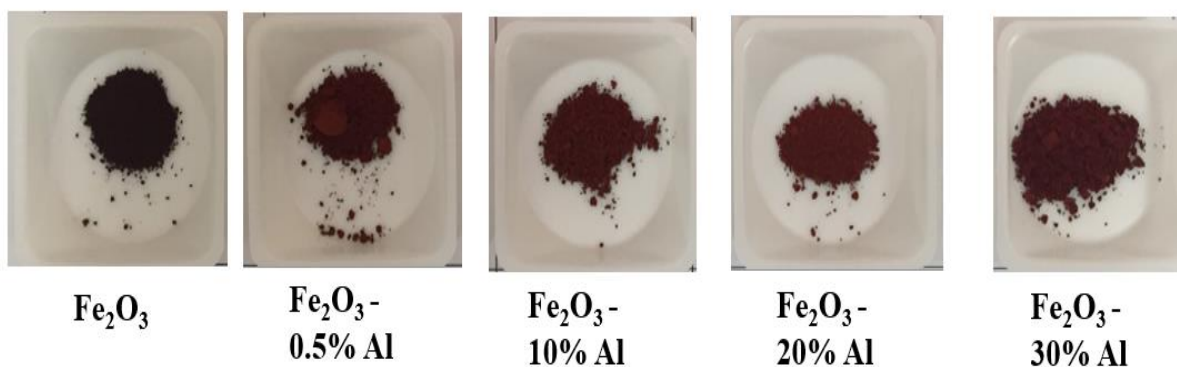


Figure 3.1 Synthesized α -hematite ($\alpha-Fe_2O_3$) and $Al-\alpha-Fe_2O_3$ materials

3.2.3 Film Formation of Substrate

The Al- α -Fe₂O₃ nanomaterial paste was prepared by mixing acetic acid. Initially, 500 mg of each Al- α -Fe₂O₃ (0.5%, 10%, 20%, 30%) nanomaterial was ground and mixed with 10 ml acetic acid and left for 10 hours. Later, the thin film was applied to quartz, silicon, and fluorine tin oxide (FTO) by the solution cast technique. The coated films were cured at different temperatures of 300, 400 and 500 °C with an interval of one hour. The films were then cooled to room temperature before any measurements were taken.

3.3 Physical Properties Studies

3.3.1 UV-Visible Spectroscopy (UV-Vis)

Figure 2 shows UV-visible spectra of Al- α -Fe₂O₃ film on quartz substrates. Table 2 shows the UV-vis peaks at nm for various percentages of Al in Al- α -Fe₂O₃ nanomaterial. Its UV-vis absorption band is located between 580-680 nm, depending on the aluminum present in the α -Fe₂O₃ structure. The characteristic broad absorption band at 639 nm and sharp band at 560 nm for α -Fe₂O₃ are observed in Figure 2. (2.2 eV) nm result from the α -Fe₂O₃. The band at 580 nm, which is related to 2.2 eV, is indicative of the band gap of the α -Fe₂O₃. This 680 nm band is due to the 3d-3d excitation of Fe⁺³ in α -Fe₂O₃. The presence of Al reveals a change in band gap from 2.1 eV to 2.4 eV, which is consistent with the results obtained by Shine et al. [69]

Table 3.2: UV-vis peaks at nm for various percentages of Al in Al- α -Fe₂O₃ nanomaterial

% of Al in Al- α -Fe ₂ O ₃	UV-vis peaks in nm
30% Al	407, 498 broad, 620 broad, 777, 802, 920, 995
20% Al	546, 573, 624 broad, 721, 735, 748, 815 broad
10% Al	403, 503 broad, 594 broad, 674 broad, 734, 786
0.5% Al	381, 409 broad, 486 broad, 595 broad, 709 broad, 850 broad

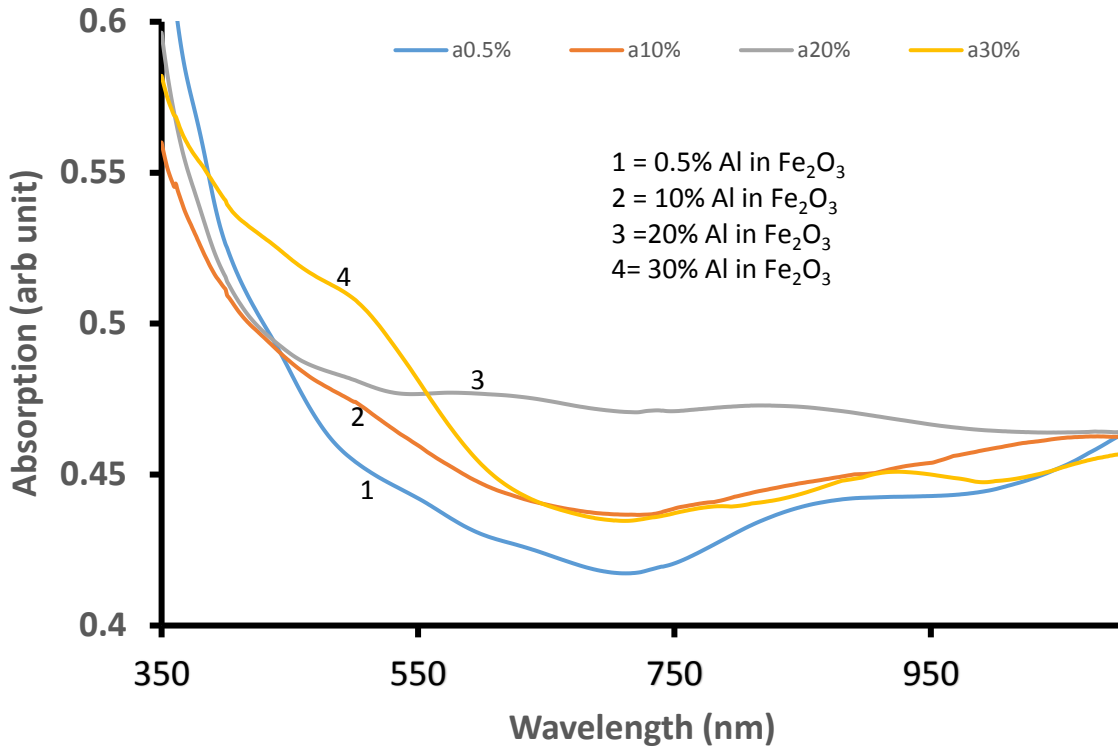


Figure 3.2 UV-vis absorption spectra of Al- α -Fe₂O₃

3.3.2 Scanning Electron Microscopy (SEM)

Figure 3 shows SEM images of Al- α -Fe₂O₃ nanomaterial film as a function of various percentages of Al. The images show the uniform distribution of Al- α -Fe₂O₃ nanoparticles. The images of Al- α -Fe₂O₃ nanomaterials for the varying Al doping is increased from 0.5% to 30%. This reveals that the size of the particles changes by increasing the aluminum in the α -Fe₂O₃ structure. 30% Al is not able to change the polycrystalline structure of α -Fe₂O₃, which does not interact at molecular level. The increase of Al ions shows clustering and/or compact formation of Al - α -Fe₂O₃. The clustering in the structure shows an increase in Al content in the structure of Al- α -Fe₂O₃ nanomaterial films.

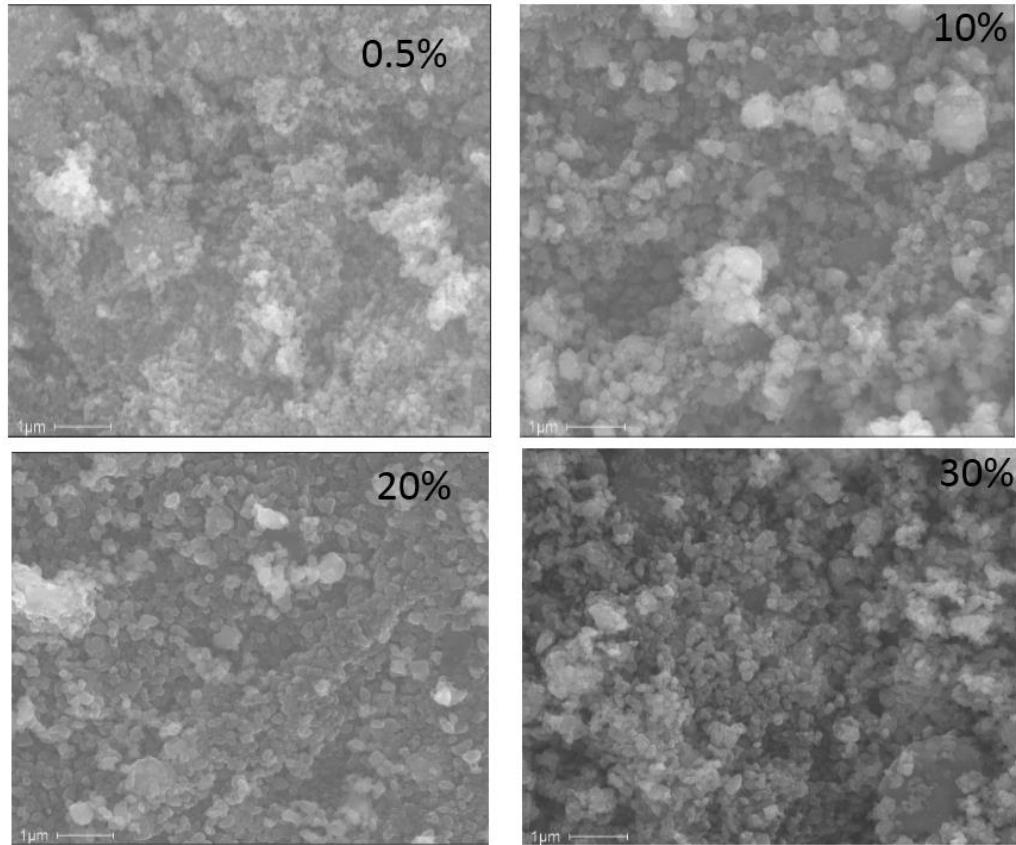


Figure 3.3 Scanning electron micrographs (SEM) of Al doped α -hematite. The percentage of doping of Al in Al- α -Fe₂O₃ is shown.

3.3.3 X-Ray Diffraction (XRD)

Figure 4 depicts the x-ray diffraction study of various Al doped Al- α -Fe₂O₃ nanomaterial films, and Table 3 shows X-ray diffraction 2θ in degrees for various percentages of Al in Al- α -Fe₂O₃ nanomaterial. It is clear from the X-ray diffraction pattern that the α -Fe₂O₃ has a polycrystalline structure. The Al ion incorporation in the structure does not cause lattice distortion in the Fe₂O₃ film. The structure, due to Al ions, forms a rhombohedral crystalline structure [69]. The small and wider X-ray diffraction peaks are a result of cluster-point defects in the structure of Al- α -Fe₂O₃ nanomaterial films.

Table 3.3: X-ray diffraction for various percentages of Al in Al- α -Fe₂O₃ nanomaterial

% Al in Al- α -Fe ₂ O ₃	X-ray diffraction 2 θ in degree
30%	31.05, 33.07, 35.61, 45.43
20%	24.11, 31.5, 33.09, 35.61, 45.41, 49.37, 53.97
10%	31.67, 33.05, 35.57, 45.37
0.5%	24.13, 31.69, 33.15, 35.61, 45.45, 49.43, 54.13, 62.49

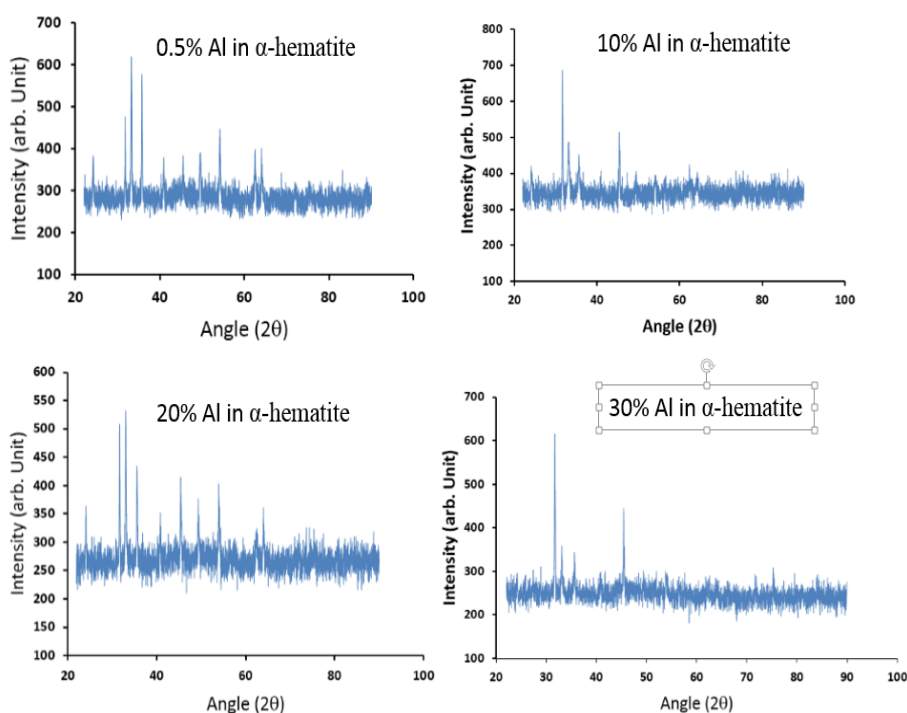


Figure 3.4 X-ray diffraction pattern of Al- α -Fe₂O₃

3.3.4 Fourier Transform Infrared Spectroscopy (FTIR)

FTIR spectra of α -Fe₂O₃ is shown in Figure 5. Curve 1 this figure shows FTIR peaks of α -Fe₂O₃ at 3414, 3029, 2934, 2843, 1637, 1497, 1446, 902, 748, 697, 553 and 474 cm⁻¹. The α -Fe₂O₃ material is related to hydroxyl OH groups at 3414 cm⁻¹ due to ν (OH) stretching, while 1627 cm⁻¹ is due to δ (OH) vibration. The band at 553 cm⁻¹ is due to Fe-O vibration mode in Fe₂O₃, and the

bands at 697 cm^{-1} and 474 cm^{-1} result from lattice defects in Fe_2O_3 [81, 82]. Curve 2 shows FTIR peaks of $\text{Al-}\alpha\text{-Fe}_2\text{O}_3$ at 3400, 3100, 3088, 2925, 2846, 1869, 1809, 1744, 1637, 1602, 1493, 1451, 1387, 1181, 1092, 1065, 841, 758, 702, 544 and 479 cm^{-1} . The presence of doping decreases the FTIR band at 697 cm^{-1} . However, there is a marked shift of the band from 479 to 460 cm^{-1} due to Al ions. The infrared shift and the appearance of a band at 670 cm^{-1} is related to Al atom replacement of Fe in $\text{Al-}\alpha\text{-Fe}_2\text{O}_3$ films [82, 83].

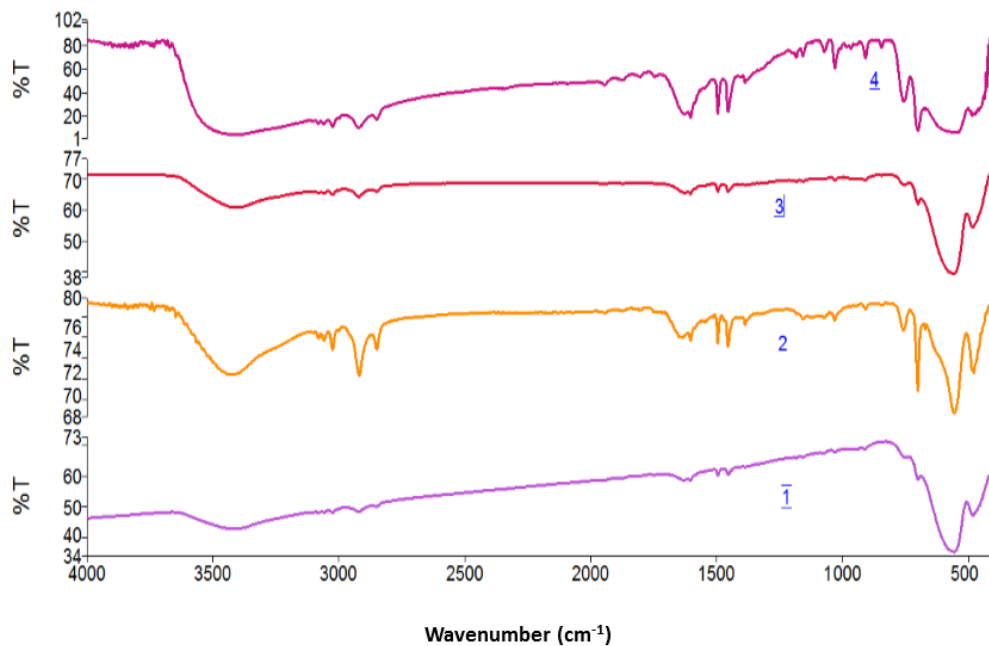


Figure 3.5 FTIR spectra of $\text{Al-}\alpha\text{-Fe}_2\text{O}_3$. Each curve shows the presence of aluminum with Fe_2O_3 given as: curve 1 = $\alpha\text{-Fe}_2\text{O}_3$, Curve 2 = 0.5% $\text{Al-}\alpha\text{-Fe}_2\text{O}_3$, Curve 3 = 20% $\text{Al-}\alpha\text{-Fe}_2\text{O}_3$ and Curve 4 = 30% $\text{Al-}\alpha\text{-Fe}_2\text{O}_3$.

3.4 Electrochemical Studies

3.4.1 Cyclic Voltammetry

The set-up of electrochemical measurements has been adopted similar to our earlier publications on hybrid films [84, 85]. Figure 6 shows cyclic voltammetry (CV) studies of 20% $\text{Al-}\alpha\text{-Fe}_2\text{O}_3$ in 1M NaOH in a three-electrode configuration of an electrochemical setup, with platinum (Pt) as a reference and Ag/AgCl as a reference electrode. The figure indicates an increase in

electrochemical properties as a function of Al content (Table 4). While Al ions induce the electrochemical properties, the CV indicates that films are highly conductive for a voltage of approximately 1.5 V; however, it is due to the oxidation of water.

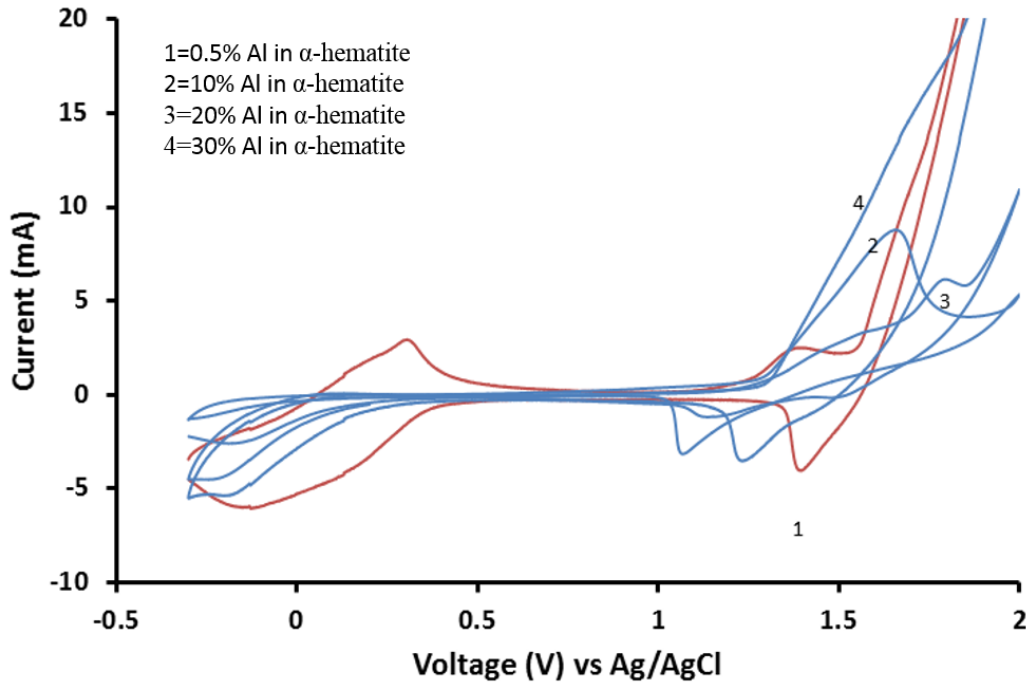


Figure 3.6 Cyclic voltammetry of Al- α -Fe₂O₃ in 1M NaOH in three electrodes with platinum as reference and Ag/AgCl as reference electrode

Figure 7 shows CV of 20% Al- α -Fe₂O₃ in 1M NaOH in a three-electrode setup with Pt as the reference and Ag/AgCl as the reference electrode. The figure clearly shows the reverse properties of the Al- α -Fe₂O₃ material in the 1 M NaOH based electrolyte. It is clear from the figure two oxidation and two reduction peaks exist. The diffusion coefficient has been calculated for using a peak current for a reversible cyclic voltammetry, which is given by Randles-Sevcik (Eq. 3),

$$I_p = (2.69 \times 10^5) n^{3/2} A C D^{1/2} \nu^{1/2} \quad \text{Eq. 3}$$

where n = number of electrons, A = electrode area (cm²), C = concentration (mol/cm³), D = diffusion coefficient (cm²/s) and ν = potential scan rate (V/s).

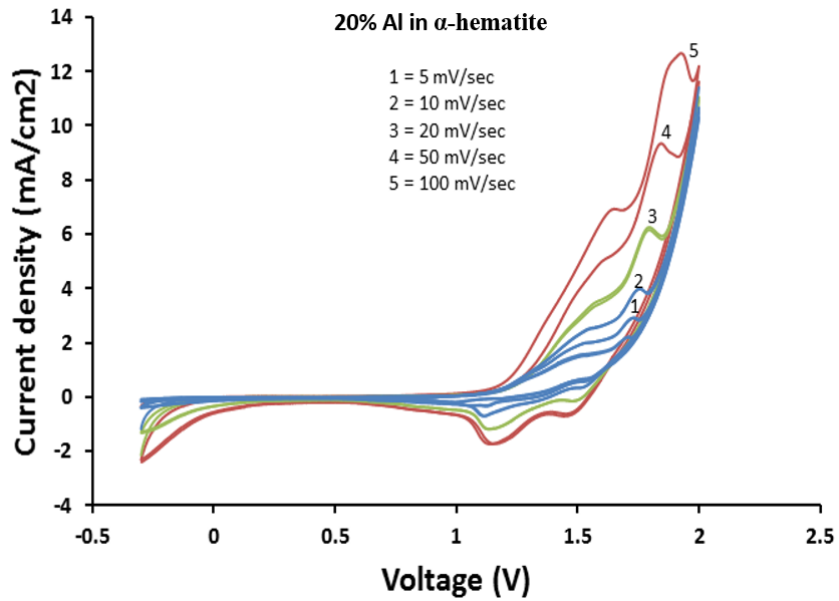


Figure 3.7 Cyclic voltammety of 20% Al- α - Fe_2O_3 in 1M NaOH in three electrodes with platinum as reference and Ag/AgCl as reference electrode

Figure 8 shows the variation of current (A) vs scan rate $(\text{V}/\text{sec})^{1/2}$ for 20% Al- α - Fe_2O_3 in 1M NaOH in a three-electrode setup with platinum counter and Ag/AgCl as a reference electrode. The diffusion coefficient has been estimated to be $0.03 \times 10^{-14} \text{ cm}^2/\text{sec}$.

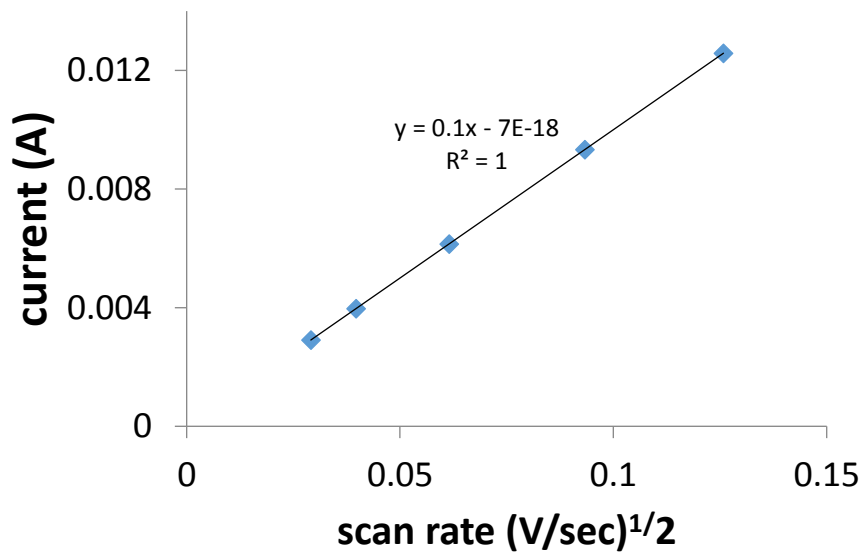


Figure 3.8 Cyclic voltammety of Al- α - Fe_2O_3 with and without light in 1M NaOH in three electrodes with platinum as reference and Ag/AgCl as reference electrode.

Figure 9 shows the CV of Al- α -Fe₂O₃ with and without light in 1M NaOH in a three-electrode setup with platinum as a reference and Ag/AgCl as the reference electrode. The voltammogram is reference and Al- α -Fe₂O₃/on ITO or steel is the working electrode. The CV studies were made with and without light. The figure clearly shows photocurrent effects with a marked increase in the current due to a photocatalytic effect on Al- α -Fe₂O₃.

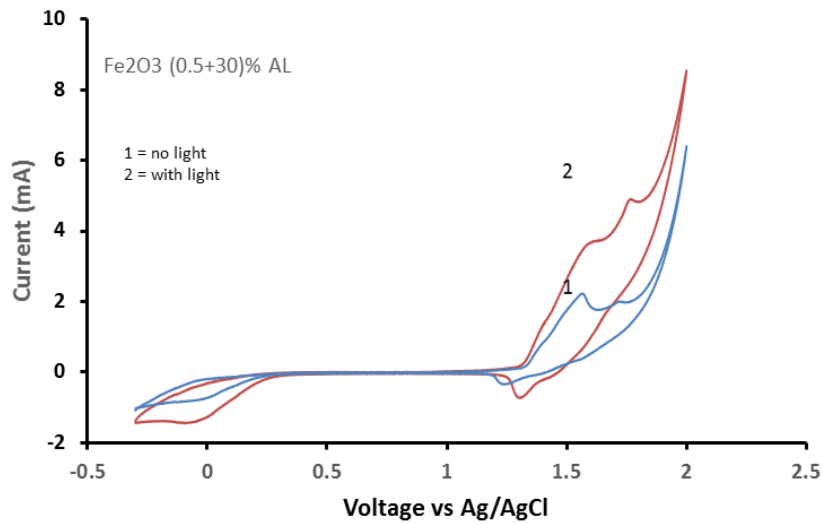
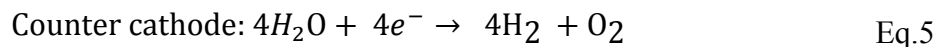
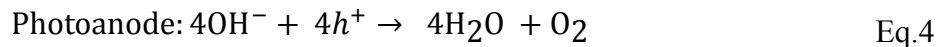


Figure 3.9 Variation of current (A) vs scan rate (V/sec)^{1/2} for 20% Al- α - Fe₂O₃ in 1M NaOH in three electrodes with platinum as reference and Ag/AgCl as reference electrode

3.4.2 Schematic of Hydrogen Production

The onset for the splitting of water is shown to be in the range of 1.3 to 2 volts [86]. The effect is also checked using chronoamperometry with an applied potential of 1.23V to 1.7 V between anode and cathode with reference to Ag/AgCl. The photocurrent can be clearly distinguishable with and without light between 1.23 to 2 volts.

The process of water oxidation and hydrogen production has been studied [57, 87] and Al- α -Fe₂O₃ will have a similar production of hydrogen in water as shown in Eq. 4 and 5.



The Al- α -Fe₂O₃ is used for hydrogen evolution in 1 M NaOH-based electrolyte. The cathode side shows the production of hydrogen, and an attempt was made to include the band diagram of the photocatalytic cells and hydrogen production based on earlier studies only for Al- α -Fe₂O₃ [57, 87]. The effect of the band gap has a profound influence on the production of hydrogen as shown in the schematic in Figure 10.

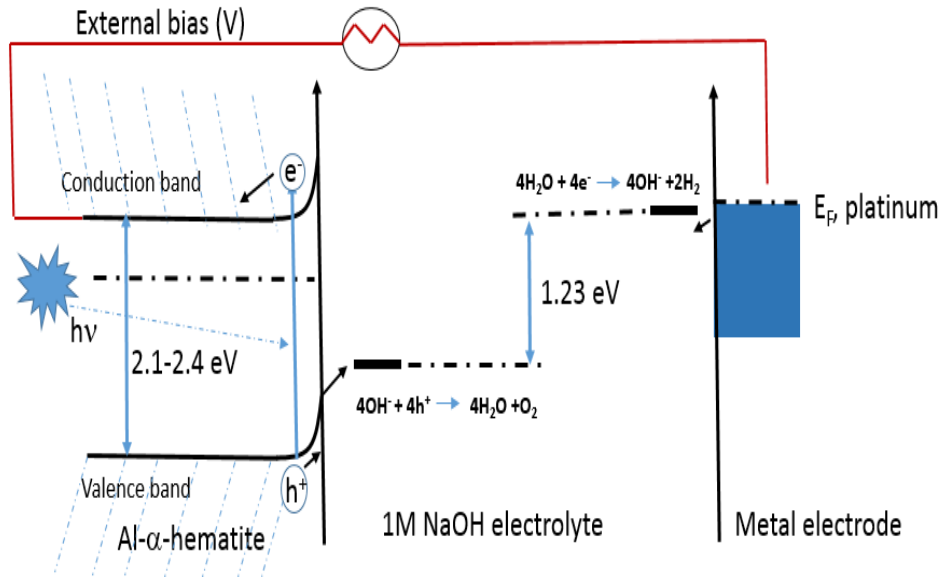


Figure 3.10 Schematic of hydrogen production using Al- α -Fe₂O₃ photocatalyst in 1 M NaOH

3.5 Conclusion

The synthesized Al- α -Fe₂O₃ observes the bandgap between 2.1 eV to 2.4 eV. The increase of Al contents in α -Fe₂O₃ shows clustering due to the denser formation of the Al- α -Fe₂O₃ particle. The structure of aluminum doping as well as composite formation due to a high percentage of Al shows a rhombohedra structure. The small, wider peaks introduced in Al- α -Fe₂O₃ are a result of a cluster-point defect. However, there is a marked shift of the band at 479 cm⁻¹ due to the presence of aluminum in α -Fe₂O₃. The photocurrent can be clearly distinguishable with and without light between 1.23 and 2 volts. We are at present researching the photoelectrochemical properties of MoS₂ composite with α -Fe₂O₃ nanomaterials to further enhance the photocurrent in the α -Fe₂O₃

photocatalyst. The Al- α -Fe₂O₃ nanostructured thin film provides easy production of hydrogen using the PEC water-splitting process, which could reveal a possible renewable energy application in future.

CHAPTER 4: MOLYBDENUM DISULFIDE α -HEMATITE-NANOCOMPOSITE FILMS FOR PHOTOELECTROCHEMICAL APPLICATIONS²

4.1 Introduction

Photoelectrochemical cells (PEC) produce hydrogen through the splitting of water using renewable sources such as the sun and water [57, 68, 88]. Photoelectrochemical (PEC) cells have been used to transform solar energy to hydrogen gas by splitting water into hydrogen and oxygen, hence offering clean and renewable energy [89]. Moreover, photoelectrochemical cells (PEC) have attracted attention since the first application of titanium dioxide (TiO_2) by Honda and Fujishima in 1972 [90]. Nevertheless, the large bandgap of TiO_2 (3.1–3.3 eV) inhibits visible light absorption which confines the efficiency of solar-to-hydrogen conversion efficiency to 2.2% [90]. So, it is necessary to use material that has a small band gap and easy to harvest energy using sunlight (visible light 53%) [91]. Iron oxide, bismuth vanadate, tungsten oxide, and tantalum nitride are examples of low band gap semiconducting materials [90]. $\alpha\text{-Fe}_2\text{O}_3$ is one of the most attractive photo-anode materials with an efficiency of 16% to convert solar-to-hydrogen energy [70, 90, 92-98]. The $\alpha\text{-Fe}_2\text{O}_3$ has been used for photoelectrochemical applications due to its optical properties, low bandgap (2.1–2.2 eV), low cost, nontoxicity, high chemical stability, and abundance in nature [90]. However, $\alpha\text{-Fe}_2\text{O}_3$ also has several drawbacks such as shorter hole diffusion length, low conductivity, shorter life time of photoexcitation, and deprived reaction kinetics of oxygen

² This chapter has been published “Alrobei, H., A. Kumar, and M.K. Ram, A New Insight in the Physical and Photoelectrochemical Properties of Molybdenum Disulfide Alpha-Hematite Nanocomposite Films. American Journal of Analytical Chemistry, 2017. 8(08): p. 523” and copyright permission in appendix A.2

evolution in photoelectrochemical applications [26]. The doping with several metallic ions such as zinc [99], titanium [100, 101], molybdenum [102], aluminum [74], platinum [47], silicon [103-105], graphene [106, 107], and cadmium sulfide [108] has shown improved PEC performance. The zinc and aluminum doped α -Fe₂O₃ has shown enhanced photoelectrochemical properties compared to α -Fe₂O₃ nanostructures [109-111].

Recently, two-dimensional (2D) dichalcogenide material, molybdenum disulfide (MoS₂), with a bandgap of 1.8 eV, has been used as n- and p-types structures for photoelectrochemical studies [90]. The MoS₂ shows stimulating photocatalytic activity due to its bonding, chemical composition, doping, and nanoparticle growth on various film matrices, and has been used for hydrogen production in nanocluster structures [88, 112-115]. Additionally, MoS₂ produces various applications in photocatalysts, phototransistors, and sensor applications [90]. It is understood that MoS₂ could play a central role in charge transfer with slow recombination of electron-hole pairs due to photo- energy with the charge transfer rate between surface and electrons [116].

Under this work, MoS₂ particles were used to promote electron transport properties of the α -Fe₂O₃ nanomaterial using doping and homogenous structure formation as MoS₂- α -Fe₂O₃ nanomaterials. The doping of MoS₂ particles varied by 0.1%, 0.2%, 0.5%, 1%, 2% and 5% in α -Fe₂O₃. The X-ray diffraction, SEM, FTIR, Raman spectroscopy, particle analyzer, and UV-vis techniques were used to characterize various percentages of MoS₂ in MoS₂- α -Fe₂O₃ nanomaterials. The electrochemical and photoelectrochemical studies were performed on MoS₂- α -Fe₂O₃ nanostructures by cyclic voltammetry (CV) and impedance measurements for water-splitting applications.

4.2 Experimental Details

4.2.1 Materials

The materials iron chloride (FeCl_3), aluminum chloride (AlCl_3), sodium hydroxide (NaOH), MoS_2 , and ammonium hydroxide (NH_4OH) were procured from Sigma-Aldrich. The $\sim 10 \Omega$ resistance of fluorine tin oxide (FTO) coated glass was purchased also from Sigma-Aldrich. The synthesized MoS_2 - α - Fe_2O_3 nanomaterials were cleaned using centrifuged containers.

4.2.2 Experimental Procedure

The sol-gel technique was used to synthesize both α - Fe_2O_3 and various compositions of MoS_2 - α - Fe_2O_3 nanomaterials. Equation 1 shows the synthesis process of MoS_2 - α - Fe_2O_3 nanomaterials. Table 1 observes the types and amounts of chemicals used in the synthesis of MoS_2 - α - Fe_2O_3 . Different concentrations of FeCl_3 with MoS_2 were prepared in 500 ml round bottom flasks. The solution was stirred for one hour after the addition of the NaOH solution. The chemical reaction continued at 90-100 °C after the round bottom flask was connected to a condenser. The reaction was held for 24 hours and then allowed to cool at room temperature. The centrifuge was used to separate the synthesized nanomaterial with the use of sufficient water. Initially, the material was left to dry at room temperature for one day. The synthesized materials containing different ratios of α - Fe_2O_3 to MoS_2 in MoS_2 - α - Fe_2O_3 were obtained. Figure 1 shows the photographs of the MoS_2 - α - Fe_2O_3 materials synthesized using various percentage of MoS_2 to α - Fe_2O_3 . The immediate doping of 0.1% MoS_2 changes the color of α - Fe_2O_3 , whereas the dark red color can be visualized with the increase of MoS_2 percentage in α - Fe_2O_3 . The each synthesized MoS_2 - α - Fe_2O_3 nanomaterial was dried for one hour at various temperatures (100, 200, 300, 400, and 500 °C). The materials were allowed then cooled at room temperature to obtain the dry powder. The nanomaterials were characterized using various physical techniques, and electrodes on conducting

substrates were prepared to study the electrochemical and photochemical properties of MoS_2 - α - Fe_2O_3 .

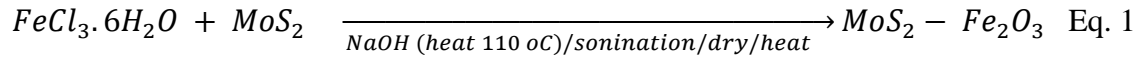


Table 4.1: Amount of chemical used for synthesis of MoS_2 -composite α -hematite

Chemicals	0.1% MoS_2	0.2% MoS_2	0.5% MoS_2	1% MoS_2	2% MoS_2	5% MoS_2
	w.r.to	w.r.to	w.r.to	w.r.to	w.r.to	w.r.to
	FeCl_3	FeCl_3	FeCl_3	FeCl_3	FeCl_3	FeCl_3
FeCl_3	6.8 g	6.8 g	6.8 g	6.8 g	6.8 g	6.8 g
MoS_2	0.013 g	0.026 g	0.065 g	0.1296 g	0.2592 g	0.648 g
NaOH	4.8 g	4.8 g	4.8 g	4.8 g	4.8 g	4.8 g
$\text{C}_{19}\text{H}_{42}\text{BrN}$	0.5 g	0.5 g	0.5 g	0.5 g	0.5 g	0.5 g

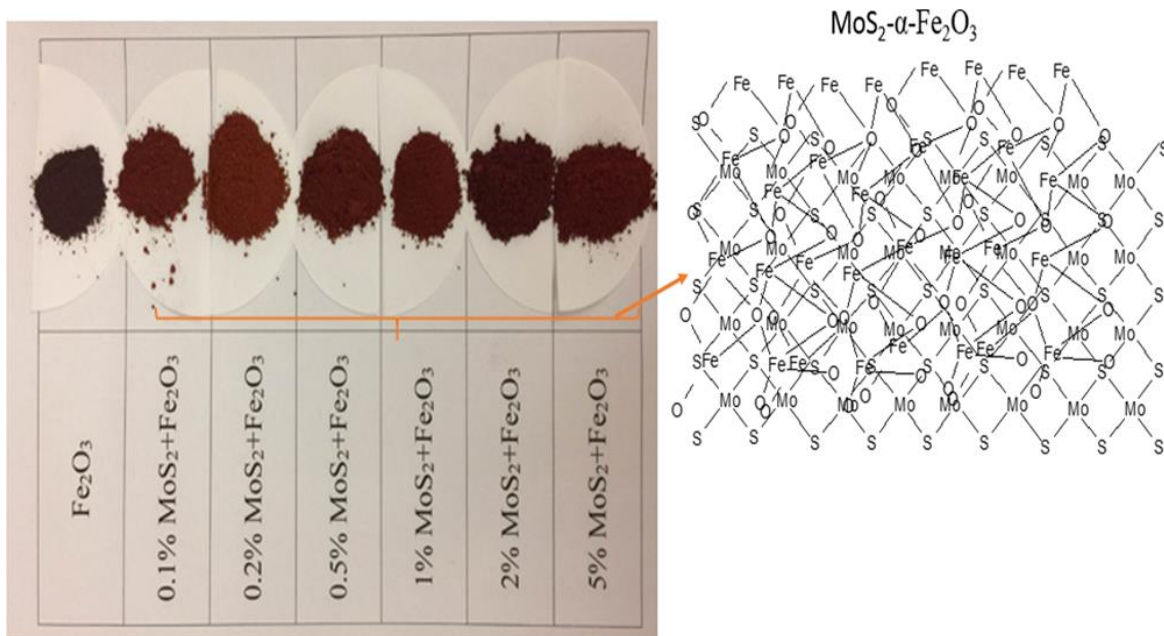


Figure 4.1 Synthesized α -hematite (α - Fe_2O_3) and MoS_2 - α - Fe_2O_3 composite materials

4.2.3 Film Formation of Substrate

The thin film of $\text{MoS}_2\text{-}\alpha\text{-Fe}_2\text{O}_3$ was fabricated on various FTO coated glass plates and silicon substrates using acetic acid. Initially, the acetic acid was used to prepare a homogenous paste of $\text{MoS}_2\text{-}\alpha\text{-Fe}_2\text{O}_3$ nanomaterial. 500 mg of $\text{MoS}_2\text{-}\alpha\text{-Fe}_2\text{O}_3$ (0.1%, 0.2%, 0.5%, 1%, 2%, and 5%) was ground and 10 ml acetic acid was applied and left for 10 hours. Later, a homogenous colloidal solution containing $\text{MoS}_2\text{-}\alpha\text{-Fe}_2\text{O}_3$ in acetic acid was used to create films on quartz, silicon, and fluorine tin oxide (FTO) coated glass plates. The films were annealed at various temperatures (100, 200, 300, 400, and 500 °C) for one hour. The XRD, SEM, cyclic voltammetry, and UV-vis characterizations were performed in room temperature-cooled samples of $\text{MoS}_2\text{-}\alpha\text{-Fe}_2\text{O}_3$ films.

4.3 Physical Properties Studies

4.3.1 UV-Visible Spectroscopy (UV-Vis)

Figure 2 observes the UV-vis spectra of $\alpha\text{-Fe}_2\text{O}_3$, MoS_2 and $\alpha\text{-Fe}_2\text{O}_3\text{-MoS}_2$ -prepared at a different ratio of MoS_2 to $\alpha\text{-Fe}_2\text{O}_3$. An UV-Vis Spectrometer Jasco V-530 was used to measure the absorption spectra on various samples deposited on glass plates. Figure 2(a) shows the UV-vis absorption at approximately 550 nm for the pristine $\alpha\text{-Fe}_2\text{O}_3$, similar to that shown in literature. Figure 2(b) shows the characteristic absorption bands 388, 453, 618 and 679 nm for the MoS_2 nanomaterial film on glass plates. Figure 2 (c-f) shows the UV-vis absorption spectra for MoS_2 doped in different percentages (0.1, 0, 2, 1 and 5%) with $\alpha\text{-Fe}_2\text{O}_3$ nanomaterial. Figure 2(c) shows the absorption bands at 282, 454, 463 nm. Figure 2(d) shows the absorption bands at 446 and 565 nm. Distinct peaks can be seen at 382, 461 and 570 nm. Figure 2(e) displays the UV-vis band at 382, 456 and 559nm whereas Figure 2(f) shows the absorption band at 382, 459 and 572 nm. There is a blue shift with an increase of MoS_2 in $\alpha\text{-Fe}_2\text{O}_3$ [117]. However, the band observed for 0.1%

MoS₂ doping is shifted at 572 nm in 5% MoS₂ doping in α -Fe₂O₃ nanomaterial. Such results are consistent with the results shown of transition composite metal ions [118]. The UV-vis spectra of the composite hematite have been estimated to be 2.17 eV for the band at 572 nm.

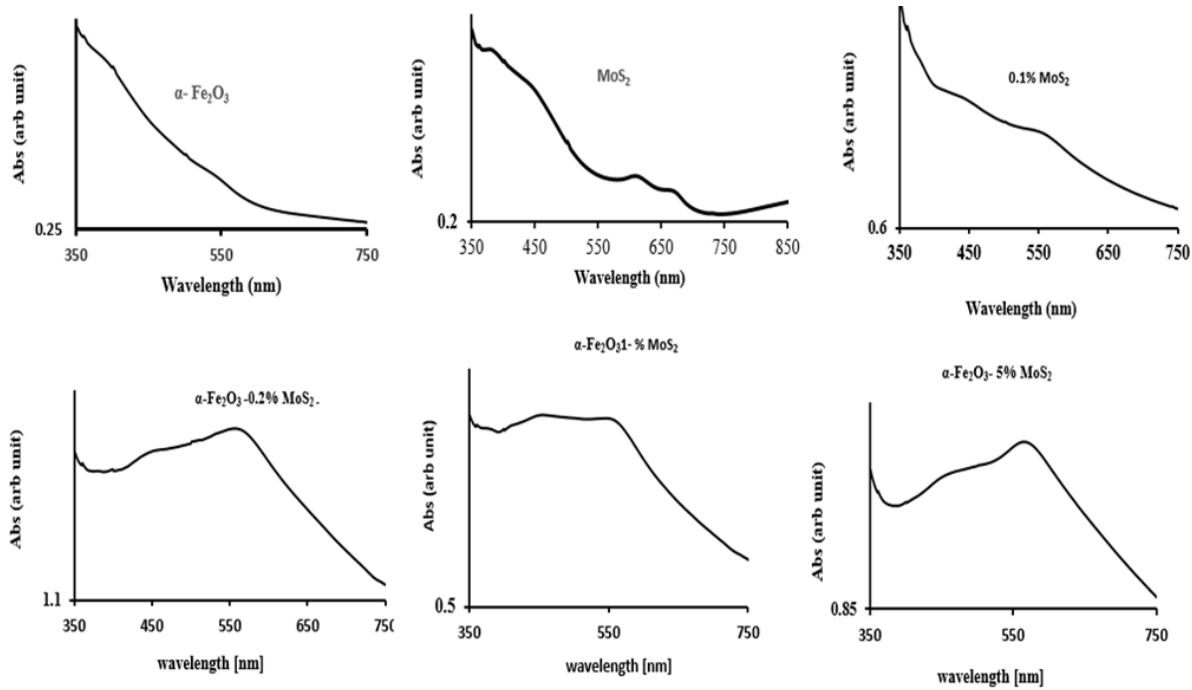


Figure 4.2 UV-vis absorption spectra of MoS₂ with α -hematite nanocomposite

4.3.2 X-Ray Diffraction (XRD)

The crystalline structure of MoS₂- α -Fe₂O₃ was investigated using Powder X-ray diffraction (XRD), model PANalytical X'Pert Pro MRD system, with Cu K α radiation (wavelength = 1.5442 Å) operated at 40 kV and 40 mA. Figure 3 shows X-ray diffraction curves for several percentages of MoS₂ (0.1%, 0.2%, 0.5%, 1%, 2%, and 5%) to α -Fe₂O₃; α -Fe₂O has a polycrystalline structure as revealed from the XRD pattern. The diffraction common peaks in MoS₂- α -Fe₂O₃ nanocomposite at different percentages of MoS₂ displays bands at 31.2°, 33.2°, 37.5°, 40.9°, 49.5°, 54.1°, 62.2°, and 64.2°. The diffraction angle peak has been indexed at (012), (104), (110), (113), (024), (116), (214), and (300) for crystal planes of hexagonal iron oxide [8]. It

is clear from sharp and strong diffraction peaks that α -Fe₂O₃ is well crystallized in the synthesis process for all percentages of MoS₂ in α -Fe₂O₃ [119]. The peak at 54.1° is due to the presence of MoS₂ in the MoS₂- α -Fe₂O₃- structure.

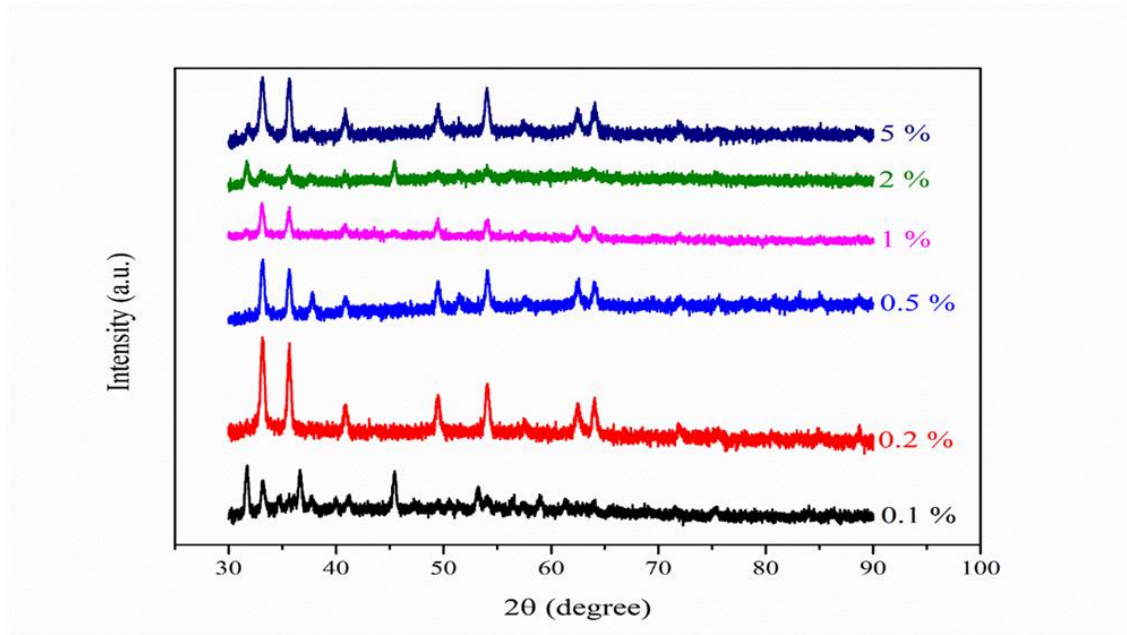


Figure 4.3 X-ray diffraction pattern of MoS₂ with α -hematite nanocomposite

4.3.3 Fourier Transform Infrared Spectroscopy (FTIR)

Perkin Elmer spectrum was utilized to study FTIR spectroscopy of various samples of MoS₂- α -Fe₂O₃- nanocomposite. The MoS₂- α -Fe₂O₃ nanocomposite was mixed with KBr, the pellets were made using the hydraulic press, and the samples were measured using the transmission mode from 400 to 4000 cm⁻¹. FTIR spectra of MoS₂- α -Fe₂O₃ shows the change of percentage of MoS₂ doping with α -Fe₂O₃ with curve 1 to 5%, curve 2 to 0.2%, curve 3 to 2%, curve 4 to 1%, curve 5 to 0.5%, and curve 6 to 0.1% of MoS₂ in MoS₂- α -Fe₂O₃ as shown in Figure 4. The infrared bands of each MoS₂ doping to α -Fe₂O₃ are shown in Table 2. The infrared band at 3414 cm⁻¹ is due to hydroxyl (OH) groups in α -Fe₂O₃. The band at 1642 cm⁻¹ results from ν (OH) stretching. The Fe-O vibration band in Fe₂O₃ is because of 562 cm⁻¹. The band at 620-654 and 474-512 are

related to the lattice defects in Fe_2O_3 [81, 82]. The infrared band at $474\text{-}512\text{ cm}^{-1}$ is due to stretching vibration depicting the presence of MoS_2 in the $\text{MoS}_2\text{-}\alpha\text{-Fe}_2\text{O}_3$ structure. The doping of 0.1% to 5% of MoS_2 shifts the infrared band from 512 cm^{-1} to 474 cm^{-1} . The band at 474 cm^{-1} is the band observed for exfoliated MoS_2 nanosheets revealing the maximum doping in $\text{MoS}_2\text{-}\alpha\text{-Fe}_2\text{O}_3$ structure [120].

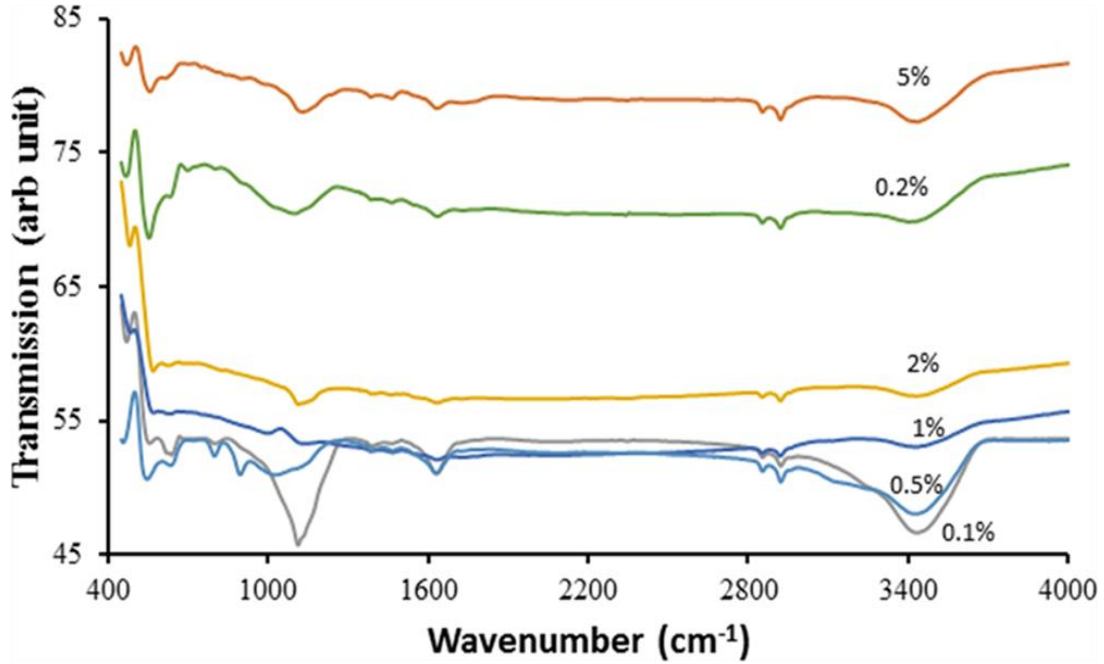


Figure 4.4 FTIR spectra of MoS_2 with α -hematite nanocomposite

Table 4.2: Infrared bands of each MoS_2 doping to $\alpha\text{-Fe}_2\text{O}_3$

MoS_2	Wavenumber (cm^{-1})
5%	474, 562, 620, 1136, 1193, 1472, 1642, 2858, 2924, 3436
2%	484, 562, 620, 1136, 1193, 1472, 1642, 2858, 2924, 3436
1%	474, 570, 640, 1006, 1134, 1388, 1470, 1670, 2854, 2924, 3436
0.5%	458, 554, 644, 802, 898, 1042, 1386, 1468, 1634, 2856, 2922, 3438
0.1%	512, 522, 654, 802, 1114, 1396, 1434, 1666, 2836, 2952, 3448

4.3.4 Scanning Electron Microscopy (SEM)

The scanning electron microscopy (SEM) of various $\text{MoS}_2\text{-}\alpha\text{-Fe}_2\text{O}_3$ samples were measured using FE-SEM, S-800, and Hitachi. Figure 5 shows SEM images of $\text{MoS}_2\text{-}\alpha\text{-Fe}_2\text{O}_3$ nanomaterials which consisted of various percentages from 0.1 to 5 % MoS_2 to Fe_2O_3 in $\text{MoS}_2\text{-}\alpha\text{-Fe}_2\text{O}_3$. SEM images reveal that the morphology of $\text{MoS}_2\text{-}\alpha\text{-Fe}_2\text{O}_3$ resembles blooming flower-like nanoparticles. The blooming flower-like morphology is a result of doping MoS_2 with $\alpha\text{-Fe}_2\text{O}_3$ [121]. The images reveal that the size of the particle changes with the increase of MoS_2 doping from 0.1% to 5% in $\text{MoS}_2\text{-}\alpha\text{-Fe}_2\text{O}_3$ nanomaterial. In addition, it is difficult to differentiate simple $\alpha\text{-Fe}_2\text{O}_3$ nanoparticles from MoS_2 nanosheets; this shows a strong interface formation between Fe_2O_3 and MoS_2 in $\text{MoS}_2\text{-}\alpha\text{-Fe}_2\text{O}_3$ nanomaterial [122].

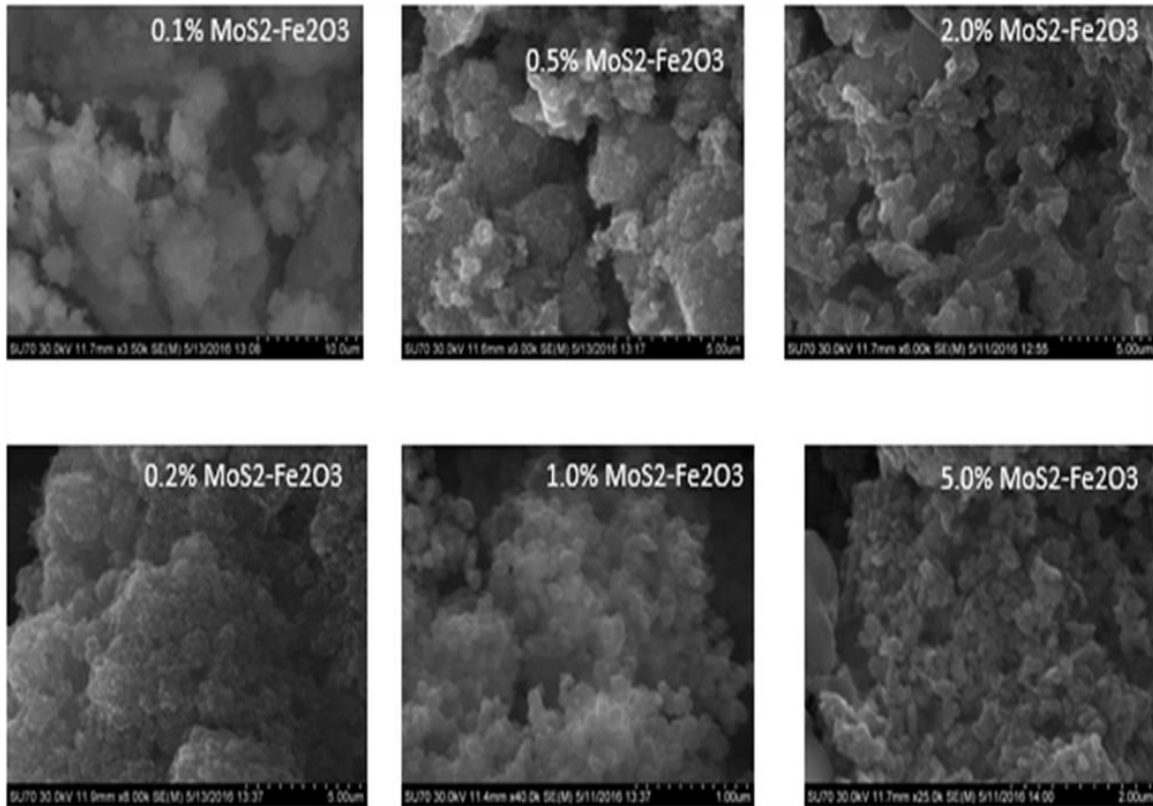


Figure 4.5 Scanning electron micrographs (SEM) of MoS_2 with $\alpha\text{-hematite}$ nanocomposite. The percentage of MoS_2 with $\alpha\text{-hematite}$ nanocomposite is shown in Figure 6.

4.3.5 Raman Spectroscopy

The Raman spectrum has been studied to understand the rapid and nondestructive surface description of vibrational characteristic bonds of MoS₂ to Fe₂O₃ in MoS₂- α -Fe₂O₃ nanomaterial. Figure 6 shows the Raman spectra of MoS₂- α -Fe₂O₃ film excited by a 532 nm laser [123]. The Raman shift at 532 cm⁻¹ resonates with the electronic transition in ring structures for aromatic clustering processes in sp² dominated particles. The shifts at 374 and 417 cm⁻¹ are due to in-plane vibrational (E_{2g1}) and the out-of-plane vibrational (A_{1g}) modes. The enhanced MoS₂ is indicative of energy difference between Raman shifts due to MoS₂ content in MoS₂- α -Fe₂O₃ nanomaterial.

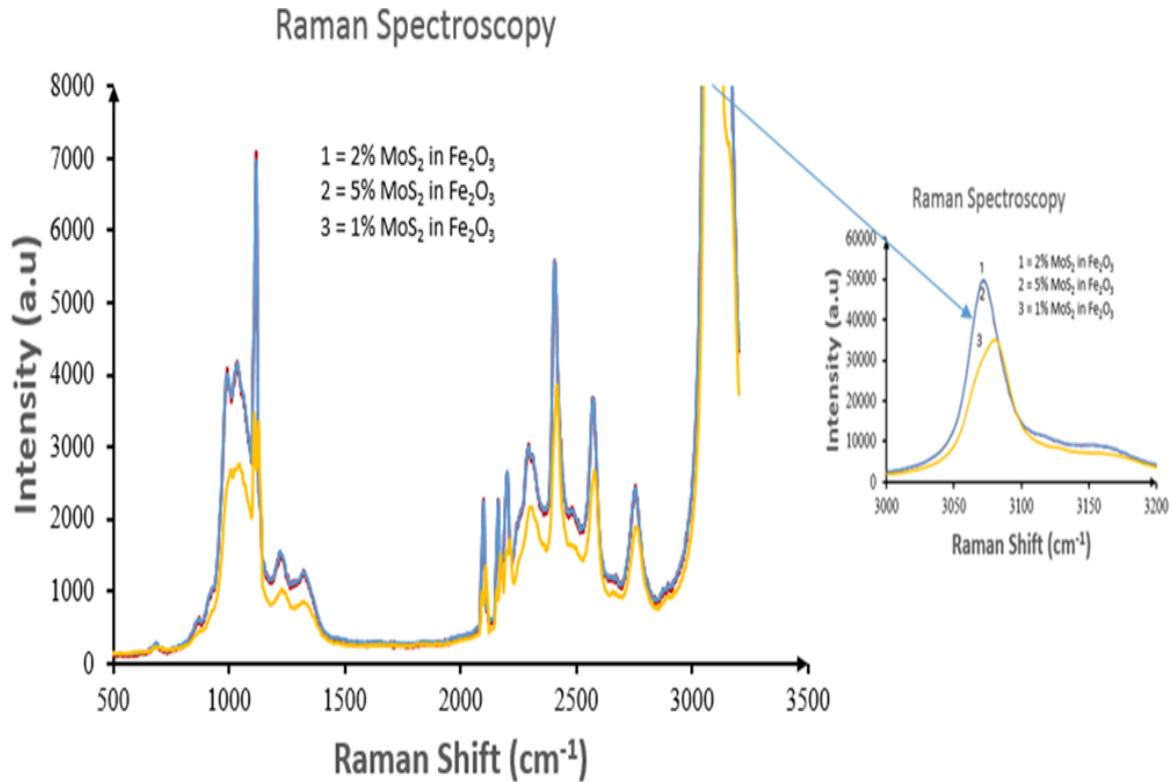


Figure 4.6 Raman spectra of MoS₂- α -Fe₂O₃ film sample and ITO substrate with various percentages of MoS₂ as shown in a and b

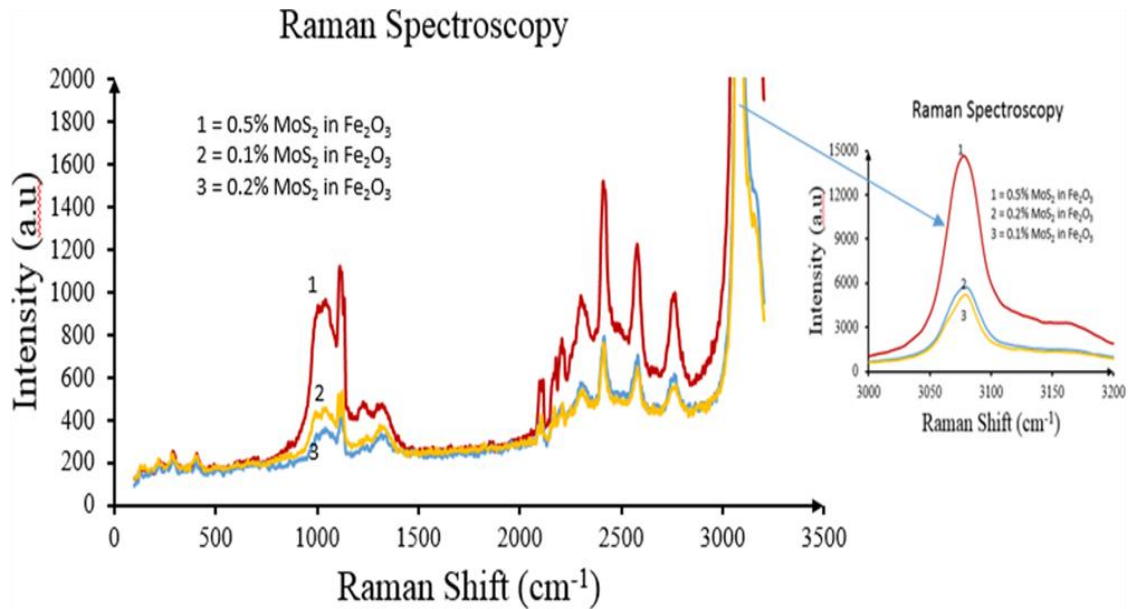


Figure 4.6 (Continued)

4.3.6 Particle Analyzer

The Zetasizer Nano particle analyzer range model was used to measure the average particle size of various MoS₂- α -Fe₂O₃ samples. Initially, the MoS₂- α -Fe₂O₃ nanomaterial was dispersed in water and ultra-sonicated to produce an aggregated free colloidal sample. Figure 7 shows the particle size of MoS₂- α -Fe₂O₃ as a function of MoS₂ doped in α -Fe₂O₃. The average particle size in the liquid sample ranges from 459 nm (0.1%) to 825 nm for (5%) the dopant of MoS₂ respectively. Although these particles are small, there are few particles which are larger than five microns. The larger particles that can be detected through SEM measurement are a result of aggregation. The average particle size is important for the fabrication of the electrodes from the particles. This information of nanomaterial dispersion of MoS₂- α -Fe₂O₃ can be exploited for electrode fabrication or other applications.

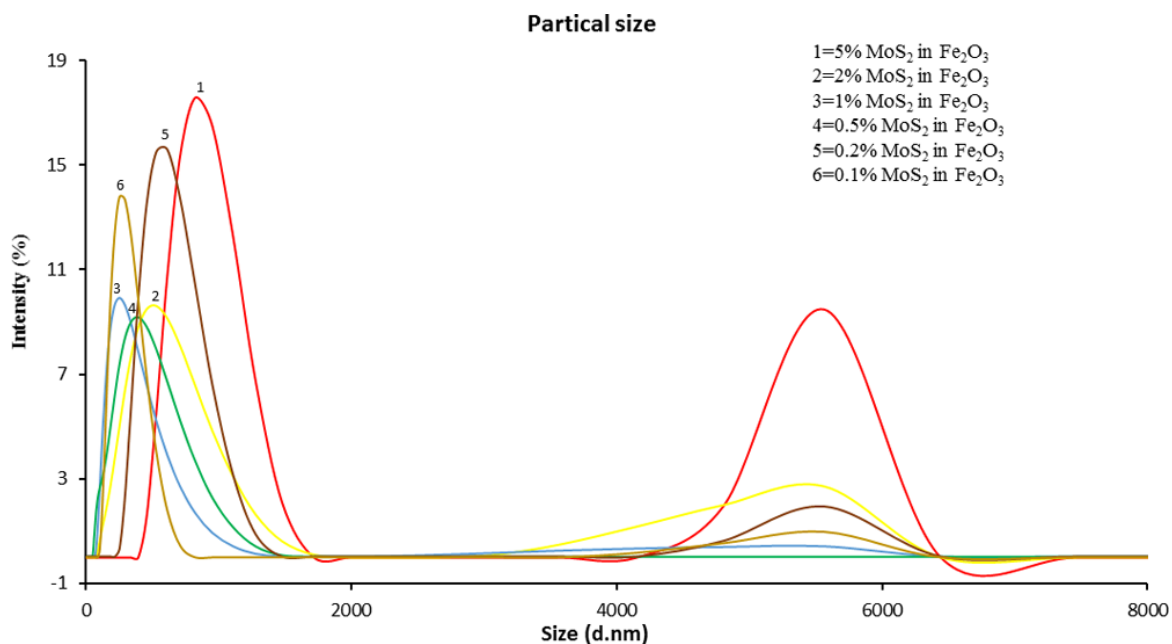


Figure 4.7 Particle size measurement of MoS₂-α-Fe₂O₃ nanocomposite materials as a function of MoS₂ dopant

4.4 Electrochemical Studies

4.4.1 Cyclic Voltammetry

The electrochemical measurements on various MoS₂-α-Fe₂O₃ electrodes were measured from an electrochemical workstation (Volta lab). The electrochemical setup was adopted similar to our earlier studies on hybrid films [84, 85]. Figure 8 shows the cyclic voltammetry (CV) of 1% MoS₂-α-Fe₂O₃ on FTO coated glass plates as a working electrode with platinum (Pt) as a reference and Ag/AgCl as a reference electrode in a three electrode-based electrochemical cell in 1M NaOH. The continuous increase of CV current was observed with an increase in function of scan rate. The presence of MoS₂ ions induces the electrochemical properties and 1.3V can be seen as the oxidation potential of water, which is less than the aluminum doped from our previous studies [30].

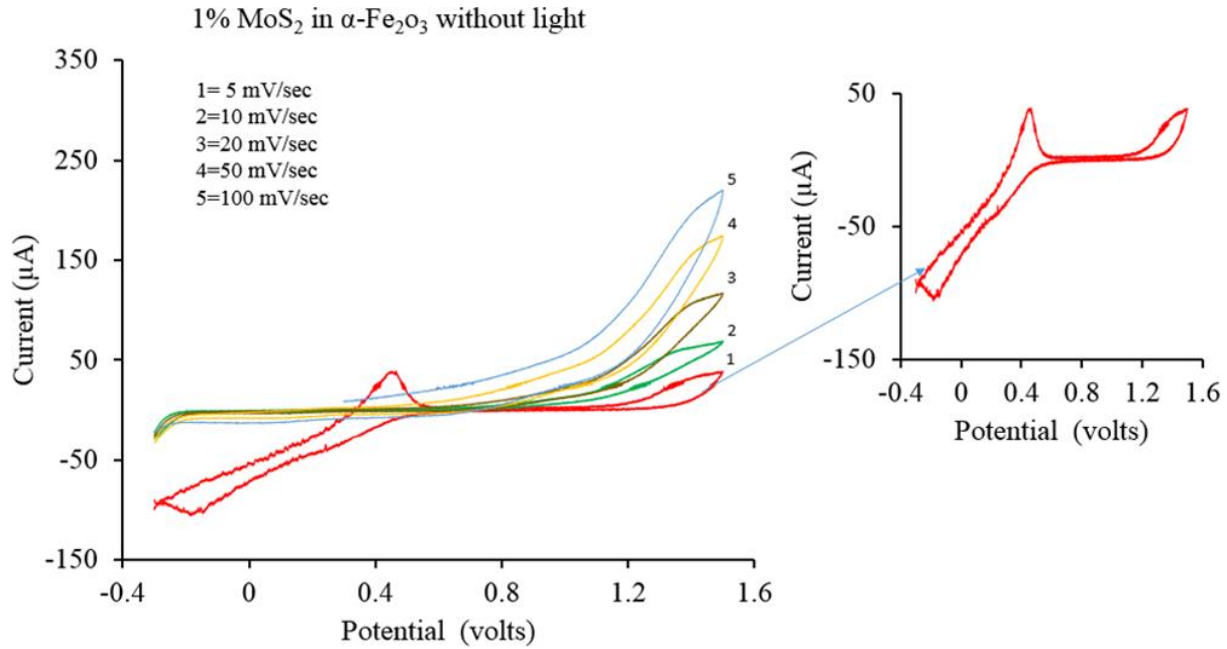


Figure 4.8 Cyclic voltammetry of 1% MoS₂ with α -Fe₂O₃ nanocomposite without light in 1M NaOH in three electrodes with platinum as reference and Ag/AgCl as reference electrode.

The CV is shown in Figure 9 with application of light simulated for solar radiation. However, with the scan rate of 100 mV/sec, a maximum photocurrent was absorbed for MoS₂- α -Fe₂O₃ film. The diffusion coefficient was calculated by using peak current for a reversible cyclic voltammetry, given by the Randles-Sevcik equation (Eq. 2)[124].

$$I_p = (2.69 \times 10^5) n^{3/2} A C D^{1/2} \nu^{1/2} \quad \text{Eq. 2}$$

where:

n = number of electrons

A = electrode area (cm²)

C = concentration (mole/cm³)

D = diffusion coefficient (cm²/s)

ν = potential scan rate (V/s)

I_p = current.

The diffusion coefficient has been calculated at 0.24×10^{-16} cm²/s.

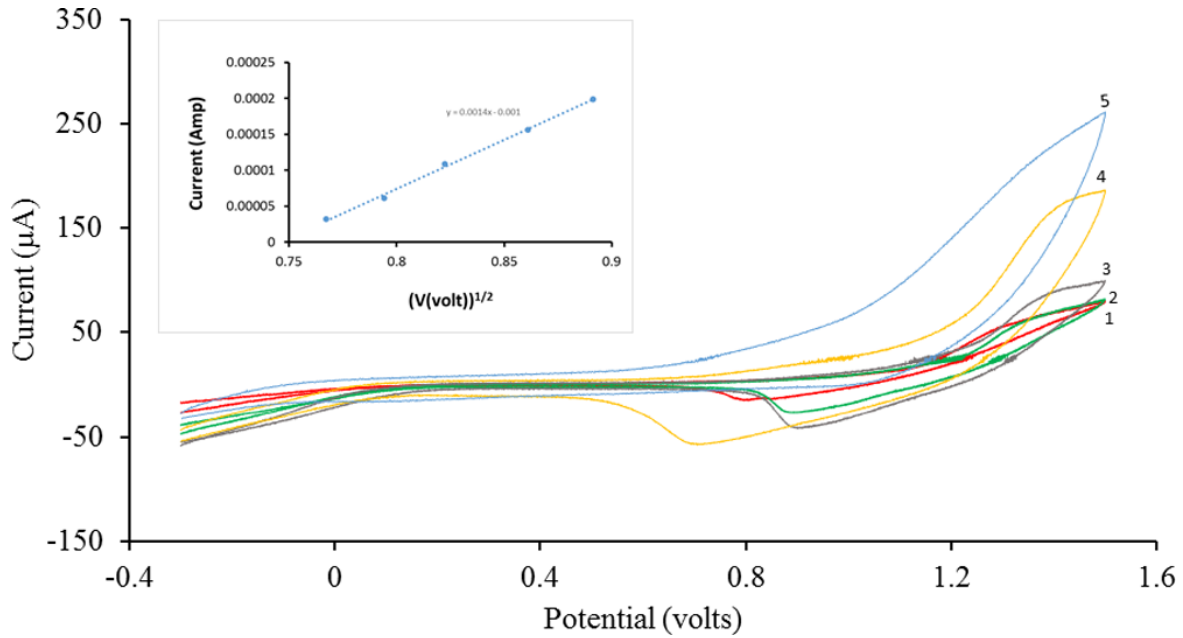


Figure 4.9 Cyclic voltammetry of 1% MoS₂ with α -Fe₂O₃ nanocomposite with light in 1M NaOH in three electrodes with platinum as reference and Ag/AgCl as reference electrode.

4.4.2 Chronoamperometry

Figure 10 (a & b) shows the chronoamperometry study of two electrode cells consisting of MoS₂- α -Fe₂O₃ film as working electrolyte and steel as the counter in various concentrations (0.01, 0.1, 1M) of NaOH-based electrolytes. The potential from -1000 mV to 1500 mV was applied, and the chronoamperometry photocurrent was studied. Figure 9 (a & b) shows the chronoamperometry photocurrent plot with $t^{-1/2}$ for oxidation and reduction processes for MoS₂- α -Fe₂O₃ film. The rise of photocurrent showed a linear relationship with $t^{-1/2}$ due to the excitation of light. The current transient was different from the excitation of light. The diffusion-controlled photocurrent is calculated using the Cottrell equation in Equation 3 [125-127].

$$i = \left[nFAD^{\frac{1}{2}}C \right] / [\pi t^{\frac{1}{2}}] \quad \text{Eq. 3}$$

where:

n = the electron participating in the reaction

F = the faraday constant

A = the area of the electrode

i = the transient current

D = the diffusion coefficient

C = the concentration of the electrolyte

The D has been estimated to be 1.057×10^{-14} cm²/sec.

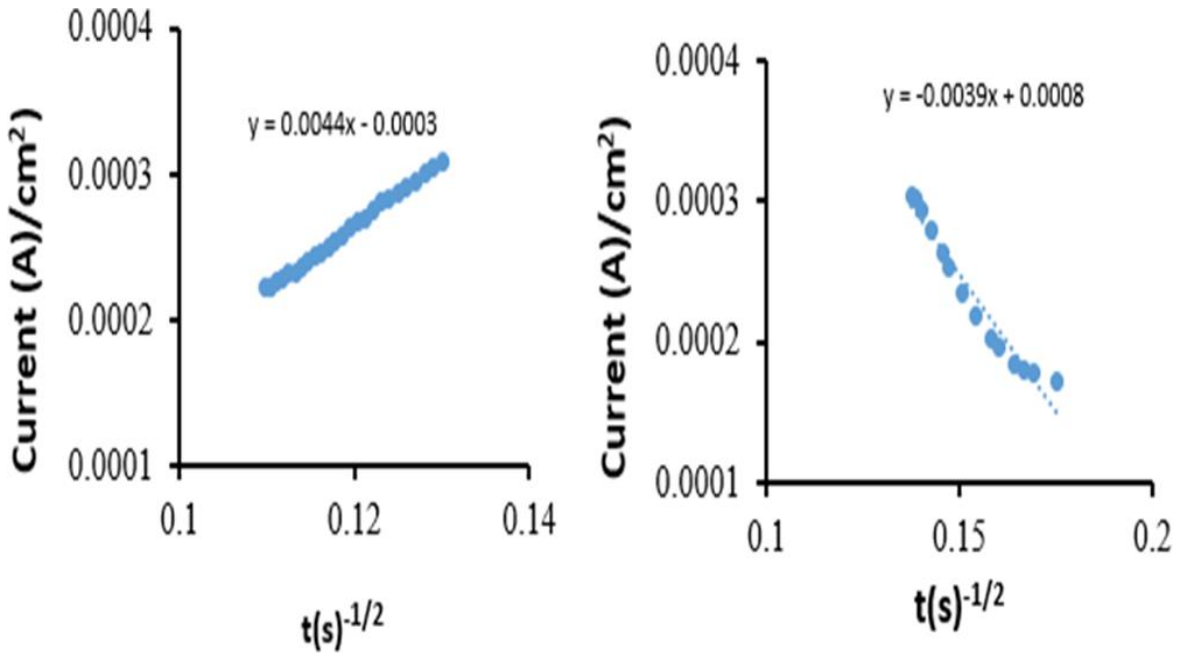


Figure 4.10 Chronoamperometry photocurrent plot with $t(s)^{-1/2}$ for oxidation and reduction processes for MoS₂- α -Fe₂O₃ film

4.4.3 Half-Sweep Potential

Figure 11 shows the half sweep potential with and without light for both aluminum-doped α -Fe₂O₃ and MoS₂- α -Fe₂O₃. Our previous study on aluminum doping has shown the photocurrent to be 35 μ A whereas the same type of electrode for MoS₂- α -Fe₂O₃ showed the current

to be 180 μA . A schottky-type current voltage is experienced for both aluminum-doped as well as MoS_2 - α - Fe_2O_3 -based electrodes in photoelectrochemical cells.

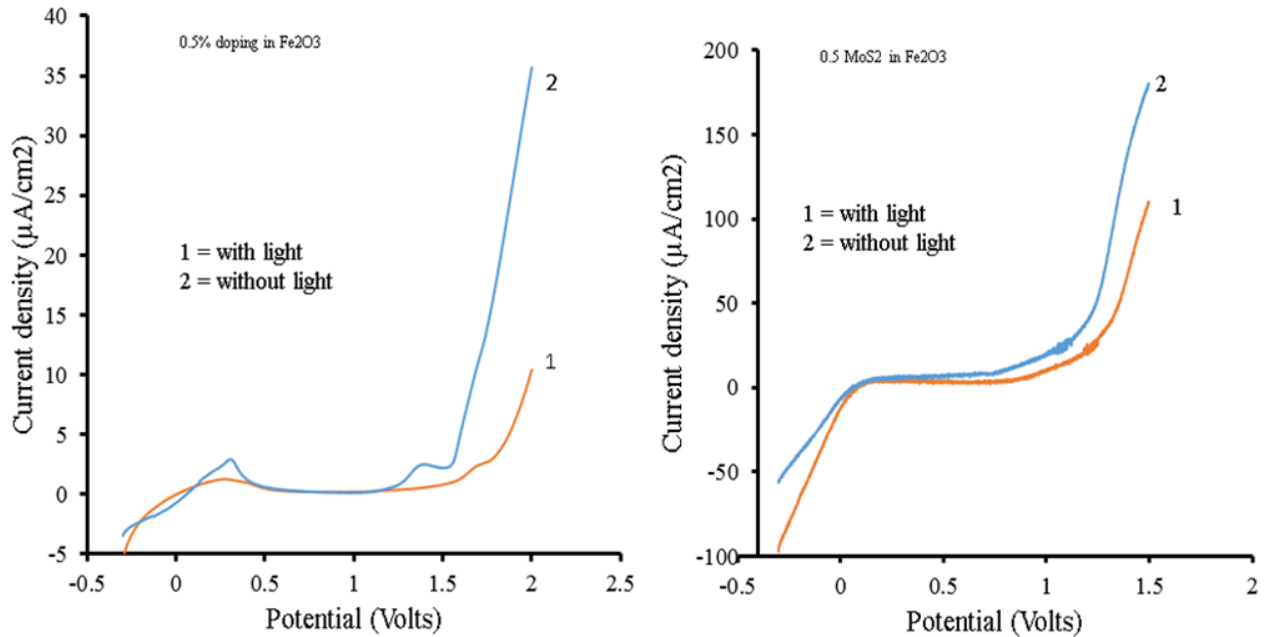


Figure 4.11 Half-sweep potential with and without light for $\text{Al-}\alpha$ - Fe_2O_3 and MoS_2 - α - Fe_2O_3 film with and without light exposure

4.4.4 Schematic of MoS_2 - α - Fe_2O_3 Reaction Process

A schematic was drawn to understand the effect of MoS_2 with α - Fe_2O_3 . Hydrogen production using MoS_2 - α - Fe_2O_3 photocatalysts in electrolytes containing 1 M NaOH is shown in a schematic in Figure 12. The band gap of MoS_2 varies from 1.8-1.9 eV, whereas the band gap of α - Fe_2O_3 is 2.1 eV. The bandgap of MoS_2 - α - Fe_2O_3 was estimated in range of 1.94 to 2.40 eV based on UV-vis measurements, which is well within the region of visible light. MoS_2 doping also increased the conductivity of the samples. The schematic in Figure 12 shows that the photogenerated electrons from the conduction band of MoS_2 are transferred to the conduction band (CB) of α - Fe_2O_3 whereas holes from α - Fe_2O_3 are transferred to the valence band (VB) of MoS_2 . This enhances the photocatalytic activity of the MoS_2 composite with α - Fe_2O_3 in MoS_2 - α - Fe_2O_3 nanomaterial-based electrodes.

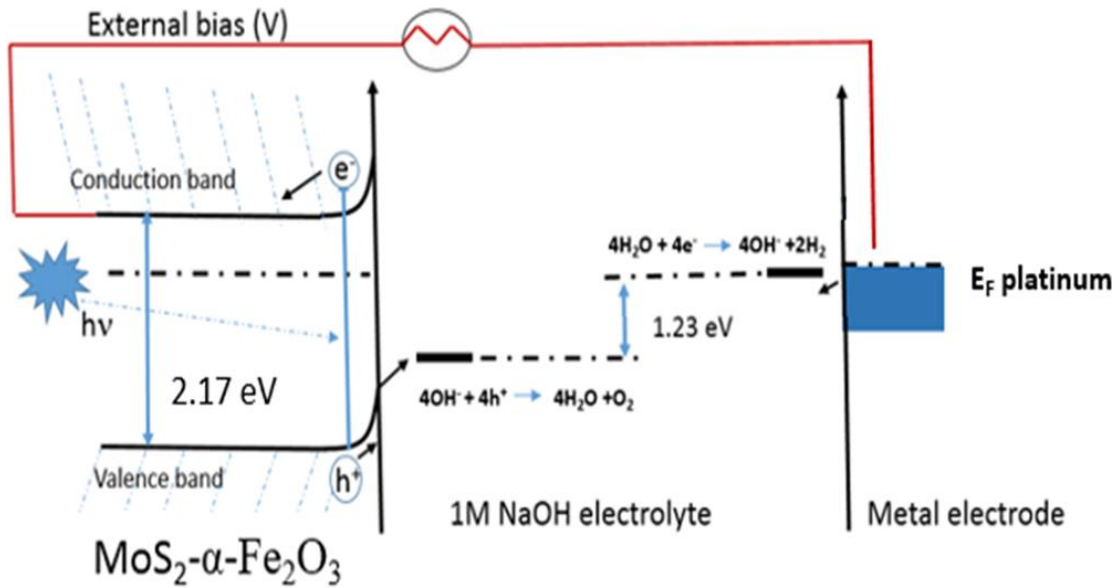


Figure 4.12 Schematic of hydrogen production using MoS_2 -composite $\alpha\text{-Fe}_2\text{O}_3$ photocatalyst in 1 M NaOH

4.5 Conclusion

The synthesized $\text{MoS}_2\text{-}\alpha\text{-Fe}_2\text{O}_3$ observed the shift in the band gap to 2.17 eV with MoS_2 doping. There is a marked change in the band due to MoS_2 doping in $\alpha\text{-Fe}_2\text{O}_3$. The increase of MoS_2 dominated the structure as marked from SEM measurements. The structure of $\alpha\text{-Fe}_2\text{O}_3$ forms a rhombohedra structure. The photocurrent is clearly distinguishable with and without light irradiation to electrodes based on $\text{MoS}_2\text{-}\alpha\text{-Fe}_2\text{O}_3$ nanomaterial. The enhanced photocurrent is observed with MoS_2 doping in $\text{MoS}_2\text{-}\alpha\text{-Fe}_2\text{O}_3$ nanomaterial. The $\text{MoS}_2\text{-}\alpha\text{-Fe}_2\text{O}_3$ nanomaterial thin film has the potential to produce hydrogen using a PEC water-splitting process that could have renewable energy applications. Our future work is based on the use of $\text{MoS}_2\text{-}\alpha\text{-Fe}_2\text{O}_3$ as n-type in p-n photoelectrochemical studies for efficient water-splitting applications.

CHAPTER 5: P-N PHOTOELECTROCHEMICAL CELL PROPERTIES USING α -HEMATITE -MOLYBDENUM DISULFIDE AS N-ELECTRODE AND POLYHEXYLTHIOPHENE (RRPHTH) - NANODIAMOND (ND) AS P-ELECTRODE³

5.1 Introduction

State of the art research has shown that tuning the band gap of photocatalytic material makes it more effective in photoelectrochemical cells for water splitting applications [57, 68, 88-91]. There are several semiconducting materials (example: Fe_2O_3 , BiVO_4 , WO_3 and Ta_3N_5) used in PEC cells with a lower band gap [90]. The α - Fe_2O_3 material as an anode has been used in the photoelectrochemical cells resulting in a water-to-hydrogen conversion efficiency of 16% of solar radiations [90, 128-131]. Also, α - Fe_2O_3 has a low bandgap (2.1–2.2 eV), low cost, high chemical stability, and nontoxic and abundant material for photoelectrochemical cells [69, 90, 102, 103, 132-136]. However, α - Fe_2O_3 has several drawbacks including shorter hole diffusion length, low conductivity, shorter lifetime of photoexcitation, and deprived reaction kinetics of oxygen evolution heralding better photo-conversion efficiency [26, 57, 137-139]. The performance of water splitting and photo-conversion has been enhanced by metallic doping such as Ti [100, 101], Mo [102], Al [74, 140], and Pt [47] and Si [103, 104]. Our earlier studies on Zn and Al doping in α - Fe_2O_3 showed enhanced photoelectrochemical properties [141]. MoS_2 is one of the most studied materials in recent years due to its classification as a 2D- dichalcogenide material having a band

³ This chapter has been communicated as “p-n photoelectrochemical cell properties using α -hematite -molybdenum disulfide as n-electrode and polyhexylthiophene (RRPHTh)-nanodiamond (ND) as p-electrode” in *Electrochimica Acta*, Elsevier Journal, April 2018

gap of 1.8-1.9 eV [90]. The MoS₂ has shown interesting photocatalytic activity because of its bonding, chemical composition, doping, and nanoparticle growth on countless matrix films [88, 105, 108, 142]. MoS₂ has applications in photocatalytic devices [11, 88], phototransistors [143-146] and sensors [90, 147-149]. Moreover, MoS₂ plays an important role as charge transfer with slow recombination of electron-hole pairs created due to photo-energy, and this relates to the charge transfer rate between surface and electrons generated in photo-conversion [116]. MoS₂ has also been used as a p-type conductor in photoelectrochemical hydrogen production in PEC cells.

Our earlier experiment using MoS₂ particles has promoted the electron transport properties of α -Fe₂O₃ nanomaterial by doping and homogenous structure. The doping of MoS₂ particles varied from 0.1%, 0.2%, 0.5%, 1%, 2% and 5% in α -Fe₂O₃ nanomaterial. The α -Fe₂O₃ and MoS₂- α -Fe₂O₃ nanomaterials were characterized using X-ray diffraction, SEM, FTIR, Raman spectroscopy, particle analysis and UV-vis spectroscopy, respectively. Cyclic voltammetry (CV) and impedance measurements were utilized to understand the electrochemical electrode and electrolyte interface and photoelectrochemical properties of MoS₂- α -Fe₂O₃. Nano-hybrid RRPHTh with various dopants (TiO₂, ZnO, and nanodiamond) has been used for photoelectrochemical applications in our group [150-152]. Ram et al. have used RRPHTh-nanodiamond (ND) electrodes to provide high-sufficiency photoelectrochemical conversions superior to TiO₂-RRPHTh and ZnO-RRPHTh nanohybrid film [153]. The use of MoS₂- α -Fe₂O₃ as the n-electrode and RRPHTh-ND as the p-electrode in liquid-based photoelectrochemical cells has been studied in PEC cells. MoS₂- α -Fe₂O₃ as the counter electrode and RRPHTh-ND as the working electrode has been used to study photoelectrochemical cells. Cyclic voltammetry and chronoamperometry studies have been performed with visible light, radiation simulated for solar

radiation, as well as with 60 W lamps, to understand the photoelectrochemical properties of PEC cells.

5.2 Experimental Details

5.2.1 Materials

The materials iron chloride (FeCl_3), aluminum chloride (AlCl_3), sodium hydroxide (NaOH), MoS_2 , poly(3-Hexylthiophene), and ammonium hydroxide (NH_4OH) were purchased from Sigma-Aldrich. The fluorine tin oxide (FTO) coated glass, with resistance of $\sim 10 \Omega$, was also procured from Sigma-Aldrich. The centrifuged containers were purchased to clean the synthesized nanomaterials from the solution.

5.2.2 Synthesis of Nanomaterials

The $\alpha\text{-Fe}_2\text{O}_3$ and $\text{MoS}_2\text{-}\alpha\text{-Fe}_2\text{O}_3$ were synthesized using the sol-gel technique. Various concentrations of FeCl_3 with AlCl_3 were prepared in 500 ml round bottom flasks. Table 1 shows the amount of chemicals used for the synthesis of $\text{MoS}_2\text{-}\alpha\text{-Fe}_2\text{O}_3$. Later, NaOH was added to the resulting solution and stirred with a magnet. A condenser was connected to the round bottom flask containing the chemicals then placed in a heater to maintain $90\text{-}100 \text{ }^\circ\text{C}$ for the chemical reaction. The reaction was terminated after 24 hours, and the solution was cooled at room temperature. The synthesized material was separated using a centrifuge and continuous cleaning with water. The synthesized materials $\text{MoS}_2\text{-}\alpha\text{-Fe}_2\text{O}_3$ were initially left drying at room temperature. The $\text{MoS}_2\text{-}\alpha\text{-Fe}_2\text{O}_3$ was then dried at various temperatures (100, 200, 300, 400 and $500 \text{ }^\circ\text{C}$). In each case, the temperature was maintained in a furnace for one hour. The materials were then brought to room temperature and collected in a tight bottle for photoelectrochemical cells and various physical characterization studies.

5.2.3 Film Formation of Substrate

The $\text{MoS}_2\text{-}\alpha\text{-Fe}_2\text{O}_3$ was prepared at different concentrations by mixing it with acetic acid to obtain a homogenous solution to cast on various substrates. 500 mg of $\text{MoS}_2\text{-}\alpha\text{-Fe}_2\text{O}_3$ (0.1%, 0.2%, 0.5%, 1%, 2% and 5%) was ground into a powder and then mixed into 10 ml acetic acid in a small container and left for 10 hours. Later, the solutions were used to make films on quartz, silicon and fluorine tin oxide (FTO). The films were cured at different temperatures (300, 400 and 500 °C) for one hour. The films were then cooled to room temperature and used for XRD, SEM, cyclic voltammetry and UV-vis measurements.

5.2.4 RRPHTH-ND/NaOH/ $\text{MoS}_2\text{-}\alpha\text{-Fe}_2\text{O}_3$ -Based Photoelectrochemical Cells

The conducting polymer solution was made by dissolving 50 mg of RRPHTH in 50 ml of chloroform. Later, 50 mg of ND was added to the solution and kept suspended by stirring for 24 hours, similar to the work of Ram et al. [151]. The RRPHTH-ND film was fabricated using spin coating, as well as by casting the solution on silicon and ITO coated glass substrates. The photoelectrochemical cell was constructed using silicon, as well as ITO coated RRPHTH-ND as a working electrode and $\text{MoS}_2\text{-Fe}_2\text{O}_3$ as a counter electrode. The cyclic voltammetry (CV) as well as the chronoamperometry measurements were made using 0.1 M and 1M NaOH concentration. A schematic is drawn in Figure 1 to understand the effect of MoS_2 with $\alpha\text{-Fe}_2\text{O}_3$. Figure 1 shows the schematic of hydrogen production using the $\text{MoS}_2\text{-}\alpha\text{-Fe}_2\text{O}_3$ photocatalyst in 1 M NaOH based electrolyte in a PEC cell.

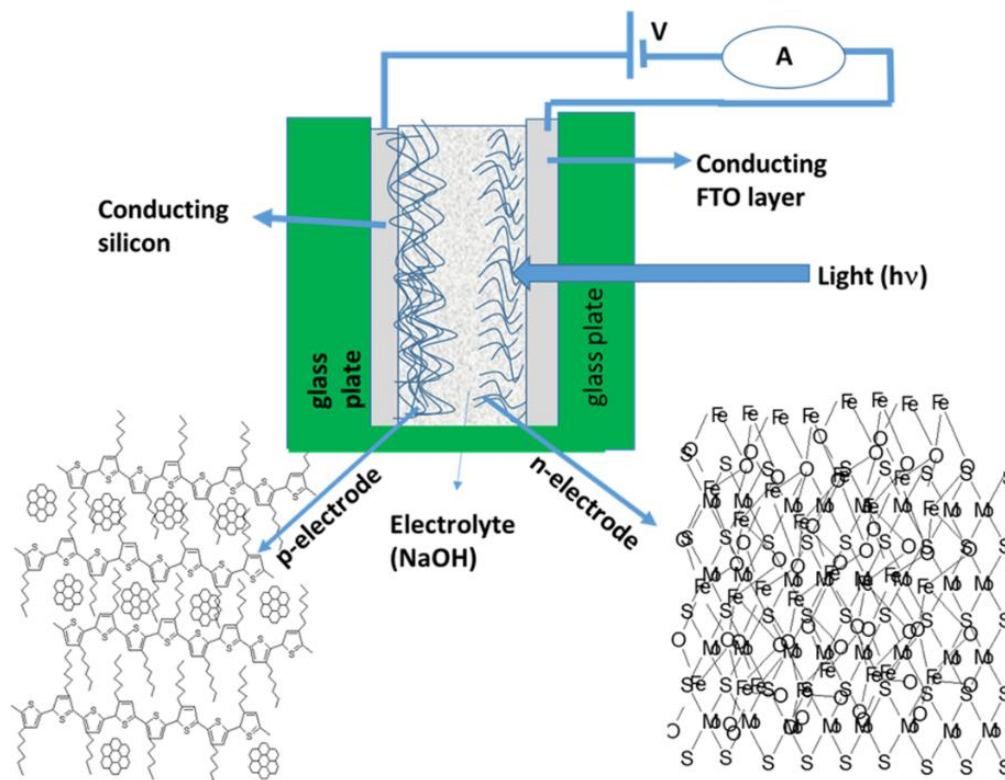


Figure 5.1 Schematic of hydrogen production using $\text{MoS}_2\text{-}\alpha\text{-Fe}_2\text{O}_3$ nanocomposite as n-type and RRPHTh-ND as p-type photocatalyst in 1 M NaOH

5.3 Physical Properties Studies

5.3.1 Scanning Electron Microscopy (SEM)

The structure and surface properties of $\alpha\text{-Fe}_2\text{O}_3$, $\text{MoS}_2\text{-}\alpha\text{-Fe}_2\text{O}_3$ and RRPHTh-ND films on silicon substrates were investigated through a Field Emission Hitachi S800 Scanning Electron Microscope (SEM) with an EDS attachment that worked at 25kV. Figure 2(a) shows the SEM image of $\alpha\text{-Fe}_2\text{O}_3$ nanomaterial consisting of well-dispersed spheres with particle sizes of 100-300 nm. The particle sizes increased in $\text{MoS}_2\text{-}\alpha\text{-Fe}_2\text{O}_3$ as shown in Figure 2(b). The films consisting of $\alpha\text{-Fe}_2\text{O}_3$ and $\text{MoS}_2\text{-}\alpha\text{-Fe}_2\text{O}_3$ have uniform and dense spheres of particles. The ND hybrid with RRPHTh conducting polymer has particle sizes varying from 100 nm to 500 nm. The average size of nanoparticles of ND was kept at approximately 20 nm. The RRPHTh provides a nearly uniform covering over the ND particles forming the nano-hybrid structure.

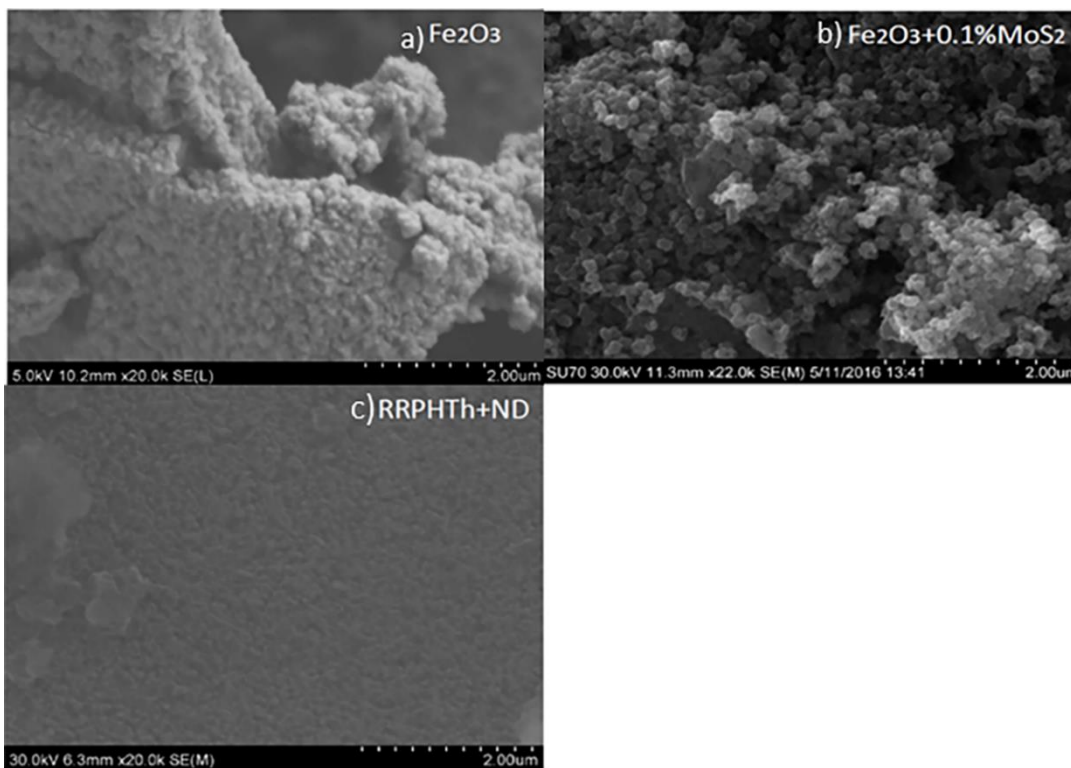


Figure 5.2 Scanning electron micrographs (SEM) of (a) α -Fe₂O₃, (b) α -Fe₂O₃+0.1%MoS₂, and (c) RRPHTH-ND.

5.3.2 Fourier Transform Infrared Spectroscopy (FTIR)

The infrared bands at 467 and 523 cm⁻¹ are related to Fe-O stretching and bending vibration mode for α -Fe₂O₃ nanomaterial as shown in Figure 3(a). Figure 3(b) shows the FTIR spectra of α -Fe₂O₃ + 0.1% MoS₂. It shows IR bands at 1388 and 1407 cm⁻¹ which are related to the stretching vibration as well as in-plane bending vibration of O-H of α -Fe₂O₃ nanomaterial [154]. Moreover, the IR bands at 544 and 1630 cm⁻¹ are assigned to the OH⁻ group which is in-plane bending vibration and γ_{as} Mo-S vibration due to the presence of MoS₂ [154]. However, the bands at 638, 802, and 892 are generated because of out-of-plane bending vibration and γ_{as} Mo-O vibrations, which are related to the OH⁻ group. In addition, Fe-O presence shows stretching vibration in α -Fe₂O₃ + 0.1% MoS₂ [154]. Figure 3(c) shows FTIR spectra of RRPHTH-ND; various bands are also presented in Table 1. The bands at 1739 cm⁻¹ are the characteristic bands of nanodiamond,

while the presence of 1687, 1129 and 630 cm^{-1} are due to the presence of a functional group in the nanodiamond [151]. The RRPHTH characteristic peaks (413, 475, 514, 758, 800, 852, 1000, 1058, 1092, 1260, 1300, 1390, 1446, 1497, 1635, 1687, and 1820) are shown in Figure 3(c), which can be well compared with the work of Ram et al. [151].

Table 5.1: Infrared bands of each $\alpha\text{-Fe}_2\text{O}_3$, 0.1% MoS_2 , and RRPHTh-ND.

Material	Infrared bands in cm^{-1}
$\alpha\text{-Fe}_2\text{O}_3$	467, 523, 578, 796, 830, 872, 990, 1046, 1076, 1376, 1551, 1625, 1736, 1763
0.1% MoS_2	512, 522, 654, 802, 1114, 1396, 1434, 1666, 2836, 2952, 3448
RRPHTh-ND	413, 475, 514, 630, 758, 800, 852, 1000, 1058, 1092, 1129, 1260, 1300, 1390, 1446, 1497, 1635, 1687, 1739, 1820, 2089, 3415,

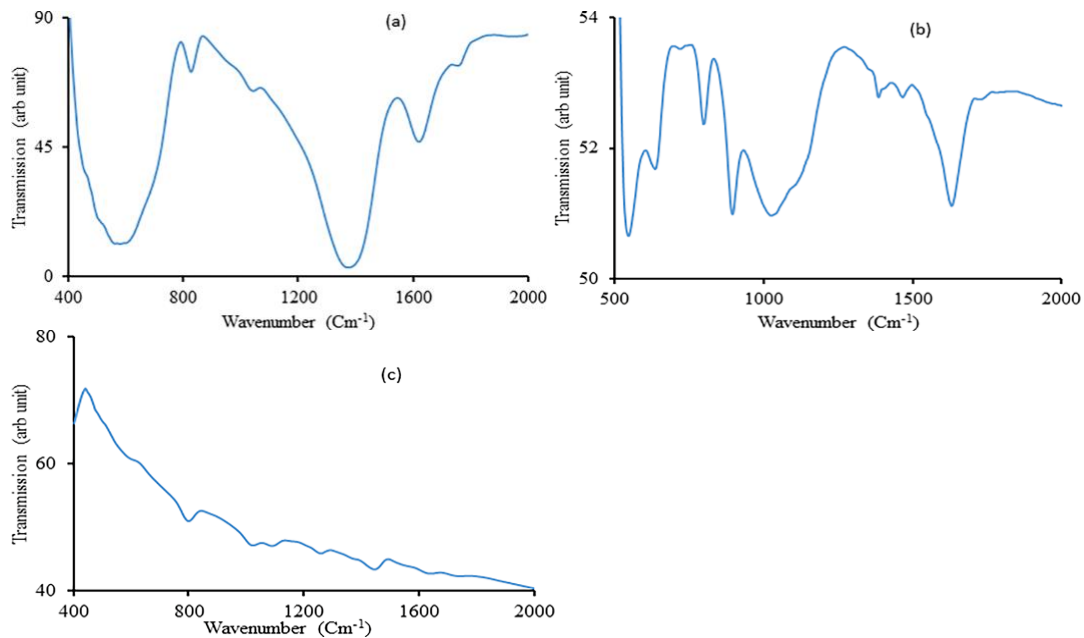


Figure 5.3 FTIR spectra of (a) $\alpha\text{-Fe}_2\text{O}_3$, (b) $\alpha\text{-Fe}_2\text{O}_3+0.1\%\text{MoS}_2$, and (c) RRPHTh-ND.

5.3.3 X-Ray Diffraction (XRD)

The model PAN-alytical X'Pert Pro MRD system, operated at 40 kV and 40 mA, was used to measure X-ray diffraction having $\text{CuK}\alpha$ radiation of wavelength = 1.5442 Å. Figure 4(a) shows

an XRD image of α -Fe₂O₃ nanomaterial. The α -Fe₂O₃ nanomaterial reveals a polycrystalline structure and coincides with the values as earlier investigated by Hussein et al. [155]. Table 2 shows the summary of diffraction angle 2theta angles [155]. Figure 4(b) shows the sharp diffraction angle of XRD spectra of α -Fe₂O₃ + 0.1% MoS₂. The sharp diffraction angle peaks at 31.69 (012), 36.62 (110), 45.46 (024), 53.23 (116), 58.93 (214) result from the crystallinity of Fe₂O₃ as well as the presence of doping of MoS₂ in α -Fe₂O₃ + 0.1% MoS₂ nanomaterial [26]. However, the band at 53.23 is related to MoS₂ in MoS₂- α -Fe₂O₃ nanomaterial.

Table 5.2: X-ray diffraction peaks of each α -Fe₂O₃, α -Fe₂O₃+0.1%MoS₂

α -Fe ₂ O ₃	30.41, 32.11, 33.87, 39.83, 44.68, 45.54, 47.76, 63.89, 66.16, 72.96, 76
α -Fe ₂ O ₃ +0.1%MoS ₂	31.69, 36.62, 45.46, 53.23,58.93

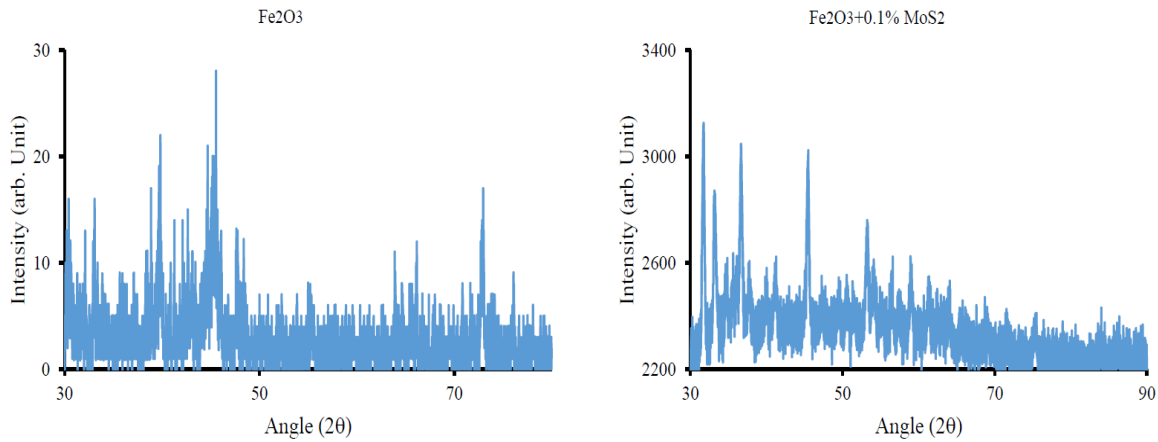


Figure 5.4 X-ray diffraction pattern of (a) α -Fe₂O₃, and (b) α -Fe₂O₃+0.1%MoS₂.

5.3.4 UV-Visible Spectroscopy (UV-Vis)

An UV-Vis spectrometer Jasco V-530 was utilized to determine the absorption peaks of various nanomaterials such as α -Fe₂O₃, α -Fe₂O₃+0.1% MoS₂, and RRPHT_h-ND. Figure 5(a) shows the UV-vis absorption spectra of α -Fe₂O₃ film on ITO coated glass plates. The absorption

band at 550 nm was depicted as similar to the previous study by Hussein et al [140]. The characteristic absorption bands at 373, 382, 406, 442, 475, 612 nm of α -Fe₂O₃-0.1% MoS₂ were observed in Figure 4(b). Figure 4(c) reveals the characteristics bands at 412, 475, 503,588, 695, 834 nm for ND-RRPHTH based film similar to the previous work by Ram et al. [155]. The band gap of MoS₂ varies from 1.8 to 1.9 eV, whereas the bandgap of α -Fe₂O₃ is 2.1 eV. So, we have estimated the bandgap of MoS₂- α -Fe₂O₃ in the range of 1.94 to 2.4 eV, which fits well in the region of visible light. MoS₂ doping increases the conductivity of the samples. The schematic in Figure 10 shows photogenerated electrons from the conduction band (CB) of MoS₂ that is transferred to CB of hematite, whereas holes from hematite are transferred to valance band (VB) of MoS₂. This doping enhances the photocatalytic activity of the MoS₂ composite with α -Fe₂O₃.

Table 5.3: UV–vis absorption peaks of each α -Fe₂O₃, α -Fe₂O₃+0.1%MoS₂, and RRPHTH-ND

Fe ₂ O ₃	286, 346, 371, 470,580
0.1%MoS ₂	373, 382, 406, 442, 475, 612
RRPHTH-ND	412, 475, 503,588, 695, 834

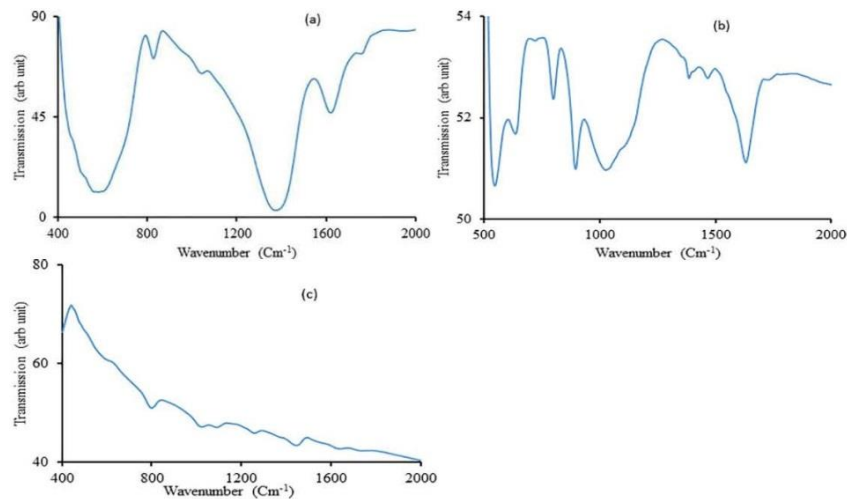


Figure 5.5 UV-vis absorption spectra of (a) α -Fe₂O₃, (b) α -Fe₂O₃+0.1%MoS₂, and (c) RRPHTH-ND.

5.4 Electrochemical Studies

5.4.1 Schematic of P-N Configuration-Based Reaction Process

The $\text{MoS}_2\text{-}\alpha\text{-Fe}_2\text{O}_3$ as the n-electrode and RRPHTH-ND as the p-electrode in a liquid electrolyte (1M NaOH, HCl etc.) was studied in photoelectrochemical cells. The cyclic voltammetry (CV) and the chronoamperometry were analyzed extensively on the p-n configuration-based photoelectrochemical cell with and without light. Figure 6 shows the water splitting application in RRPHTH-ND as the p-type and $\text{MoS}_2\text{-Fe}_2\text{O}_3$ as the n-type in 1M NaOH water-based electrolyte photoelectrochemical cell under a photoexcitation and applied electrical potential. The NaOH was used as an electrolyte in the photoelectrochemical cell. The cyclic voltammetry as well as the chronoamperometry measurements were made using 0.1 M and 1M concentrations of NaOH-based electrolytes.

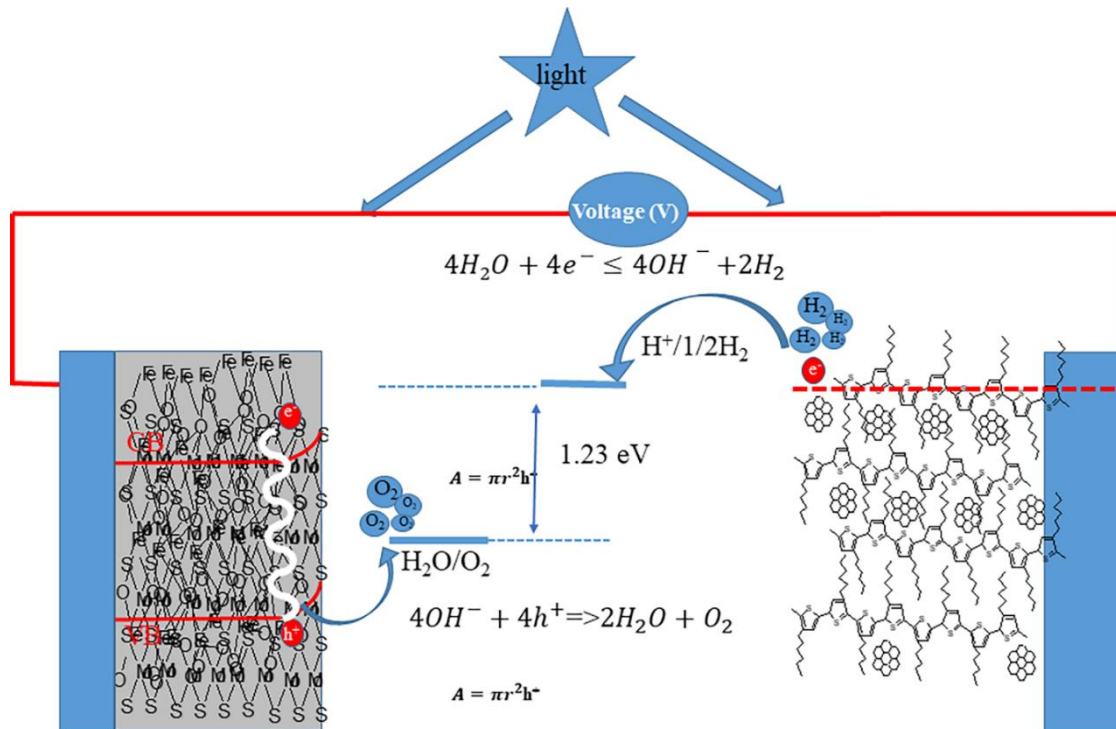


Figure 5.6 Schematic of water-splitting application in p-type RRPHTH-ND and n-type $\text{MoS}_2\text{-Fe}_2\text{O}_3$ in water-based electrolyte photoelectrochemical cell under photoexcitation and under potential

Attempts were made to understand the water splitting using the work function and band gap of the material. The MoS₂ doped α -Fe₂O₃ in water has a band gap varying from 2.17 to 1.94 eV. The hydrogen gas was formed at the electrode of RRPHTH-ND whereas oxygen was liberated at the MoS₂- α -Fe₂O₃ based electrode.

5.4.2 Cyclic Voltammetry

Figure 7 shows the cyclic voltammetry curves with and without light for MoS₂- α -Fe₂O₃ and RRPHTH-ND based electrodes in 0.1M NaOH solution. The CV curves show nearly twice the value of photocurrent than without light. However, at light under 2V, exposition of the photocurrent is shown, which is a 30 times greater varying current for n type-based electrode containing 1% MoS₂ - α -Fe₂O₃ in p-type RRPHTH-ND containing 1M NaOH electrolyte.

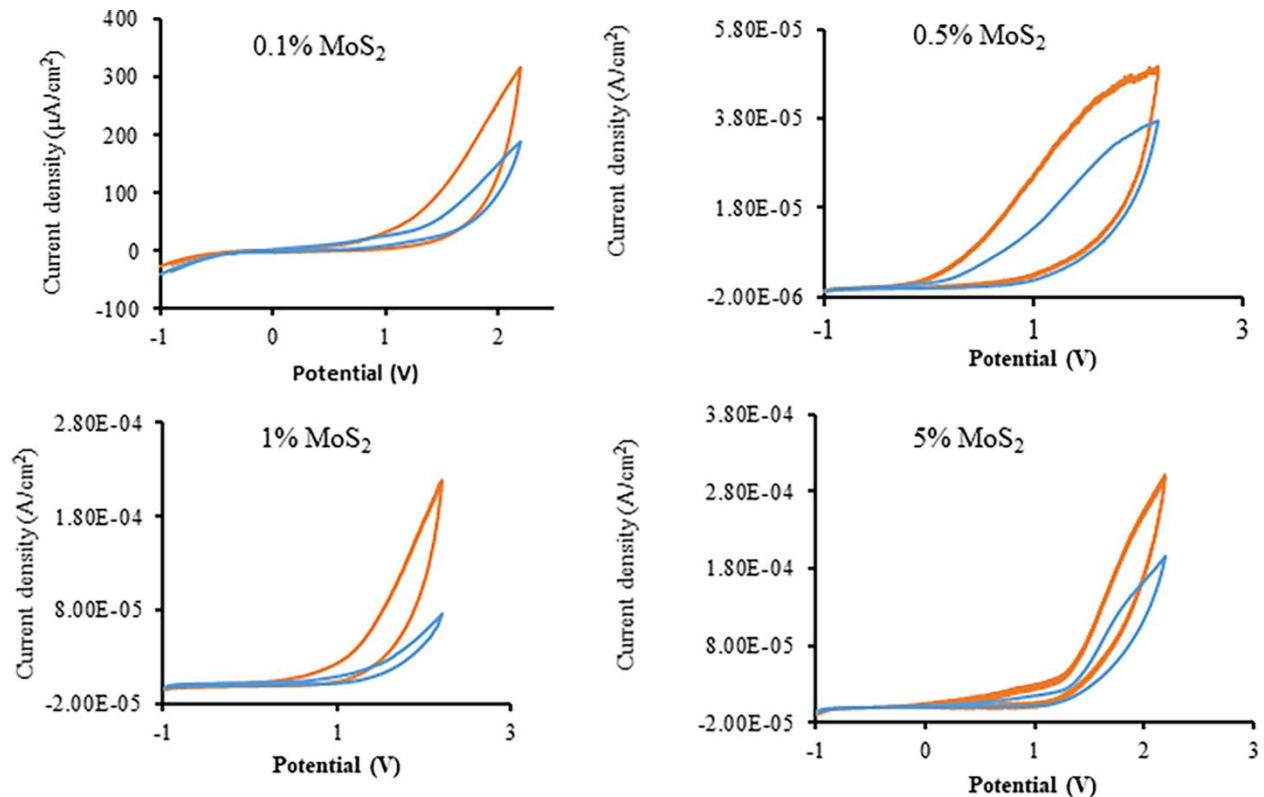


Figure 5.7 Cyclic voltammetry study of p-type RRPHTH-ND and n-type MoS₂-Fe₂O₃ in NaOH 1M-based electrolyte in photoelectrochemical cell with and without light

5.4.3 Chronoamperometry

Figure 8 below shows the chronoamperometry curves of MoS₂- α -Fe₂O₃ and RRPHTH-ND in 0.1 M NaOH solution. A light bulb of 60 W was exposed and the immediate current in the device increased significantly for 0.1% MoS₂- α -Fe₂O₃ as the n-type and RRPHTH-ND as the p-type electrodes in a cell containing 0.1M NaOH electrolytes. The photocurrent is observed with the cell's exposure to light. However, the transient current is immediately observed due to the combination of electron and hole-pair, and the photocurrent decreases 0.1% in the MoS₂- α -Fe₂O₃ as the n-type and RRPHTH-ND as the p-type electrode-based electrodes in photoelectrochemical cells.

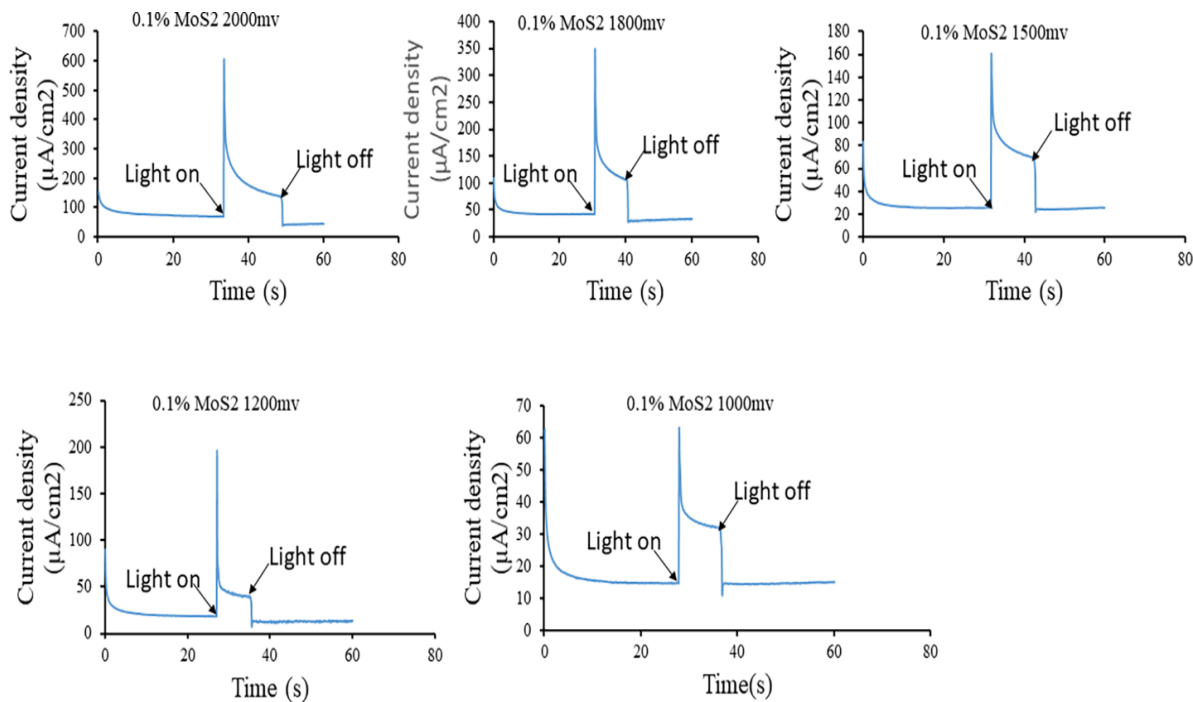


Figure 5.8 Current-transient study of p-type RRPHTH-ND and n-type 0.1% MoS₂- α -Fe₂O₃-based electrodes in 1M NaOH-based electrolyte in photoelectrochemical cell with and without light

Figure 9 shows chronoamperometry results of 0.1, 0.2, 1, and 5% of MoS₂ in α -Fe₂O₃ MoS₂ as n-type electrode and RRPHTH-ND as p-type electrode in a cell containing 0.1M NaOH

electrolyte. The current density was found to be highest for 1% MoS₂-α-Fe₂O₃ as n-type electrode with RRPHT_h-ND as p-type electrode in a cell containing 0.1M NaOH electrolyte. There is a current transient, but it becomes a stable photocurrent after 2-3 seconds, whereas there is continual decrease of photocurrent in 0.1 and 0.2 % of MoS₂ in α-Fe₂O₃ nanocomposite material. However, 5% of MoS₂ in α-Fe₂O₃ nanocomposite material does not reveal a higher photocurrent due to aggregation of MoS₂ in α-Fe₂O₃ nanomaterial.

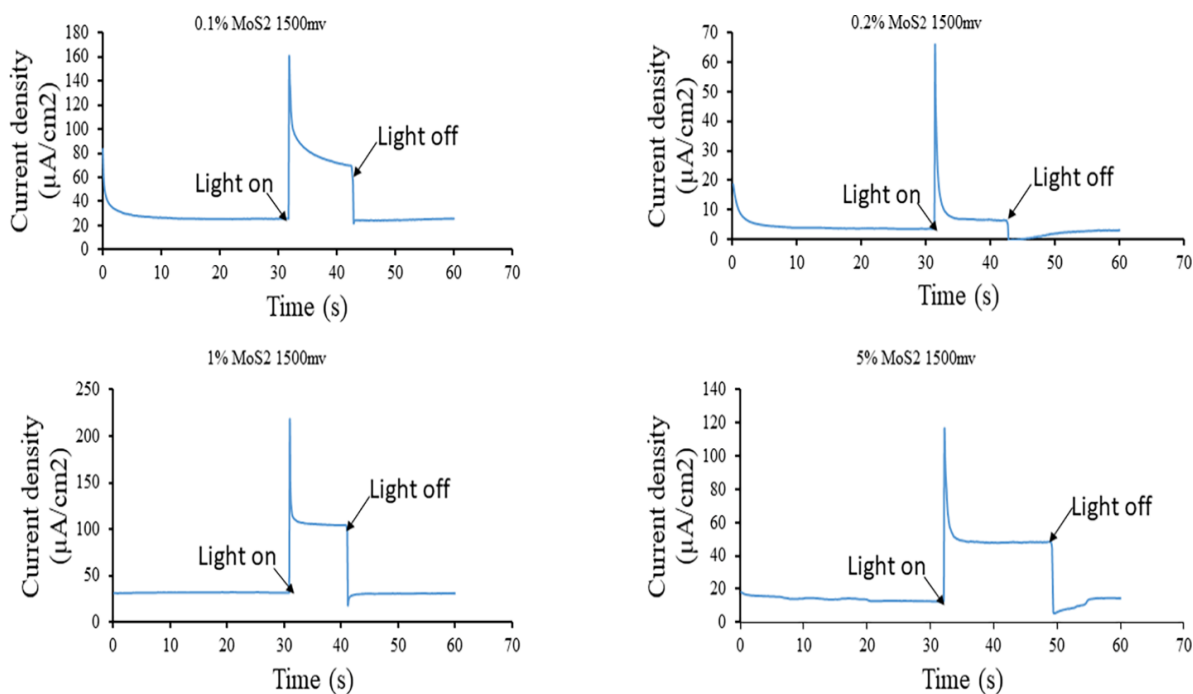


Figure 5.9 Current-transient study of photoelectrochemical cell containing RRPHT_h-ND as p-type electrode and 0.1, 0.2, 1, and 5% of MoS₂ in MoS₂-α-Fe₂O₃ as n-type electrode in 1M NaOH-based electrolyte with light switch on and off at applied potential of 1500 mV

Figure 10 shows chronoamperometry results of 0.1, 0.2, 1, and 5% of MoS₂ in α-Fe₂O₃ MoS₂ as n-type electrode and RRPHT_h-ND as p-type electrode in a cell containing 0.1M NaOH electrolyte at a potential of 2000 mV. The current density has been found to be highest for 0.1 and 1% MoS₂-α-Fe₂O₃ based n-type based electrode. There is a larger current transient for 0.1% MoS₂ in MoS₂-α-Fe₂O₃ nanocomposite material. However, stable photocurrent after 2-3 seconds is also

observed for 1% of MoS₂ in MoS₂- α -Fe₂O₃ nanocomposite nanomaterial film. The chronoamperometry results reveal that 1% MoS₂ in MoS₂- α -Fe₂O₃ nanocomposite is a suitable structure to obtain higher photocurrent density.

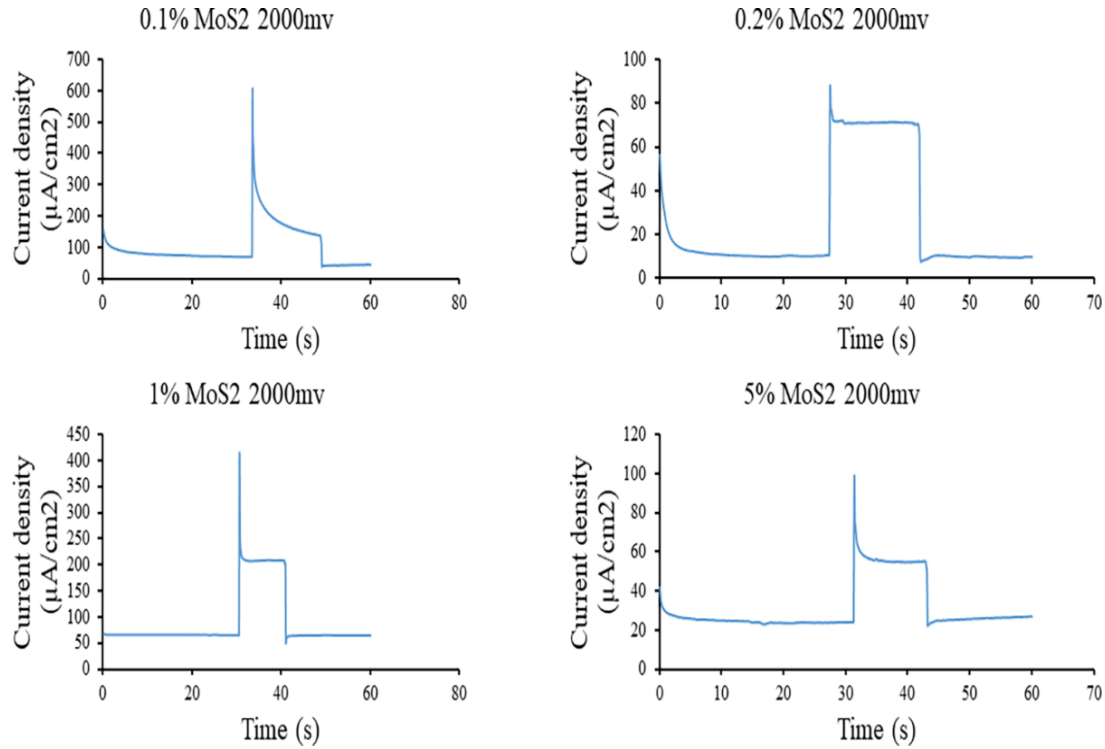


Figure 5.10 Current-transient study of photoelectrochemical cell containing RRPHT_h-ND as p-type electrode and 0.1, 0.2, 1, and 5% of MoS₂ in MoS₂- α -Fe₂O₃ as n-type electrode in 1M NaOH- based electrolyte

5.5 Conclusion

From this chapter, it is clear that the water-splitting process is renewable and clean in generating hydrogen. To measure the photoelectrochemical properties of this process, the MoS₂ - α -Fe₂O₃ electrodes were synthesized. The films, consisting of α -Fe₂O₃ as well as MoS₂- α -Fe₂O₃, have a uniform and dense sphere of particles. The 1% MoS₂- α -Fe₂O₃ film showed the most stable photocurrent. From the XRD figure, the band at 53.23 is related to MoS₂ in MoS₂- α -Fe₂O₃ nanomaterial. The photoelectrochemical photocurrent was found to be dependent on the applied potential from 0 to 2V in an electrolyte of varying molar concentration of NaOH. The

chronoamperometry results showed that 1% MoS₂ in MoS₂- α -Fe₂O₃ nanocomposite can be a suitable structure for obtaining a higher photocurrent density. The p-n configuration is a stable photoelectrochemical cell and allows for eliminating the photo corrosion process. Also, this p-n configuration prevents the leakage of solvent and has low absorption of light due to the thin layer of electrolytes. It is a renewable and affordable process to produce clean energy in the form of hydrogen. PEC with 1% MoS₂- α -Fe₂O₃ nanocomposite has the potential to revolutionize full-cell technology.

CHAPTER 6: P-N BASED PHOTOELECTROCHEMICAL DEVICE FOR WATER-SPLITTING APPLICATION OF ALPHA-HEMATITE (α -Fe₂O₃)-TITANIUM DIOXIDE (TiO₂) AS N-ELECTRODE & POLYHEXYLTHIOPHENE (RRPHTH) - NANODIAMOND (ND) AS P-ELECTRODE⁴

6.1 Introduction

Great attention has been paid to the production of hydrogen as an alternative energy by the photoelectrochemical (PEC) water-splitting process [156, 157]. The transition metal oxide semiconductors have been used as a photocatalyst for water PEC-based splitting applications [91, 158-160]. Among materials, α -Fe₂O₃ is one of the more extensively explored materials and has advantages for production of hydrogen in the PEC process including chemical suitability for electrolytes (PH > 3), relatively narrow bandgap (2.0 - 2.2eV), abundance, and inexpensive cost [161-163]. Due to the short electron-hole pair time (<10 ps) and hole diffusion length (2-4 nm), which cause a high recombination rate of photo-generated carriers in the bulk. Hematite-based water splitting has lower efficiency than that of the theoretical (12.6 mA/cm²) and has restricted PEC applications [68, 164]. In addition, the oxidation reduction seems to delay on the surface of hematite-based water splitting due to the kinetics of the interfacial extraction of the hole, and might be accompanied by an increased charge recombination and the decline of efficiency [164, 165].

⁴ This chapter has been published "Hussein Alrobei, H.Y.L., Ashok Kumar, and Manoj K. Ram, p-n Based Photoelectrochemical Device for Water Splitting Application Alpha-Hematite (α -Fe₂O₃)-Titanium Dioxide (TiO₂) as N-Electrode & Polyhexylthiophene (RRPHTh) – Nanodiamond (ND) as P-Electrode. MRS Advances, 2017." and copyright permission in appendix A.3

To improve photoelectrochemical properties, TiO₂ has been investigated because of the low cost for the fabrication of photoelectrochemical stability [166, 167]. However, TiO₂ also has significant limitations. Firstly, excitation is generated in response to UV regions. Secondly, the PEC device, has been fabricated with TiO₂, which often has a short diffusion length of excitation [161, 168, 169]. To solve the above limitations, some suggestions are made for reducing band gap that allow the PEC device to absorb the visible region and create a large contact area with the electrolyte, allowing the PEC device to split electron-hole pairs [161, 168, 170]. In gathering advantages of both metal oxide materials, TiO₂ with Fe₂O₃ film was shown to increase contact area with electrolytes, reducing e-h recombination and shifting light absorption along with visible region [164, 171, 172].

However, the properties of alpha-hematite photoanode were changed when doped with various concentrations of TiO₂. Under this work, the sol-gel technique was used to synthesis α -Fe₂O₃-TiO₂ nanomaterials with different concentrations (50%, 25%, 16%, 5% and 2.5% of TiO₂) and were dried at 300 °C and 500°C, respectively. The physical properties of α -Fe₂O₃-TiO₂ nanomaterials were investigated by using SEM, XRD, UV-Vis, FTIR and Raman measurements. The photoelectrochemical properties were also examined by using the chronoamperometry technique.

6.2 Experimental Details

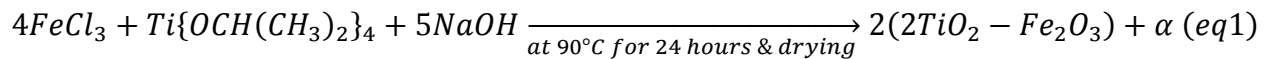
6.2.1 Materials

Iron chloride (FeCl₃), titanium (IV)-isopropoxide solution (TTIP), and sodium hydroxide (NaOH) were used to synthesize the α -Fe₂O₃-TiO₂ nanomaterials. Potassium bromide (KBr, Aldrich), which was purchased from the Sigma-Aldrich company, was used for making FTIR sample pellets. The synthesized materials were mixed with acrylic acid to fabricate the film. To

measure electrochemical properties, α -Fe₂O₃-TiO₂ materials were coated on indium tin oxide (ITO) glass, which operated as working electrode. Polyhexylthiophene (RRPHT_h)-nanodiamond (ND) materials were coated on silicon wafers which worked as a counter electrode.

6.2.2 Synthesis of Nanomaterial

The α -Fe₂O₃-TiO₂ nanomaterials were synthesized by sol-gel. Equation 1 shows the chemical reaction equation. The synthesized α -Fe₂O₃-TiO₂ nanomaterials were obtained by changing various concentrations of reactant materials, which were FeCl₃ and TTIP. To obtain different concentrations of TiO₂ (50%, 25%, 16%, 5% and 2.5%), the amount of FeCl₃ and TTIP were put into the round bottom flask with DI water (450 ml), respectively. To dissolve the above materials, the resulting solution was stirred with a magnetic stir bar, and the flask was put on the hotplate at 60 °C for one hour. Afterwards, the NaOH solution (50mL) was added to the resulting solution and connected to a reflux condenser. Reaction temperature was maintained at 90 °C for the chemical reaction, and reaction time was maintained for 24 hours. Filter paper was utilized to separate the solution and to extract α -Fe₂O₃-TiO₂ nanomaterial from residues. The α -Fe₂O₃-TiO₂ nanomaterial was washed using DI water twice to remove the impurities. The α -Fe₂O₃-TiO₂ nanomaterial was dried at 300 °C and 500 °C for two hours each. Then, dried α -Fe₂O₃-TiO₂ nanomaterial was further grounded using a ball-milling machine. TiO₂ nanomaterial was fabricated with 0.05M of TTIP, and subsequently dried at 500 °C for three hours using similar conditions of the α -Fe₂O₃-TiO₂ nanomaterial synthesis process.



6.2.3 Film Formation of Substrate

The α -Fe₂O₃-TiO₂ nanomaterial and KBr powder were mixed and applied via hydraulic press for obtaining the pellets. The α -Fe₂O₃ and TiO₂ pellets were prepared for comparative

analysis. To fabricate film-type specimens, the α -Fe₂O₃-TiO₂ nanomaterial was mixed with a small amount of acetic acid for obtaining the colloidal materials. The colloidal α -Fe₂O₃-TiO₂ materials were used to coat ITO glasses (2cm ×2.5cm) and were cured at 100 °C for one hour. The counter electrode was fabricated by immersing pieces of Si-wafer in RRPHTH-ND colloidal solution [112].

6.3 Physical Properties Studies

The X-ray diffraction (XRD), SEM, and Raman spectroscopy were performed using powder from the samples. For electrochemical properties, a Potentiostat/Galvanostat instrument (Radiometer Analytical, Volta lab 40 PGZ301) was utilized. To measure cyclic voltammetry and chronoamperometry properties, the working electrode (α -Fe₂O₃-TiO₂/ITO) and the counter electrode (RRPHTH-ND/Si) were immersed in NaOH (0.1M) solution as electrolytes and connected to the equipment using clips.

6.3.1 UV-Visible Spectroscopy (UV-Vis)

The UV-Vis characterizations of α -Fe₂O₃-TiO₂ nanomaterial film on glass substrates were measured using a UV-visible spectrophotometer (Jasco- V-670 absorption spectrometer). Figure 1 and Figure 2 show UV-Vis spectra of TiO₂, α -Fe₂O₃ and α -Fe₂O₃-TiO₂ that were prepared at various concentrations of TiO₂ to α -Fe₂O₃ and dried at 300 °C and 500°C, respectively. The absorption spectra were obtained from the UV-Vis spectroscopy by measuring the sample holder that contained the powdered sample dissolved in DI water. Table 1 and 2 list the absorption peaks of all samples. For comparison, the α -Fe₂O₃ nanomaterial exhibits absorption of approximately 300 nm in the UV region and broad weak absorption at 400-600 nm in the visible region. For the TiO₂ nanomaterials, two absorption bands in the UV regions at 237 nm and 327nm are observed. In addition, there are also few very weak absorption bands at 428 nm and 488nm in the visible region (Figure 1 and 2). Figure 1 (b-f) shows the UV-Vis absorption bands for five different

concentrations of TiO₂ (2.5%, 5%, 16%, 25% and 50%) to α -Fe₂O₃ nanomaterials that were dried at 300 °C. Figure 2(b-f) shows the absorption band for α -Fe₂O₃-TiO₂ nanomaterials dried at 500 °C with the same conditions. From Figure 1 and Figure 2, drying temperature appears to have insignificant influence on absorption bands of the material. For high concentrations of TiO₂ (16, 25, and 50%) samples, the absorption bands are similar to that of the TiO₂ sample. Thus, absorption bands exhibit the characteristics of TiO₂ nanomaterial. For the low concentrations of TiO₂ (5 and 2.5%) samples, the absorption bands appear for the α -Fe₂O₃-TiO₂ nanomaterials, which are different spectra than the Fe₂O₃ and TiO₂ samples. The absorption bands at 238, 270, and 320 nm begin to appear in the UV region. In addition, strong absorptions appear near 428 and 540 nm in the visible region. Thus, α -Fe₂O₃-TiO₂ nanomaterial with a small quantity of TiO₂ seems to be red-shifted due to the TiO₂ nanomaterials showing improvement in absorption in the range of 400-600 nm [173, 174].

Table 6.1: Peaks of each α -Fe₂O₃-TiO₂ nanomaterial dried at 300°C

	Wavelength (cm ⁻¹)
TiO ₂	237, 327, 428, 488
α -Fe ₂ O ₃ -(50%)TiO ₂	236, 397, 438, 524, 607
α -Fe ₂ O ₃ -(25%)TiO ₂	238, 321, 386, 532
α -Fe ₂ O ₃ -(16%)TiO ₂	236, 453, 561
α -Fe ₂ O ₃ -(5%)TiO ₂	279, 325, 428, 534
α -Fe ₂ O ₃ -(2.5%)TiO ₂	216, 236, 264, 329, 432, 537
α -Fe ₂ O ₃	299, 364, 488, 537

Table 6.2: Peaks of each α -Fe₂O₃-TiO₂ nanomaterial dried at 500°C

	Wavelength (cm ⁻¹)
TiO ₂	237, 327, 428, 488
α -Fe ₂ O ₃ -(50%)TiO ₂	235, 334, 338, 526
α -Fe ₂ O ₃ -(25%)TiO ₂	236, 404, 432, 522
α -Fe ₂ O ₃ -(16%)TiO ₂	236, 335, 456,560
α -Fe ₂ O ₃ -(5%)TiO ₂	230, 271, 329,426, 544
α -Fe ₂ O ₃ -(2.5%)TiO ₂	218, 239, 268, 322, 428, 544
α -Fe ₂ O ₃	299, 364, 488, 537

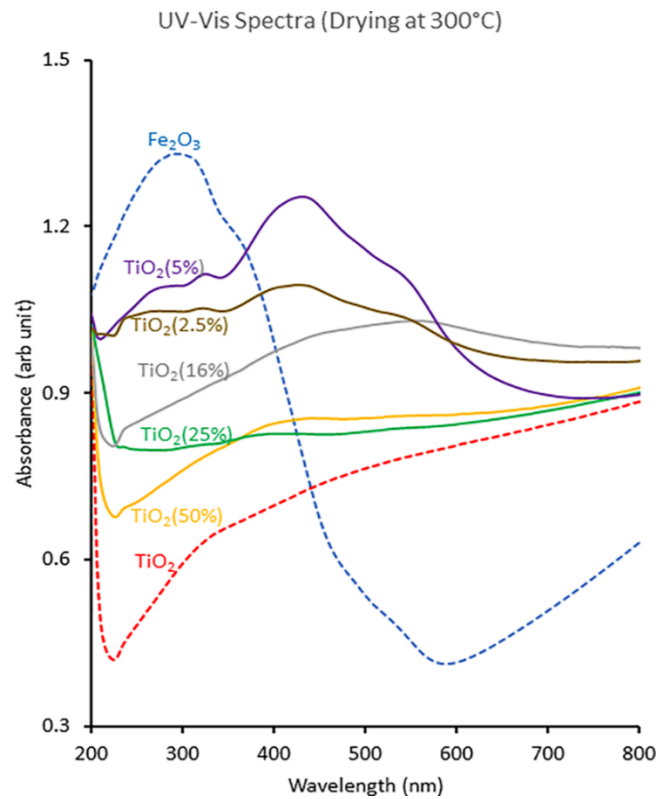


Figure 6.1 UV-vis absorption spectra of α -Fe₂O₃-TiO₂ nanomaterials dried at 300°C

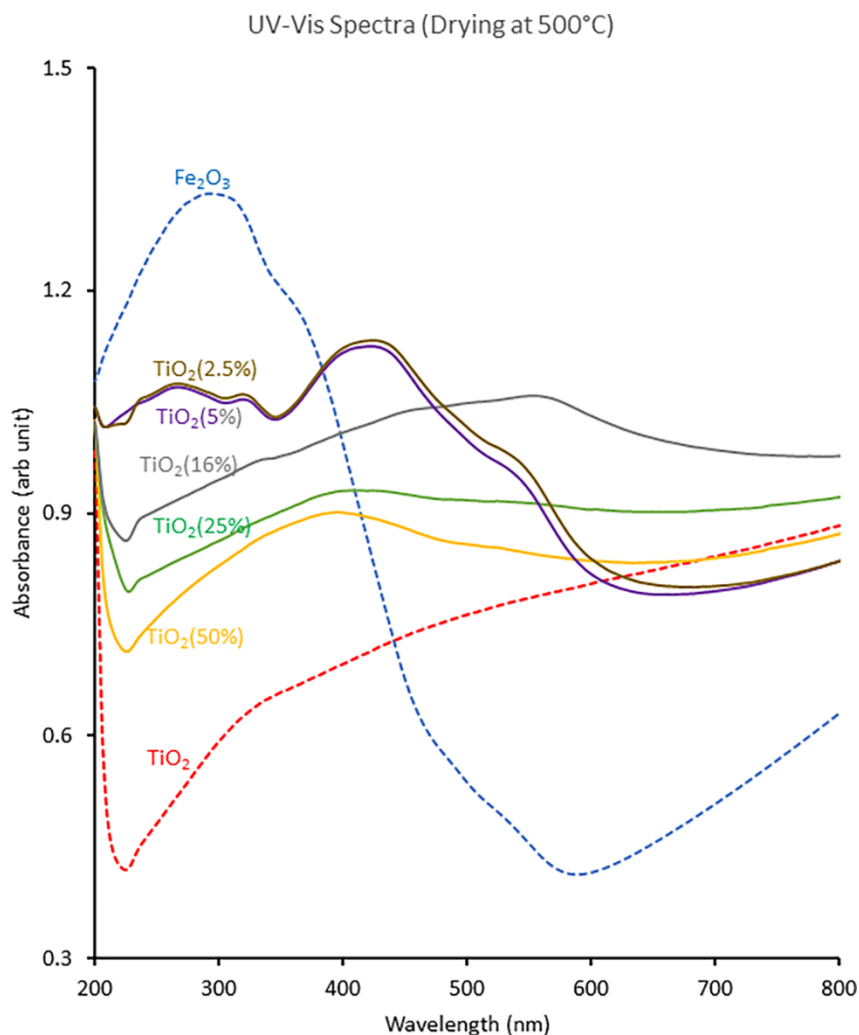


Figure 6.2 UV-vis absorption spectra of α -Fe₂O₃-TiO₂ nanomaterials dried at 500°C

6.3.2 Fourier Transform Infrared Spectroscopy (FTIR)

The FTIR measurement of nanomaterials was made using KBr pellets in transmission mode using the FTIR spectrophotometer (Perkin-Elmer spectrum one). The data was obtained after averaging 16 scans for each sample recorded from 400 to 2000 cm⁻¹. Figure 3 shows the α -Fe₂O₃, TiO₂, and α -Fe₂O₃-TiO₂ nanomaterials with various concentrations of TiO₂ (50, 25, 16, 5 and 2.5%) at 500 °C of drying. The samples were measured using transmission mode from 400 to 2000 cm⁻¹. The infrared bands of all samples are shown in Table 3. The weak band near 1630 cm⁻¹ is relevant to the H-O-H bending vibration mode, since moisture on the surface of the sample is

adsorbed [175]. The TiO₂ samples show broad bands in range of 400 to 700 cm⁻¹, which are ascribed to the stretching vibration of Ti-O-Ti and Ti-O bridge bond [175, 176]. On the other hand, the α-Fe₂O₃ sample exhibits the broad band at 580 cm⁻¹, which is ascribed to the Fe-O(metal-oxygen) stretching-mode [177]. For the α-Fe₂O₃-TiO₂ nanomaterial, infrared bands at 460 and 560 cm⁻¹ become stronger as the concentration of TiO₂ is lowered. Both infrared bands at 460 and 560 cm⁻¹ appear to correspond to the α-Fe₂O₃-TiO₂ nanomaterial lattice.

Table 6.3: Infrared bands of each α-Fe₂O₃-TiO₂

	Wavelength (cm ⁻¹)
TiO ₂	583, 651, 713, 767, 898, 1452, 1624, 1751
α-Fe ₂ O ₃ -(50%)TiO ₂	442, 483, 588, 720, 950, 1354, 1451, 1541, 1620
α-Fe ₂ O ₃ -(25%)TiO ₂	473, 582, 859, 942, 1070, 1346, 1452, 1542, 1617
α-Fe ₂ O ₃ -(16%)TiO ₂	469, 554, 856, 932, 1066, 1346, 1449, 1622, 1726
α-Fe ₂ O ₃ -(5%)TiO ₂	454, 540, 932, 1064, 1184, 1341, 1521, 1615
α-Fe ₂ O ₃ -(2.5%)TiO ₂	456, 542, 928, 1064, 1170, 1346, 1527, 1629
α-Fe ₂ O ₃	454, 501, 561, 582, 825, 1041, 1373, 1621, 1757

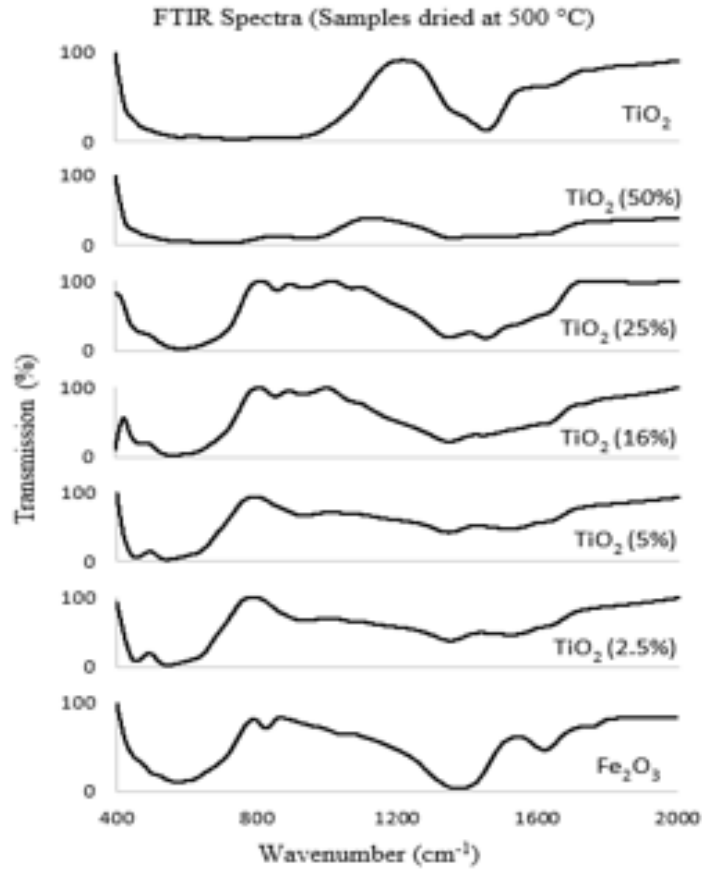


Figure 6.3 FTIR spectra of α -Fe₂O₃-TiO₂ nanomaterials

6.3.3 Raman Spectroscopy

Figure 4 shows the Raman spectra of the Fe₂O₃, TiO₂, and α -Fe₂O₃-TiO₂ nanomaterials with different concentrations of TiO₂ (50, 5, and 2.5%) with heat treatment at 500 °C. Table 4 indicates the Raman peak of all samples. The α -Fe₂O₃ sample exhibits peaks of 225, 295, 409 cm⁻¹, which are assigned to hematite. Namely, the lines at 225 cm⁻¹ are assigned to the A_{1g} vibration mode and 296 and 409 cm⁻¹ are assigned to the E_g vibration mode [178, 179]. The TiO₂ samples show 205, 275, 434, 633 and 823 cm⁻¹. The TiO₂ sample includes both anatase and rutile phases: Raman shifts near 205 and 633 cm⁻¹ for anatase phase, and nearby 434 and 823 cm⁻¹ for rutile [180-182].

Table 6.4: Peaks of each α -Fe₂O₃-TiO₂

	Wavelength (cm ⁻¹)
TiO ₂	205, 275, 434, 633, 823
α -Fe ₂ O ₃ -(50%)TiO ₂	215, 278, 375, 717, 978
α -Fe ₂ O ₃ -(5%)TiO ₂	232, 288, 406, 628, 664, 819, 975
α -Fe ₂ O ₃ -(2.5%)TiO ₂	225, 243, 299, 406, 614, 664, 819, 975
α -Fe ₂ O ₃	225, 295, 409, 712, 824, 970

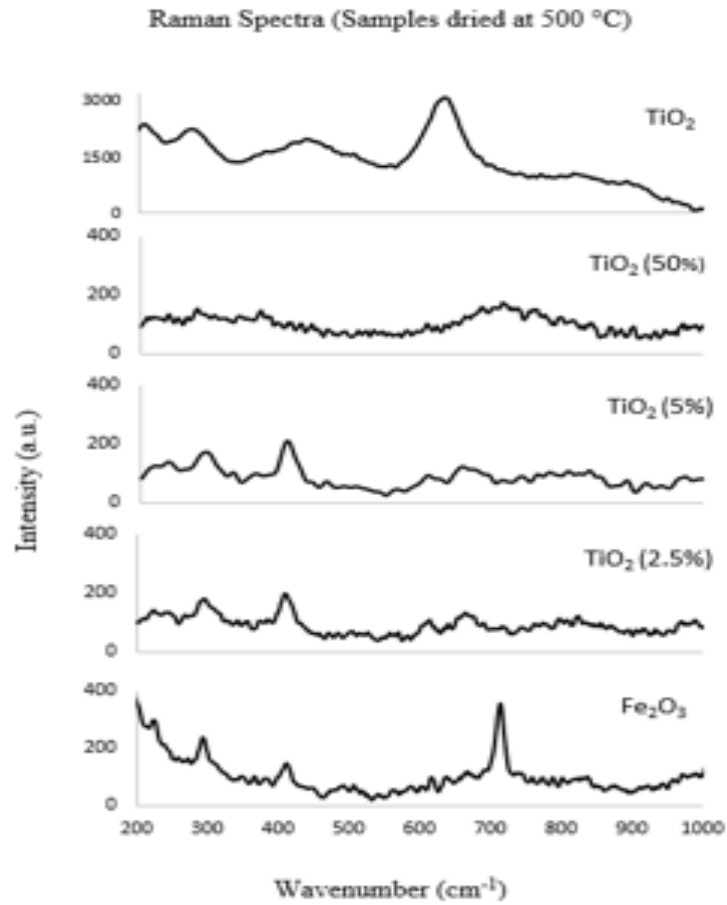


Figure 6.4 Raman spectra of α -Fe₂O₃-TiO₂ nanomaterials

6.3.4 Scanning Electron Microscopy (SEM)

The SEM pictures of nanomaterials were measured using a Field Emission Hitachi S800 Scanning Electron Microscope. Figure 5 shows the scanning electron microscopy (SEM) images of Fe_2O_3 , TiO_2 and $\alpha\text{-Fe}_2\text{O}_3\text{-TiO}_2$ with different concentrations of TiO_2 (50, 5 and 2.5 %) samples. Figure 5 (a-b) shows SEM images of synthesized TiO_2 and $\alpha\text{-Fe}_2\text{O}_3$ nanomaterial samples respectively, with an average diameter of particles at less than $10\ \mu\text{m}$. On the other hand, Figure 5 (c-e) shows SEM images of $\alpha\text{-Fe}_2\text{O}_3\text{-TiO}_2$ with different concentrations of TiO_2 (50, 5 and 2.5 %) nanomaterials. Figure 5 (d-f) shows the urchin-like nanostructure consisting of nanowires e, thus the average particle size is over $10\ \mu\text{m}$. The urchin-like nanostructure includes more surface area, which may improve the effective interface of $\alpha\text{-Fe}_2\text{O}_3$ and improve performance of the water-splitting application [172, 179, 183].

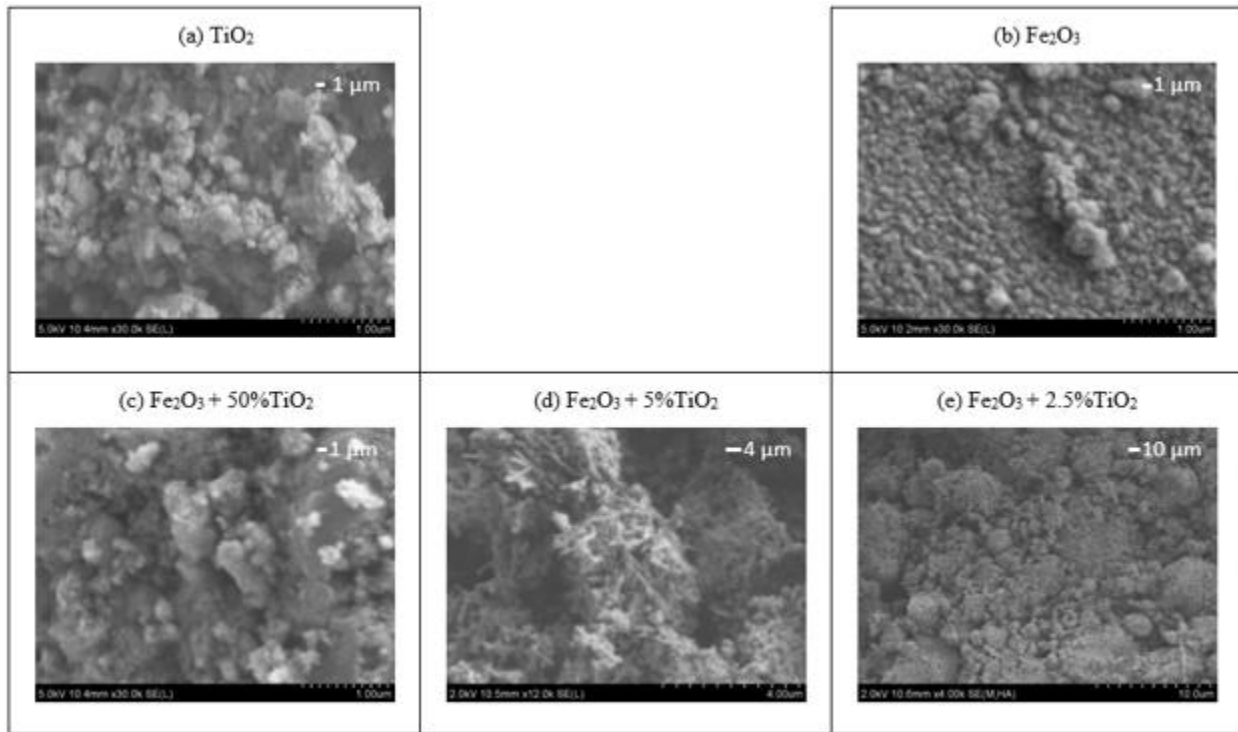


Figure 6.5 SEM images of (a) $\alpha\text{-Fe}_2\text{O}_3$ (b) TiO_2 (c) $\alpha\text{-Fe}_2\text{O}_3 + 50\%\text{TiO}_2$ (d) $\alpha\text{-Fe}_2\text{O}_3 + 5\%\text{TiO}_2$ (e) $\alpha\text{-Fe}_2\text{O}_3 + 2.5\%\text{TiO}_2$ dried at $500\ ^\circ\text{C}$

6.4 Electrochemical Studies

6.4.1 Chronoamperometry

The electrochemical studies on various α -Fe₂O₃-TiO₂ nanomaterial films were conducted using Potentiostat/galvanostate of model “PGZ 301 Dynamic EIS voltammetry” from Volta lab. The chronoamperometry curve was measured using two electrodes consisting of α -Fe₂O₃-TiO₂ nanomaterial (50% of TiO₂ dried at 500 °C) film as the working electrode and RRPHTTh-ND as the counter electrode. 1M of NaOH solution was utilized as the electrolyte. The electrochemical photo response was measured by switching the lamp on and off (60W). Figure 6 shows the chronoamperometry photocurrent curve with time (seconds) for oxidation-reduction reaction of α -Fe₂O₃-TiO₂ film. When charge potential was at 1000 mV, current density was 120 μ m/cm² of the maximum and 90 μ m/cm² of average as shown in Figure 6 (a); when charge potential was at 2000 mV, current density was 800 μ m/cm² of the maximum and 300 μ m/cm² of average as shown in Figure 6 (b). The increase of potential shows the larger current density due to the oxidation of water.

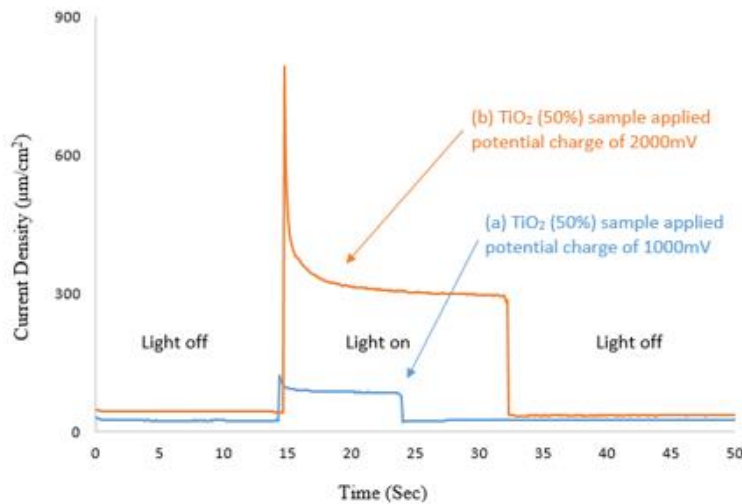


Figure 6.6 Photocurrent response for α -Fe₂O₃-TiO₂ nanomaterial sample with 50% of TiO₂, heat treatment at 500 °C. (a) working electrode applied with 1000 mV of charge potential, (b) applied with 2000 mV of charge potential

6.5 Conclusion

The α -Fe₂O₃-TiO₂ nanomaterial was synthesized with various percentages of TiO₂. The α -Fe₂O₃-TiO₂ nanomaterial can absorb the visible region. The low concentration of TiO₂ (5% and 2.5%) nanomaterial may be concerned with changing the structure of α -Fe₂O₃ nanomaterials based on SEM images. The urchin- nanostructure improves the effective interface of α -Fe₂O₃ and also enhances the performance of the water-splitting application. The TiO₂ sample in α -Fe₂O₃-TiO₂ nanomaterial shows the presence of both phases such as anatase and rutile. In addition, production of photocurrent seems to improve with illumination of the electrode based on α -Fe₂O₃-TiO₂ nanomaterial. TiO₂ nanomaterial contributes to improving the performance of a PEC device based on α -Fe₂O₃-TiO₂ nanomaterial electrode by shifting the absorbing region of light and by expanding the contact area with electrolytes on the α -Fe₂O₃-TiO₂ surface. The increase of potential shows the larger current density due to oxidation of water using α -Fe₂O₃-TiO₂ nanomaterial film.

CHAPTER 7: CONCLUSION

The most efficient free resources that can generate sustainable energy are sunlight and water. The processes being developed using solar energy as the power source to energize the splitting of water to produce hydrogen gas are very promising in their potential for completely replacing fossil fuels as the world's primary source of energy. Photomaterials have been tested successfully to be used in photoelectrochemical cells for water-splitting applications. Alpha-hematite is a promising photomaterial with a low bandgap of 2.1 eV and it can absorb visible light. Doping alpha-hematite material with aluminum, molybdenum disulfide, and titanium dioxide showed more changes in the structure, morphology, and particle size compared to pristine alpha-hematite.

Alpha-hematite material properties are enhanced by doping with aluminum in various percentages (0.5, 10, 20, 30), and the bandgap was varied from 2.1 to 2.4 eV. Also, the charge transport properties were improved through the strain introduction in the lattice structure, thus increasing the light absorption. The increase of Al contents in α -Fe₂O₃ shows clustering due to the denser formation of the Al- α -Fe₂O₃ particle. The 20% Al doped α -Fe₂O₃ has blue shift that absorbs visible light and contains a marked increase in the photocurrent (35 μ A/cm²).

The MoS₂- α -Fe₂O₃ nanocomposite has changed the morphology of α -Fe₂O₃ to resemble blooming flowers. The MoS₂ could play a central role in charge transfer with slow recombination of electron-hole pairs created due to photo-energy with a charge transfer rate between surface and electrons. The chronoamperometry was used to estimate the photocurrent; the enhanced

photocurrent is observed with MoS₂ doping in MoS₂- α -Fe₂O₃ nanomaterial (180 μ A/cm²) and is more effective than the Al- α -Fe₂O₃ nanocomposite.

MoS₂ can easily extract the holes from an n-type semiconductor by fabricating a p-n configuration. Alpha-hematite material has been enhanced by using the p-n configuration and provides high efficiency photoelectrochemical conversions. The p-n photoelectrochemical cell is stable and allows for eliminating the photo corrosion process. The chronoamperometry results showed that 1% MoS₂ in MoS₂- α -Fe₂O₃ nanocomposite can be a suitable structure to obtain a higher photocurrent density (450 μ A/cm²).

The TiO₂ with p-n configuration contributes to improving the performance of the PEC device based on α -Fe₂O₃-TiO₂ nanomaterial as the n-electrode and RRPHTTh-ND as the p-electrode by shifting the absorption region of light and by expanding the contact area with electrolytes on the α -Fe₂O₃-TiO₂ surface. The increasing potential shows the larger current density (800 μ A/cm²) due to oxidation of water using α -Fe₂O₃-TiO₂ nanomaterial film.

7.1 Future Work

- Exploration of more dichalcogenide materials that consider to be highly semiconducting materials, such as WS₂, MoTe₂, and MoSe₂ for doping and composite to alpha- hematite for photoelectrochemical applications.
- Integration of photovoltaic cells with photoelectrochemical properties of alpha-hematite materials to obtain a free solar current.
- Exploration of p-n configuration-based photochemical properties by using a nanodiamond-conducting polymer that easily obtains p-type semiconductor materials such as polymethythiophene, polyethylenedioxythiophene, and polycarbazole.

- MoO₂ synthesis through hydrothermal technique is equal to or better than TiO₂ photocatalytic cells, as proven by the recent work from our group

REFERENCES

1. Zhang, L., C.C. Xu, and P. Champagne, *Overview of recent advances in thermo-chemical conversion of biomass*. Energy Conversion and Management, 2010. **51**(5): p. 969-982.
2. Saxena, R., et al., *Thermo-chemical routes for hydrogen rich gas from biomass: a review*. Renewable and Sustainable Energy Reviews, 2008. **12**(7): p. 1909-1927.
3. Kalinci, Y., A. Hepbasli, and I. Dincer, *Biomass-based hydrogen production: a review and analysis*. International journal of hydrogen energy, 2009. **34**(21): p. 8799-8817.
4. Panwar, N., R. Kothari, and V. Tyagi, *Thermo chemical conversion of biomass–Eco friendly energy routes*. Renewable and Sustainable Energy Reviews, 2012. **16**(4): p. 1801-1816.
5. Abanades, S., et al., *Investigation of reactive cerium-based oxides for H₂ production by thermochemical two-step water-splitting*. Journal of Materials Science, 2010. **45**(15): p. 4163-4173.
6. Locke, B.R. and K.-Y. Shih, *Review of the methods to form hydrogen peroxide in electrical discharge plasma with liquid water*. Plasma Sources Science and Technology, 2011. **20**(3): p. 034006.
7. GyoáKoo, I., et al., *Platinum nanoparticles prepared by a plasma-chemical reduction method*. Journal of Materials Chemistry, 2005. **15**(38): p. 4125-4128.
8. Etievant, C. and M. Roshd, *Method and devices for producing hydrogen by plasma reformer*. 2001, Google Patents.
9. Xiang, Q., J. Yu, and M. Jaroniec, *Preparation and enhanced visible-light photocatalytic H₂-production activity of graphene/C₃N₄ composites*. The Journal of Physical Chemistry C, 2011. **115**(15): p. 7355-7363.
10. Zhang, J., et al., *Visible light photocatalytic H₂-production activity of CuS/ZnS porous nanosheets based on photoinduced interfacial charge transfer*. Nano Letters, 2011. **11**(11): p. 4774-4779.
11. Xiang, Q., J. Yu, and M. Jaroniec, *Synergetic effect of MoS₂ and graphene as cocatalysts for enhanced photocatalytic H₂ production activity of TiO₂ nanoparticles*. Journal of the American Chemical Society, 2012. **134**(15): p. 6575-6578.

12. Park, H.S., et al., *A novel electrochemically active and Fe (III)-reducing bacterium phylogenetically related to Clostridium butyricum isolated from a microbial fuel cell*. *Anaerobe*, 2001. **7**(6): p. 297-306.
13. Armstrong, F.A., et al., *Dynamic electrochemical investigations of hydrogen oxidation and production by enzymes and implications for future technology*. *Chemical Society Reviews*, 2009. **38**(1): p. 36-51.
14. Fujishima, A., K. Kohayakawa, and K. Honda, *Hydrogen production under sunlight with an electrochemical photocell*. *Journal of the Electrochemical Society*, 1975. **122**: p. 1487-1489.
15. Grätzel, M., *Photochemical methods for the conversion of light into chemical energy*. *Berichte der Bunsengesellschaft für physikalische Chemie*, 1980. **84**(10): p. 981-991.
16. Brown, K.A., et al., *Characterization of photochemical processes for H₂ production by CdS nanorod-[FeFe] hydrogenase complexes*. *Journal of the American Chemical Society*, 2012. **134**(12): p. 5627-5636.
17. Zhang, L., et al., *In situ photochemical synthesis of Zn-doped Cu₂O hollow microcubes for high efficient photocatalytic H₂ production*. *ACS Sustainable Chemistry & Engineering*, 2014. **2**(6): p. 1446-1452.
18. Stuhl, F. and H. Niki, *Pulsed Vacuum-uv Photochemical Study of Reactions of OH with H₂, D₂, and CO Using a Resonance-Fluorescent Detection Method*. *The Journal of Chemical Physics*, 1972. **57**(9): p. 3671-3677.
19. Buehler, N., K. Meier, and J.F. Reber, *Photochemical hydrogen production with cadmium sulfide suspensions*. *The Journal of Physical Chemistry*, 1984. **88**(15): p. 3261-3268.
20. Chen, Z., et al., *Accelerating materials development for photoelectrochemical hydrogen production: Standards for methods, definitions, and reporting protocols*. *Journal of Materials Research*, 2010. **25**(1): p. 3-16.
21. Wang, Y., Y. Wang, and R. Xu, *Photochemical deposition of Pt on CdS for H₂ evolution from water: markedly enhanced activity by controlling Pt reduction environment*. *The Journal of Physical Chemistry C*, 2013. **117**(2): p. 783-790.
22. Lewis, N.S. and D.G. Nocera, *Powering the planet: Chemical challenges in solar energy utilization*. *Proceedings of the National Academy of Sciences*, 2006. **103**(43): p. 15729-15735.
23. Singh, B.S.M., *Nanotechnology in Solar Hydrogen Production*, in *Carbon and Oxide Nanostructures*. 2010, Springer. p. 263-280.

24. Alenzi, N., et al., *Photoelectrochemical hydrogen production from water/methanol decomposition using Ag/TiO₂ nanocomposite thin films*. international journal of hydrogen energy, 2010. **35**(21): p. 11768-11775.
25. Preethi, V. and S. Kanmani, *Photocatalytic hydrogen production*. Materials Science in Semiconductor Processing, 2013. **16**(3): p. 561-575.
26. Tamirat, A.G., et al., *Using hematite for photoelectrochemical water splitting: a review of current progress and challenges*. Nanoscale Horizons, 2016.
27. Basavegowda, N., K. Mishra, and Y.R. Lee, *Synthesis, characterization, and catalytic applications of hematite (α -Fe₂O₃) nanoparticles as reusable nanocatalyst*. Advances in Natural Sciences: Nanoscience and Nanotechnology, 2017. **8**(2): p. 025017.
28. Alagiri, M. and S.B.A. Hamid, *Synthesis, characterization and photocatalytic application of α -Fe₂O₃ microflower*. Materials Letters, 2014. **136**: p. 329-332.
29. Goncalves, R.H., B.H. Lima, and E.R. Leite, *Magnetite colloidal nanocrystals: A facile pathway to prepare mesoporous hematite thin films for photoelectrochemical water splitting*. Journal of the American Chemical Society, 2011. **133**(15): p. 6012-6019.
30. Lassoued, A., et al., *Control of the shape and size of iron oxide (α -Fe₂O₃) nanoparticles synthesized through the chemical precipitation method*. Results in physics, 2017. **7**: p. 3007-3015.
31. Yue, G., et al., *Efficient growth of aligned SnO₂ nanorod arrays on hematite (α -Fe₂O₃) nanotube arrays for photoelectrochemical and photocatalytic applications*. Journal of Materials Science: Materials in Electronics, 2013. **24**(9): p. 3324-3329.
32. Nasibulin, A.G., et al., *Simple and rapid synthesis of α -Fe₂O₃ nanowires under ambient conditions*. Nano Research, 2009. **2**(5): p. 373-379.
33. Liu, J., et al., *General strategy for doping impurities (Ge, Si, Mn, Sn, Ti) in hematite nanocrystals*. The Journal of Physical chemistry c, 2012. **116**(8): p. 4986-4992.
34. He, D., et al., *Construct Fe²⁺ species and Au particles for significantly enhanced photoelectrochemical performance of α -Fe₂O₃ by ion implantation*. Science China Materials, 2018. **61**(6): p. 878-886.
35. Ye, K.-H., et al., *A novel CoOOH/(Ti, C)-Fe₂O₃ nanorod photoanode for photoelectrochemical water splitting*. Science China Materials, 2018: p. 1-8.
36. Huang, M.-C., et al., *Magnetron sputtering process of carbon-doped α -Fe₂O₃ thin films for photoelectrochemical water splitting*. Journal of Alloys and Compounds, 2015. **636**: p. 176-182.

37. Shen, S., et al., *Effect of Cr doping on the photoelectrochemical performance of hematite nanorod photoanodes*. Nano Energy, 2012. **1**(5): p. 732-741.
38. Wang, J., et al., *Enhanced photoelectrochemical water splitting performance of hematite nanorods by Co and Sn co-doping*. International Journal of Hydrogen Energy, 2017. **42**(49): p. 29140-29149.
39. Zheng, C., et al., *NaF-assisted hydrothermal synthesis of Ti-doped hematite nanocubes with enhanced photoelectrochemical activity for water splitting*. Applied Surface Science, 2015. **359**: p. 805-811.
40. Shen, S., et al., *Physical and photoelectrochemical characterization of Ti-doped hematite photoanodes prepared by solution growth*. Journal of Materials Chemistry A, 2013. **1**(46): p. 14498-14506.
41. Han, S., et al., *Enhancing photoelectrochemical activity of nanocrystalline WO₃ electrodes by surface tuning with Fe (III)*. international journal of hydrogen energy, 2012. **37**(22): p. 16810-16816.
42. Kumar, P., et al., *Electrodeposited zirconium-doped α -Fe₂O₃ thin film for photoelectrochemical water splitting*. international journal of hydrogen energy, 2011. **36**(4): p. 2777-2784.
43. Zhang, R., et al., *Enhanced Photoelectrochemical Water Oxidation Performance of Fe₂O₃ Nanorods Array by S Doping*. ACS Sustainable Chemistry & Engineering, 2017. **5**(9): p. 7502-7506.
44. Natarajan, K., M. Saraf, and S.M. Mobin, *Visible-Light-Induced Water Splitting Based on a Novel α -Fe₂O₃/CdS Heterostructure*. ACS Omega, 2017. **2**(7): p. 3447-3456.
45. Kim, J.H., et al., *Hetero-type dual photoanodes for unbiased solar water splitting with extended light harvesting*. Nature communications, 2016. **7**: p. 13380.
47. Hu, Y.-S., et al., *Pt-doped α -Fe₂O₃ thin films active for photoelectrochemical water splitting*. Chemistry of Materials, 2008. **20**(12): p. 3803-3805.
48. Hsu, Y.-K., Y.-C. Chen, and Y.-G. Lin, *Novel ZnO/Fe₂O₃ core-shell nanowires for photoelectrochemical water splitting*. ACS applied materials & interfaces, 2015. **7**(25): p. 14157-14162.
49. Qi, X., et al., *Electrochemical synthesis of p-type Zn-doped α -Fe₂O₃ nanotube arrays for photoelectrochemical water splitting*. Chemical Communications, 2013. **49**(51): p. 5742-5744.

50. Garcia, D., et al., *Sensors based on Ag-loaded hematite (α -Fe₂O₃) nanoparticles for methyl mercaptan detection at room temperature*. Analytical Chemistry Research, 2017. **12**: p. 74-81.
51. Cheng, K., et al., *Quantum size effect on surface photovoltage spectra: alpha-Fe₂O₃ nanocrystals on the surface of monodispersed silica microsphere*. The Journal of Physical Chemistry B, 2006. **110**(14): p. 7259-7264.
52. Ji, J., et al., *A layer-by-layer self-assembled Fe₂O₃ nanorod-based composite multilayer film on ITO anode in microbial fuel cell*. Colloids and Surfaces A: Physicochemical and Engineering Aspects, 2011. **390**(1-3): p. 56-61.
53. Zhou, W., et al., *Mesoporous TiO₂/ α -Fe₂O₃: bifunctional composites for effective elimination of arsenite contamination through simultaneous photocatalytic oxidation and adsorption*. The Journal of Physical Chemistry C, 2008. **112**(49): p. 19584-19589.
54. Xu, X., et al., *Spindle-like mesoporous α -Fe₂O₃ anode material prepared from MOF template for high-rate lithium batteries*. Nano letters, 2012. **12**(9): p. 4988-4991.
55. Lu, X.-F., et al., *α -Fe₂O₃@ PANI core-shell nanowire arrays as negative electrodes for asymmetric supercapacitors*. ACS applied materials & interfaces, 2015. **7**(27): p. 14843-14850.
56. Umare, S. and B. Shambharkar, *Synthesis, characterization, and corrosion inhibition study of polyaniline- α -Fe₂O₃ nanocomposite*. Journal of Applied Polymer Science, 2013. **127**(5): p. 3349-3355.
57. Wheeler, D.A., et al., *Nanostructured hematite: synthesis, characterization, charge carrier dynamics, and photoelectrochemical properties*. Energy & Environmental Science, 2012. **5**(5): p. 6682-6702.
58. Wang, H., et al., *Photoelectrochemistry of nanostructured WO₃ thin film electrodes for water oxidation: mechanism of electron transport*. The Journal of Physical Chemistry B, 2000. **104**(24): p. 5686-5696.
59. Ahn, K.-S., et al., *Photoelectrochemical properties of N-incorporated ZnO films deposited by reactive RF magnetron sputtering*. Journal of the Electrochemical Society, 2007. **154**(9): p. B956-B959.
60. Cao, F., et al., *Electron transport in porous nanocrystalline TiO₂ photoelectrochemical cells*. The Journal of Physical Chemistry, 1996. **100**(42): p. 17021-17027.
61. Zhao, H., et al., *Photoelectrocatalytic oxidation of organic compounds at nanoporous TiO₂ electrodes in a thin-layer photoelectrochemical cell*. Journal of Catalysis, 2007. **250**(1): p. 102-109.

62. Bjoerksten, U., J. Moser, and M. Graetzel, *Photoelectrochemical studies on nanocrystalline hematite films*. Chemistry of materials, 1994. **6**(6): p. 858-863.
63. Ling, Y., et al., *Sn-doped hematite nanostructures for photoelectrochemical water splitting*. Nano letters, 2011. **11**(5): p. 2119-2125.
64. Jia, C.J., et al., *Single-Crystalline Iron Oxide Nanotubes*. Angewandte Chemie, 2005. **117**(28): p. 4402-4407.
65. Mao, A., et al., *Controlled synthesis of vertically aligned hematite on conducting substrate for photoelectrochemical cells: nanorods versus nanotubes*. ACS applied materials & interfaces, 2011. **3**(6): p. 1852-1858.
66. Wu, W., et al., *Large-scale and controlled synthesis of iron oxide magnetic short nanotubes: shape evolution, growth mechanism, and magnetic properties*. The Journal of Physical Chemistry C, 2010. **114**(39): p. 16092-16103.
67. Li, S., et al., *Shape-control fabrication and characterization of the airplane-like FeO (OH) and Fe₂O₃ nanostructures*. Crystal growth & design, 2006. **6**(2): p. 351-353.
68. Sivula, K., F. Le Formal, and M. Grätzel, *Solar water splitting: progress using hematite (α -Fe₂O₃) photoelectrodes*. ChemSusChem, 2011. **4**(4): p. 432-449.
69. Shinde, S., et al., *Physical properties of hematite α -Fe₂O₃ thin films: application to photoelectrochemical solar cells*. Journal of Semiconductors, 2011. **32**(1): p. 013001.
70. Satsangi, V.R., et al., *Nanostructured hematite for photoelectrochemical generation of hydrogen*. International Journal of Hydrogen Energy, 2008. **33**(1): p. 312-318.
71. Hahn, N.T. and C.B. Mullins, *Photoelectrochemical performance of nanostructured Ti- and Sn-doped α -Fe₂O₃ photoanodes*. Chemistry of Materials, 2010. **22**(23): p. 6474-6482.
72. Boudjemaa, A., et al., *Physical and photo-electrochemical characterizations of α -Fe₂O₃. Application for hydrogen production*. International Journal of Hydrogen Energy, 2009. **34**(10): p. 4268-4274.
73. Ingler Jr, W.B., J.P. Baltrus, and S.U. Khan, *Photoresponse of p-type zinc-doped iron (III) oxide thin films*. Journal of the American Chemical Society, 2004. **126**(33): p. 10238-10239.
74. Kleiman-Shwarscstein, A., et al., *Electrodeposited aluminum-doped α -Fe₂O₃ photoelectrodes: experiment and theory*. Chemistry of Materials, 2009. **22**(2): p. 510-517.

75. Satsangi, V.R., *Characterization of Zn-doped hematite thin films for photoelectrochemical splitting of water*. Current science, 2006. **91**(8).
76. Lukowski, M.A. and S. Jin, *Improved synthesis and electrical properties of Si-doped α -Fe₂O₃ nanowires*. The Journal of Physical Chemistry C, 2011. **115**(25): p. 12388-12395.
77. Warwick, M.E., et al., *Pt-functionalized Fe₂O₃ photoanodes for solar water splitting: the role of hematite nano-organization and the platinum redox state*. Physical Chemistry Chemical Physics, 2015. **17**(19): p. 12899-12907.
78. Rowley, J.G., et al., *Combinatorial Discovery Through a Distributed Outreach Program: Investigation of the Photoelectrolysis Activity of p-Type Fe, Cr, Al Oxides*. ACS applied materials & interfaces, 2014. **6**(12): p. 9046-9052.
79. Mao, A., et al., *Controlled growth of vertically oriented hematite/Pt composite nanorod arrays: use for photoelectrochemical water splitting*. Nanotechnology, 2011. **22**(17): p. 175703.
80. Castriota, M., et al., *Micro-Raman characterizations of Pompei's mortars*. Journal of Raman Spectroscopy, 2008. **39**(2): p. 295-301.
81. Srivastava, S., *Synthesis and characterization of iron oxide nanoparticle from FeCl₃ by using polyvinyl alcohol*. International Journal of Physical and Social Sciences, 2012. **2**(5): p. 161-184.
82. Woo, K., et al., *Sol-gel mediated synthesis of Fe₂O₃ nanorods*. Advanced Materials, 2003. **15**(20): p. 1761-1764.
83. Zoppi, A., et al., *Al-for-Fe substitution in hematite: the effect of low Al concentrations in the Raman spectrum of Fe₂O₃*. Journal of Raman Spectroscopy, 2008. **39**(1): p. 40-46.
84. Nunzio Giambone, A.K.a.M.K.R., *Comparative photoelectrochemical studies of regio-regular polyhexylthiophene with microdiamond, nanodiamond and hexagonal boron nitride hybrid films*. Thin Solid Films, 2016(in press).
85. Basnayaka, P.A., et al. *Photovoltaic properties of multi walled carbon nanotubes-poly (3-octathiophene) conducting polymer blends structures*. in *MRS Proceedings*. 2013. Cambridge Univ Press.
86. Phuan, Y.W., et al., *Effects of annealing temperature on the physicochemical, optical and photoelectrochemical properties of nanostructured hematite thin films prepared via electrodeposition method*. Materials Research Bulletin, 2015. **69**: p. 71-77.
87. Splitting, S.W., *Progress Using Hematite (α -Fe₂O₃) Photoelectrodes* Sivula, Kevin; Le Formal, Florian; Graetzel, Michael. ChemSusChem, 2011. **4**(4): p. 432-449.

88. Li, Y., et al., *MoS₂ nanoparticles grown on graphene: an advanced catalyst for the hydrogen evolution reaction*. Journal of the American Chemical Society, 2011. **133**(19): p. 7296-7299.
89. Hiralal, P., et al., *Nanostructured hematite photoelectrochemical electrodes prepared by the low temperature thermal oxidation of iron*. Solar Energy Materials and Solar Cells, 2011. **95**(7): p. 1819-1825.
90. Ahn, H.-J., et al., *MoS_x supported hematite with enhanced photoelectrochemical performance*. Journal of Materials Chemistry A, 2015. **3**(43): p. 21444-21450.
91. Hisatomi, T., J. Kubota, and K. Domen, *Recent advances in semiconductors for photocatalytic and photoelectrochemical water splitting*. Chemical Society Reviews, 2014. **43**(22): p. 7520-7535.
92. Kim, J.Y., et al., *Single-crystalline, wormlike hematite photoanodes for efficient solar water splitting*. Scientific reports, 2013. **3**: p. 2681.
93. Kment, S., et al., *On the improvement of PEC activity of hematite thin films deposited by high-power pulsed magnetron sputtering method*. Applied Catalysis B: Environmental, 2015. **165**: p. 344-350.
94. Hisatomi, T., et al., *Enhancement in the performance of ultrathin hematite photoanode for water splitting by an oxide underlayer*. Advanced Materials, 2012. **24**(20): p. 2699-2702.
95. Ahn, H.-J., et al., *Nanoporous hematite structures to overcome short diffusion lengths in water splitting*. Journal of Materials Chemistry A, 2014. **2**(47): p. 19999-20003.
96. Du, C., et al., *Hematite-based water splitting with low turn-on voltages*. Angewandte Chemie International Edition, 2013. **52**(48): p. 12692-12695.
97. Desai, J., et al., *FT-IR, XPS and PEC characterization of spray deposited hematite thin films*. Applied surface science, 2005. **252**(5): p. 1870-1875.
98. Bassi, P.S., L.H. Wong, and J. Barber, *Iron based photoanodes for solar fuel production*. Physical Chemistry Chemical Physics, 2014. **16**(24): p. 11834-11842.
99. Kumari, S., et al., *Characterization of Zn-doped hematite thin films for photoelectrochemical splitting of water*. Current science, 2006. **91**(8): p. 1062-1073.
100. Jorand Sartoretti, C., et al., *Photoelectrochemical oxidation of water at transparent ferric oxide film electrodes*. The Journal of Physical Chemistry B, 2005. **109**(28): p. 13685-13692.

101. Kennedy, J.H. and K.W. Frese, *Photooxidation of water at α -Fe₂O₃ electrodes*. Journal of the Electrochemical Society, 1978. **125**(5): p. 709-714.
102. Kleiman-Shwarscstein, A., et al., *Electrodeposition of α -Fe₂O₃ doped with Mo or Cr as photoanodes for photocatalytic water splitting*. The Journal of Physical Chemistry C, 2008. **112**(40): p. 15900-15907.
103. Saremi-Yarahmadi, S., et al., *Nanostructured α -Fe₂O₃ electrodes for solar driven water splitting: effect of doping agents on preparation and performance*. The Journal of Physical Chemistry C, 2009. **113**(12): p. 4768-4778.
104. Kay, A., I. Cesar, and M. Grätzel, *New benchmark for water photooxidation by nanostructured α -Fe₂O₃ films*. Journal of the American Chemical Society, 2006. **128**(49): p. 15714-15721.
105. Ding, Q., et al., *Efficient photoelectrochemical hydrogen generation using heterostructures of Si and chemically exfoliated metallic MoS₂*. Journal of the American Chemical Society, 2014. **136**(24): p. 8504-8507.
106. Yoon, K.-Y., et al., *Hematite-based photoelectrochemical water splitting supported by inverse opal structures of graphene*. ACS applied materials & interfaces, 2014. **6**(24): p. 22634-22639.
107. Meng, F., et al., *Photocatalytic water oxidation by hematite/reduced graphene oxide composites*. ACS Catalysis, 2013. **3**(4): p. 746-751.
108. Liu, Y., Y.-X. Yu, and W.-D. Zhang, *MoS₂/CdS heterojunction with high photoelectrochemical activity for H₂ evolution under visible light: the role of MoS₂*. The Journal of Physical Chemistry C, 2013. **117**(25): p. 12949-12957.
109. Alrobei, H. *α -hematite-molybdenum disulfide and polyhexylthiophene (RRPHTh)-nanodiamond (ND) electrodes for photoelectrochemical applications*. in *3rd International Conference on Smart Materials & Structures*. 2017. Orlando, Florida, USA.
110. Hussein Alrobei, Ashok Kumar, Manoj K. Ram. *Aluminum Doped α -Hematite for Photoelectrochemical Applications*. in *Research Day 2015 at USF College of Engineering*. 2015. Tampa, Florida, USA.
111. Ram, H.A.M.K., *Aluminum - α -hematite thin films for photoelectrochemical applications*. Surface Review and Letters (communicated), 2017.
112. Chen, Z., et al., *Core-shell MoO₃-MoS₂ nanowires for hydrogen evolution: a functional design for electrocatalytic materials*. Nano letters, 2011. **11**(10): p. 4168-4175.
113. Bonde, J., et al., *Hydrogen evolution on nano-particulate transition metal sulfides*. Faraday discussions, 2009. **140**: p. 219-231.

114. Kibsgaard, J., et al., *Engineering the surface structure of MoS₂ to preferentially expose active edge sites for electrocatalysis*. Nature materials, 2012. **11**(11): p. 963-969.
115. Thurston, T. and J. Wilcoxon, *Photooxidation of organic chemicals catalyzed by nanoscale MoS₂*. The Journal of Physical Chemistry B, 1999. **103**(1): p. 11-17.
116. Han, S., et al., *One-Step Hydrothermal Synthesis of 2D Hexagonal Nanoplates of α -Fe₂O₃/Graphene Composites with Enhanced Photocatalytic Activity*. Advanced Functional Materials, 2014. **24**(36): p. 5719-5727.
117. Hussein Alrobei, Ashok Kumar, , Manoj K. Ram. *Doped α -hematite with Molybdenum Sulfides MoS₂ for photoelectrochemical applications*. in *9th Annual College of Engineering Research Day*. 2016. Tampa, FL, USA.
118. Chemelewski, W.D., et al., *Bandgap engineering of Fe₂O₃ with Cr—application to photoelectrochemical oxidation*. Physical Chemistry Chemical Physics, 2016. **18**(3): p. 1644-1648.
119. Sun, S., et al., *MoS₂ and graphene as dual, cocatalysts for enhanced visible light photocatalytic activity of Fe₂O₃*. Journal of Sol-Gel Science and Technology: p. 1-9.
120. Gao, D., et al., *Ferromagnetism in freestanding MoS₂ nanosheets*. Nanoscale research letters, 2013. **8**(1): p. 129.
121. Zhang, Y., et al., *Synthesis of S-rich flower-like Fe₂O₃-MoS₂ for Cr (VI) removal*. Separation Science and Technology, 2016(just-accepted).
122. Yang, X., et al., *High Efficient Photo-Fenton Catalyst of α -Fe₂O₃/MoS₂ Hierarchical Nanoheterostructures: Reutilization for Supercapacitors*. Scientific Reports, 2016. **6**.
123. Ye, L., D. Wang, and S. Chen, *Fabrication and Enhanced Photoelectrochemical Performance of MoS₂/S-Doped g-C₃N₄ Heterojunction Film*. ACS applied materials & interfaces, 2016. **8**(8): p. 5280-5289.
124. Zanello, P., *Inorganic electrochemistry: theory, practice and applications*. 2003: Royal Society of Chemistry.
125. Bard, A.J., *LR Faulkner Electrochemical Methods*. 1980, Wiley, New York.
126. Ram, M.K., E. Maccioni, and C. Nicolini, *The electrochromic response of polyaniline and its copolymeric systems*. Thin solid films, 1997. **303**(1-2): p. 27-33.
127. Ram, M., N. Sundaresan, and B. Malhotra, *Performance of electrochromic cells of polyaniline in polymeric electrolytes*. Journal of materials science letters, 1994. **13**(20): p. 1490-1493.

128. Cesar, I., et al., *Translucent thin film Fe₂O₃ photoanodes for efficient water splitting by sunlight: nanostructure-directing effect of Si-doping*. Journal of the American Chemical Society, 2006. **128**(14): p. 4582-4583.
129. Duret, A. and M. Grätzel, *Visible light-induced water oxidation on mesoscopic α -Fe₂O₃ films made by ultrasonic spray pyrolysis*. The Journal of Physical Chemistry B, 2005. **109**(36): p. 17184-17191.
130. Meng, F., et al., *Solar hydrogen generation by nanoscale p–n junction of p-type molybdenum disulfide/n-type nitrogen-doped reduced graphene oxide*. Journal of the American Chemical Society, 2013. **135**(28): p. 10286-10289.
131. Hahn, N.T., et al., *Reactive ballistic deposition of α -Fe₂O₃ thin films for photoelectrochemical water oxidation*. ACS nano, 2010. **4**(4): p. 1977-1986.
132. van de Krol, R., Y. Liang, and J. Schoonman, *Solar hydrogen production with nanostructured metal oxides*. Journal of Materials Chemistry, 2008. **18**(20): p. 2311-2320.
133. Mohapatra, S.K., et al., *Water photooxidation by smooth and ultrathin α -Fe₂O₃ nanotube arrays*. Chemistry of Materials, 2009. **21**(14): p. 3048-3055.
134. Chirita, M., et al., *Fe₂O₃–nanoparticles, physical properties and their photochemical and photoelectrochemical applications*. Chem. Bull, 2009. **54**(68): p. 1-8.
135. Lin, Y., et al., *Nanonet-based hematite heteronanostructures for efficient solar water splitting*. Journal of the American Chemical Society, 2011. **133**(8): p. 2398-2401.
136. Liu, Y., Y.-X. Yu, and W.-D. Zhang, *Photoelectrochemical properties of Ni-doped Fe₂O₃ thin films prepared by electrodeposition*. Electrochimica Acta, 2012. **59**: p. 121-127.
137. Mehraj, O., et al., *A highly efficient visible-light-driven novel pn junction Fe₂O₃/BiOI photocatalyst: Surface decoration of BiOI nanosheets with Fe₂O₃ nanoparticles*. Applied Surface Science, 2016. **387**: p. 642-651.
138. Melero, J., et al., *Nanocomposite Fe₂O₃/SBA-15: An efficient and stable catalyst for the catalytic wet peroxidation of phenolic aqueous solutions*. Chemical Engineering Journal, 2007. **131**(1-3): p. 245-256.
139. Koutsoukos, P., W. Norde, and J. Lyklema, *Protein adsorption on hematite (α -Fe₂O₃) surfaces*. Journal of colloid and interface science, 1983. **95**(2): p. 385-397.
140. Alrobei, H., A. Kumar, and M.K. Ram, *ALUMINUM– α -HEMATITE THIN FILMS FOR PHOTOELECTROCHEMICAL APPLICATIONS*. Surface Review and Letters, 2017: p. 1950031.

142. Sun, Q.-C., et al., *Observation of a Burstein–Moss shift in rhenium-doped MoS₂ nanoparticles*. ACS nano, 2013. **7**(4): p. 3506-3511.
143. Yin, Z., et al., *Single-layer MoS₂ phototransistors*. ACS nano, 2011. **6**(1): p. 74-80.
144. Choi, W., et al., *High-detectivity multilayer MoS₂ phototransistors with spectral response from ultraviolet to infrared*. Advanced materials, 2012. **24**(43): p. 5832-5836.
145. Lee, H.S., et al., *MoS₂ nanosheet phototransistors with thickness-modulated optical energy gap*. Nano letters, 2012. **12**(7): p. 3695-3700.
146. Miao, J., et al., *Surface plasmon-enhanced photodetection in few layer MoS₂ phototransistors with Au nanostructure arrays*. Small, 2015. **11**(20): p. 2392-2398.
147. He, Q., et al., *Fabrication of Flexible MoS₂ Thin-Film Transistor Arrays for Practical Gas-Sensing Applications*. Small, 2012. **8**(19): p. 2994-2999.
148. Wu, S., et al., *Electrochemically reduced single-layer MoS₂ nanosheets: Characterization, properties, and sensing applications*. Small, 2012. **8**(14): p. 2264-2270.
149. Li, H., et al., *Fabrication of single-and multilayer MoS₂ film-based field-effect transistors for sensing NO at room temperature*. small, 2012. **8**(1): p. 63-67.
150. Ram, M.K. and A. Kumar, *Nano-hybrid structured regioregular polyhexylthiophene (RRPHT) blend films for production of photoelectrochemical energy*, U.S. Patent, Editor. 2016: U.S.
151. Ram, M.K., et al., *Novel nanohybrid structured regioregular polyhexylthiophene blend films for photoelectrochemical energy applications*. The Journal of Physical Chemistry C, 2011. **115**(44): p. 21987-21995.
152. Hussein Alrobei, H.Y.L., Ashok Kumar, and Manoj K. Ram, *p-n Based Photoelectrochemical Device for Water Splitting Application Alpha-Hematite (α -Fe₂O₃)-Titanium Dioxide (TiO₂) as N-Electrode & Polyhexylthiophene (RRPHT) - Nanodiamond (ND) as P-Electrode*. MRS Advances, 2017.
153. Ram, M.K. and A. Kumar, *Nano-hybrid structured regioregular polyhexylthiophene (RRPHT) blend films for production of photoelectrochemical energy*. 2016, Google Patents.
154. Sahoo, S., et al., *Characterization of γ -and α -Fe₂O₃ nano powders synthesized by emulsion precipitation-calcination route and rheological behaviour of α -Fe₂O₃*. International Journal of Engineering, Science and Technology, 2010. **2**(8).

155. Alrobei, H., A. Kumar, and M.K. Ram, *A New Insight in the Physical and Photoelectrochemical Properties of Molybdenum Disulfide Alpha-Hematite Nanocomposite Films*. American Journal of Analytical Chemistry, 2017. **8**(08): p. 523.
156. Kim, B.-R., et al., *Effect of TiO₂ supporting layer on Fe₂O₃ photoanode for efficient water splitting*. Progress in Organic Coatings, 2013. **76**(12): p. 1869-1873.
157. Ruth, J.D., et al. *An overview of photoelectrochemical cells (PEC): Mimicking nature to produce hydrogen for fuel cells*. in *SoutheastCon, 2017*. 2017. IEEE.
158. Ni, M., et al., *A review and recent developments in photocatalytic water-splitting using TiO₂ for hydrogen production*. Renewable and Sustainable Energy Reviews, 2007. **11**(3): p. 401-425.
159. Kudo, A., *Photocatalyst materials for water splitting*. Catalysis Surveys from Asia, 2003. **7**(1): p. 31-38.
160. Deng, J., et al., *Ti-doped hematite nanostructures for solar water splitting with high efficiency*. Journal of Applied Physics, 2012. **112**(8): p. 084312.
161. Azad, A., W. Kang, and S.-J. Kim, *Preparation and photoelectrochemical properties of Fe₂O₃-TiO₂ based photoanode for water splitting*. 2014, One Central Press, UK. p. 79-107.
162. Murphy, A., et al., *Efficiency of solar water splitting using semiconductor electrodes*. International journal of hydrogen energy, 2006. **31**(14): p. 1999-2017.
163. Watanabe, A. and H. Kozuka, *Photoanodic Properties of Sol–Gel-Derived Fe₂O₃ Thin Films Containing Dispersed Gold and Silver Particles*. The Journal of Physical Chemistry B, 2003. **107**(46): p. 12713-12720.
164. Li, X., et al., *Revealing the role of TiO₂ surface treatment of hematite nanorods photoanodes for solar water splitting*. ACS applied materials & interfaces, 2015. **7**(31): p. 16960-16966.
165. Moniz, S.J., et al., *Visible-light driven heterojunction photocatalysts for water splitting—a critical review*. Energy & Environmental Science, 2015. **8**(3): p. 731-759.
166. Hwang, Y.J., et al., *Photoelectrochemical properties of TiO₂ nanowire arrays: a study of the dependence on length and atomic layer deposition coating*. Acs Nano, 2012. **6**(6): p. 5060-5069.
167. Fujishima, A., T.N. Rao, and D.A. Tryk, *Titanium dioxide photocatalysis*. Journal of Photochemistry and Photobiology C: Photochemistry Reviews, 2000. **1**(1): p. 1-21.

168. Choudhary, S., et al., *Nanostructured bilayered thin films in photoelectrochemical water splitting—A review*. international journal of hydrogen energy, 2012. **37**(24): p. 18713-18730.
169. Zhou, M., X.W.D. Lou, and Y. Xie, *Two-dimensional nanosheets for photoelectrochemical water splitting: Possibilities and opportunities*. Nano Today, 2013. **8**(6): p. 598-618.
170. Chen, X., et al., *Nanomaterials for renewable energy production and storage*. Chemical Society Reviews, 2012. **41**(23): p. 7909-7937.
171. Malik, A., et al., *Influence of Ce Doping on the Electrical and Optical Properties of TiO₂ and Its Photocatalytic Activity for the Degradation of Remazol Brilliant Blue R*. International Journal of Photoenergy, 2013. **2013**.
172. Zhu, J., et al., *Nanocrystalline Fe/TiO₂ Visible Photocatalyst with a Mesoporous Structure Prepared via a Nonhydrolytic Sol–Gel Route*. The Journal of Physical Chemistry C, 2007. **111**(51): p. 18965-18969.
173. Zandi, O., B.M. Klahr, and T.W. Hamann, *Highly photoactive Ti-doped α -Fe₂O₃ thin film electrodes: resurrection of the dead layer*. Energy & Environmental Science, 2013. **6**(2): p. 634-642.
174. Yang, X., et al., *Improving hematite-based photoelectrochemical water splitting with ultrathin TiO₂ by atomic layer deposition*. ACS applied materials & interfaces, 2014. **6**(15): p. 12005-12011.
175. Johnston, C., G. Sposito, and C. Erickson, *Vibrational probe studies of water interactions with montmorillonite*. Clays and Clay Minerals, 1992. **40**(6): p. 722-730.
176. Zhang, D., *Decomposition of rhodamine 6G in the presence of titania coupling coupled with carbon source as photocatalyst under visible light excitation*. High Energy Chemistry, 2013. **47**(4): p. 177-181.
177. Ahmadi Golsefidi, M., et al., *Synthesis, characterization and photocatalytic activity of Fe₂O₃-TiO₂ nanoparticles and nanocomposites*. Journal of Nanostructures, 2016. **6**(1): p. 64-69.
178. Peña-Flores, J.I., et al., *Fe effect on the optical properties of TiO₂: Fe₂O₃ nanostructured composites supported on SiO₂ microsphere assemblies*. Nanoscale research letters, 2014. **9**(1): p. 499.
179. De Faria, D., S. Venâncio Silva, and M. De Oliveira, *Raman microspectroscopy of some iron oxides and oxyhydroxides*. Journal of Raman spectroscopy, 1997. **28**(11): p. 873-878.

180. Ricci, P.C., et al., *Anatase-to-rutile phase transition in TiO₂ nanoparticles irradiated by visible light*. The Journal of Physical Chemistry C, 2013. **117**(15): p. 7850-7857.
181. Ohsaka, T., F. Izumi, and Y. Fujiki, *Raman spectrum of anatase, TiO₂*. Journal of Raman spectroscopy, 1978. **7**(6): p. 321-324.
182. Mazza, T., et al., *Raman spectroscopy characterization of Ti O 2 rutile nanocrystals*. Physical Review B, 2007. **75**(4): p. 045416.
183. Mirbagheri, N., et al., *Visible light driven photoelectrochemical water oxidation by Zn- and Ti-doped hematite nanostructures*. Acs Catalysis, 2014. **4**(6): p. 2006-2015.

APPENDIX A: COPYRIGHT PERMISSIONS FOR CHAPTERS 3, 4, AND 6

The copyright permission for chapter 3 is below.

6/4/2018 Rightslink® by Copyright Clearance Center

Title: Surface review and letters
Article ID: 0218-625X
Publication: Publication1
Publisher: CCC Republication
Date: Jan 1, 1994
Copyright © 1994, CCC Republication

Logged in as:
HUSSEIN ALROBEI
Account #:
3001284122
[LOGOUT](#)

Order Completed
Thank you for your order.


This Agreement between HUSSEIN ALROBEI ("You") and World Scientific Publishing Co., Inc. ("World Scientific Publishing Co., Inc.") consists of your order details and the terms and conditions provided by World Scientific Publishing Co., Inc. and Copyright Clearance Center.

License number	Reference confirmation email for license number
License date	Jun, 04 2018
Licensed content publisher	World Scientific Publishing Co., Inc.
Licensed content title	Surface review and letters
Licensed content date	Jan 1, 1994
Type of use	Thesis/Dissertation
Requestor type	Author of requested content
Format	Electronic
Portion	chapter/article
The requesting person/organization	University of South Florida
Title or numeric reference of the portion(s)	ALUMINUM- α -HEMATITE THIN FILMS FOR PHOTOELECTROCHEMICAL APPLICATIONS
Title of the article or chapter the portion is from	ALUMINUM- α -HEMATITE THIN FILMS FOR PHOTOELECTROCHEMICAL APPLICATIONS
Editor of portion(s)	N/A
Author of portion(s)	HUSSEIN ALROBEI
Volume of serial or monograph	N/A
Page range of portion	
Publication date of portion	2017
Rights for	Main product
Duration of use	Life of current edition
Creation of copies for the disabled	no
With minor editing privileges	no
For distribution to	United States
In the following language(s)	Original language of publication
With incidental promotional use	no
Lifetime unit quantity of new product	Up to 499
Title	Critical Investigation of Photo-semiconducting Material for Water Splitting Applications
Instructor name	n/a
Institution name	n/a
Expected presentation date	Dec 2018

<https://s100.copyright.com/AppDispatchServlet> 1/2

The copyright permission for chapter 4 is below.

5/10/2018 permission to use my published paper (AJAC) in my Dissertation - alrobei@mail.usf.edu - University of South Florida Mail

 Ma

Move to inbox More 9 of about 95

COMPOSE

Inbox (4,120)
Starred
Important
Sent Mail
Drafts (75)
Categories
More

Hussein Alrobei <alrobei@mail.usf.edu> Apr 18
to ajac

Hello

I am Hussein Alrobei, first author of my published journal in AJAC with title "A New Insight in the Physical and Photoelectrochemical Properties of Molybdenum Disulfide Nanocomposite Films" and I want to use this article including everything (figures, tables, text etc.) in my Ph.D. dissertation.

I need copyright permission from you which I need to include in my appendix of my dissertation report for allowing me to use this article completely.

thanks

ajac@scirp.org Apr 18
to me

Dear Hussein Alrobei,

Thank you for the email.

You can use the paper as appendix in your dissertation. Please add proper citation in the paper.

Best Regards
Martina MA
Managing Editor
QQ: 2489977548
Skype: marina1220@hotmail.com
American Journal of Analytical Chemistry

<https://mail.google.com/mail/u/1/#search/Ma/162d97e8bfeed276>

1/1

The copyright permission for chapter 6 is below.

5/14/2018

Rightslink® by Copyright Clearance Center



RightsLink®

Home

Account Info

Help



Title: p-n Based Photoelectrochemical Device for Water Splitting Application Alpha-Hematite (α -Fe₂O₃)-Titanium Dioxide (tio₂) as N-Electrode

Logged in as:
HUSSEIN ALROBEI
Account #:
3001284122

LOGOUT

Author: Hussein Alrobei, Hye Young Lee, Ashok Kumar, Manoj K. Ram

Publication: MRS Advances

Publisher: Cambridge University Press

Date: Mar 20, 2018

Copyright © COPYRIGHT: © Materials Research Society 2018

Order Completed

Thank you for your order.

This Agreement between 17921 TROPICAL COVE DR ("You") and Cambridge University Press ("Cambridge University Press") consists of your license details and the terms and conditions provided by Cambridge University Press and Copyright Clearance Center.

Your confirmation email will contain your order number for future reference.

[printable details](#)

License Number	4347931153878
License date	May 14, 2018
Licensed Content Publisher	Cambridge University Press
Licensed Content Publication	MRS Advances
Licensed Content Title	p-n Based Photoelectrochemical Device for Water Splitting Application Alpha-Hematite (α -Fe ₂ O ₃)-Titanium Dioxide (tio ₂) as N-Electrode
Licensed Content Author	Hussein Alrobei, Hye Young Lee, Ashok Kumar, Manoj K. Ram
Licensed Content Date	Mar 20, 2018
Licensed Content Volume	3
Licensed Content Issue	13
Start page	697
End page	706
Type of Use	Dissertation/Thesis
Requestor type	Author
Portion	Full article
Author of this Cambridge University Press article	Yes
Author / editor of the new work	Yes
Order reference number	
Territory for reuse	World
Title of your thesis / dissertation	Critical Investigation of Photo-semiconducting Material for Water Splitting Applications
Expected completion date	Dec 2018
Estimated size(pages)	1
Attachment	
Requestor Location	17921 TROPICAL COVE DR 17921 TROPICAL COVE DR

<https://s100.copyright.com/AppDispatchServlet>

1/2

APPENDIX B: COPYRIGHT PERMISSIONS FOR FIGURES

The copyright permission for figure 2.2 is below.

5/8/2018 Rights and Permissions | PNAS

☰ ⚙️ 🔍

Proceedings of the
National Academy of Sciences
of the United States of America

NEW RESEARCH IN

Physical Sciences ▾

Social Sciences ▾

Biological Sciences ▾

Rights and Permissions

← About

The author(s) retains copyright to individual PNAS articles, and the National Academy of Sciences of the United States of America (NAS) holds copyright to the collective work and retains an exclusive License to Publish these articles, except for open access articles submitted beginning September 2017. For such open access articles, NAS retains a nonexclusive License to Publish, and these articles are distributed under a CC BY-NC-ND license.

For volumes 106–114 (2009–September 2017), the author(s) retains copyright to individual articles, and NAS retains an exclusive License to Publish these articles and holds copyright to the collective work. Volumes 90–105 (1993–2008) are copyright National Academy of Sciences. For volumes 1–89 (1915–1992), the author(s) retains copyright to individual articles, and NAS holds copyright to the collective work.

<http://www.pnas.org/page/about/rights-permissions>

1/5

The copyright permission for figure 2.3 is below.

5/14/2018 RightsLink® by Copyright Clearance Center

 **Copyright Clearance Center** **RightsLink®** [Home](#) [Account Info](#) [Help](#) 



Title: Towards highly efficient photoanodes: boosting sunlight-driven semiconductor nanomaterials for water oxidation

Author: Jiayong Gan, Xihong Lu, Yexiang Tong

Publication: Nanoscale

Publisher: Royal Society of Chemistry

Date: May 5, 2014

Copyright © 2014, Royal Society of Chemistry

Logged in as: HUSSEIN ALROBEI
Account #: 3001284122
[LOGOUT](#)

Order Completed

Thank you for your order.

This Agreement between 17921 TROPICAL COVE DR ("You") and Royal Society of Chemistry ("Royal Society of Chemistry") consists of your license details and the terms and conditions provided by Royal Society of Chemistry and Copyright Clearance Center.

Your confirmation email will contain your order number for future reference.

[printable details](#)

License Number	4347950885238
License date	May 14, 2018
Licensed Content Publisher	Royal Society of Chemistry
Licensed Content Publication	Nanoscale
Licensed Content Title	Towards highly efficient photoanodes: boosting sunlight-driven semiconductor nanomaterials for water oxidation
Licensed Content Author	Jiayong Gan, Xihong Lu, Yexiang Tong
Licensed Content Date	May 5, 2014
Licensed Content Volume	6
Licensed Content Issue	13
Type of Use	Thesis/Dissertation
Requestor type	academic/educational
Portion	figures/tables/images
Number of figures/tables/images	1
Distribution quantity	50
Format	print and electronic
Will you be translating?	no
Order reference number	
Title of the thesis/dissertation	Critical Investigation of Photo-semiconducting Material for Water Splitting Applications
Expected completion date	Dec 2018
Estimated size	1
Attachment	
Requestor Location	17921 TROPICAL COVE DR 17921 TROPICAL COVE DR TAMPA, FL 33647

<https://s100.copyright.com/AppDispatchServlet>

1/2

The copyright permission for figure 2.5 is below.

5/14/2018

Rightslink® by Copyright Clearance Center



RightsLink®

Home

Account Info

Help



Title: Using hematite for photoelectrochemical water splitting: a review of current progress and challenges

Author: Andebet Gedamu Tamirat, John Rick, Amare Aregahegn Dubale, Wei-Nien Su, Bing-Joe Hwang

Publication: Nanoscale Horizons

Publisher: Royal Society of Chemistry

Date: Feb 4, 2016

Copyright © 2016, Royal Society of Chemistry

Logged in as:
HUSSEIN ALROBEI
Account #:
3001284122

LOGOUT

Order Completed

Thank you for your order.

This Agreement between 17921 TROPICAL COVE DR ("You") and Royal Society of Chemistry ("Royal Society of Chemistry") consists of your license details and the terms and conditions provided by Royal Society of Chemistry and Copyright Clearance Center.

Your confirmation email will contain your order number for future reference.

[printable details](#)

License Number	4347951453619
License date	May 14, 2018
Licensed Content Publisher	Royal Society of Chemistry
Licensed Content Publication	Nanoscale Horizons
Licensed Content Title	Using hematite for photoelectrochemical water splitting: a review of current progress and challenges
Licensed Content Author	Andebet Gedamu Tamirat, John Rick, Amare Aregahegn Dubale, Wei-Nien Su, Bing-Joe Hwang
Licensed Content Date	Feb 4, 2016
Licensed Content Volume	1
Licensed Content Issue	4
Type of Use	Thesis/Dissertation
Requestor type	academic/educational
Portion	figures/tables/images
Number of figures/tables/images	1
Distribution quantity	50
Format	print and electronic
Will you be translating?	no
Order reference number	
Title of the thesis/dissertation	Critical Investigation of Photo-semiconducting Material for Water Splitting Applications
Expected completion date	Dec 2018
Estimated size	1
Attachment	
Requestor Location	17921 TROPICAL COVE DR 17921 TROPICAL COVE DR TAMPA, FL 33647

<https://s100.copyright.com/AppDispatchServlet>

1/2

The copyright permission for figure 2.6 and 2.7 is below.

5/8/2018

Creative Commons — Attribution 3.0 Unported — CC BY 3.0



Creative Commons License Deed

Attribution 3.0 Unported (CC BY 3.0)



This is a human-readable summary of (and not a substitute for) the [license](#).

You are free to:

Share — copy and redistribute the material in any medium or format

Adapt — remix, transform, and build upon the material

for any purpose, even commercially.

The licensor cannot revoke these freedoms as long as you follow the license terms.

Under the following terms:

Attribution — You must give appropriate credit, provide a link to the license, and indicate if changes were made. You may do so in any reasonable manner, but not in any way that suggests the licensor endorses you or your use.

No additional restrictions — You may not apply legal terms or technological measures that legally restrict others from doing anything the license permits.

Notices:

You do not have to comply with the license for elements of the material in the public domain or where your use is permitted by an applicable exception or limitation.

<https://creativecommons.org/licenses/by/3.0/>

1/2

The copyright permission for figure 2.8 is below.

5/8/2018 RightsLink® by Copyright Clearance Center

Copyright Clearance Center RightsLink®

Home Account Info Help



Title: Synthesis, characterization and photocatalytic application of α -Fe₂O₃ microflower
Author: M. Alagiri, Sharifah Bee Abdul Hamid
Publication: Materials Letters
Publisher: Elsevier
Date: 1 December 2014
Copyright © 2014 Elsevier B.V. All rights reserved.

Logged in as: HUSSEIN ALROBEI
Account #: 3001284122
LOGOUT

Order Completed

Thank you for your order.

This Agreement between 17921 TROPICAL COVE DR ("You") and Elsevier ("Elsevier") consists of your license details and the terms and conditions provided by Elsevier and Copyright Clearance Center.

Your confirmation email will contain your order number for future reference.

[printable details](#)

License Number	4344341150760
License date	May 08, 2018
Licensed Content Publisher	Elsevier
Licensed Content Publication	Materials Letters
Licensed Content Title	Synthesis, characterization and photocatalytic application of α -Fe ₂ O ₃ microflower
Licensed Content Author	M. Alagiri, Sharifah Bee Abdul Hamid
Licensed Content Date	Dec 1, 2014
Licensed Content Volume	136
Licensed Content Issue	n/a
Licensed Content Pages	4
Type of Use	reuse in a thesis/dissertation
Portion	figures/tables/illustrations
Number of figures/tables/illustrations	1
Format	both print and electronic
Are you the author of this Elsevier article?	No
Will you be translating?	No
Original figure numbers	figure 2

<https://s100.copyright.com/AppDispatchServlet>

1/2

The copyright permission for figure 2.9 is below.

5/10/2018 Rightslink® by Copyright Clearance Center

 **RightsLink®** [Home](#) [Create Account](#) [Help](#) 

 **ACS Publications** Most Trusted. Most Cited. Most Read. **Title:** Magnetite Colloidal Nanocrystals: A Facile Pathway To Prepare Mesoporous Hematite Thin Films for Photoelectrochemical Water Splitting

Author: Ricardo H. Gonçalves, Bruno H. R. Lima, Edson R. Leite

Publication: Journal of the American Chemical Society

Publisher: American Chemical Society

Date: Apr 1, 2011

Copyright © 2011, American Chemical Society

LOGIN

If you're a [copyright.com](#) user, you can login to RightsLink using your copyright.com credentials.

Already a [RightsLink](#) user or want to [learn more?](#)

PERMISSION/LICENSE IS GRANTED FOR YOUR ORDER AT NO CHARGE



This type of permission/license, instead of the standard Terms & Conditions, is sent to you because no fee is being charged for your order. Please note the following:


- Permission is granted for your request in both print and electronic formats, and translations.
- If figures and/or tables were requested, they may be adapted or used in part.
- Please print this page for your records and send a copy of it to your publisher/graduate school.
- Appropriate credit for the requested material should be given as follows: "Reprinted (adapted) with permission from (COMPLETE REFERENCE CITATION). Copyright (YEAR) American Chemical Society." Insert appropriate information in place of the capitalized words.
- One-time permission is granted only for the use specified in your request. No additional uses are granted (such as derivative works or other editions). For any other uses, please submit a new request.

If credit is given to another source for the material you requested, permission must be obtained from that source.

The copyright permission for figure 2.10 is below.

5/8/2018 Rightslink® by Copyright Clearance Center

 **Copyright Clearance Center** **RightsLink®** [Home](#) [Account Info](#) [Help](#) 

 **ELSEVIER**

Title: Control of the shape and size of iron oxide (α -Fe₂O₃) nanoparticles synthesized through the chemical precipitation method

Author: Abdelmajid Lassoued, Brahim Dkhil, Abdellatif Gadri, Salah Ammar

Publication: Results in Physics

Publisher: Elsevier

Date: 2017

© 2017 The Authors. Published by Elsevier B.V.

Logged in as: HUSSEIN ALROBEI
Account #: 3001284122
[LOGOUT](#)

Creative Commons Attribution-NonCommercial-No Derivatives License (CC BY NC ND)

This article is published under the terms of the [Creative Commons Attribution-NonCommercial-No Derivatives License \(CC BY NC ND\)](#).

For non-commercial purposes you may copy and distribute the article, use portions or extracts from the article in other works, and text or data mine the article, provided you do not alter or modify the article without permission from Elsevier. You may also create adaptations of the article for your own personal use only, but not distribute these to others. You must give appropriate credit to the original work, together with a link to the formal publication through the relevant DOI, and a link to the Creative Commons user license above. If changes are permitted, you must indicate if any changes are made but not in any way that suggests the licensor endorses you or your use of the work.

Permission is not required for this non-commercial use. For commercial use please continue to request permission via Rightslink.

[BACK](#)

[CLOSE WINDOW](#)

Copyright © 2018 [Copyright Clearance Center, Inc.](#) All Rights Reserved. [Privacy statement](#). [Terms and Conditions](#).
Comments? We would like to hear from you. E-mail us at customerscare@copyright.com

The copyright permission for figure 2.11 and figure 12 is below.

5/8/2018 Rightslink® by Copyright Clearance Center

 **Copyright Clearance Center** **RightsLink®**

[Home](#) [Account Info](#) [Help](#) 

SPRINGER NATURE

Title: Efficient growth of aligned SnO₂ nanorod arrays on hematite (α-Fe₂O₃) nanotube arrays for photoelectrochemical and photocatalytic applications

Author: Gao Yue, Hongwei Ni, Rongsheng Chen et al

Publication: Journal of Materials Science: Materials in Electronics

Publisher: Springer Nature

Date: Jan 1, 2013

Copyright © 2013, Springer Nature

Logged in as: HUSSEIN ALROBEI
Account #: 3001284122
[Logout](#)

Order Completed

Thank you for your order.

This Agreement between 17921 TROPICAL COVE DR ("You") and Springer Nature ("Springer Nature") consists of your license details and the terms and conditions provided by Springer Nature and Copyright Clearance Center.

Your confirmation email will contain your order number for future reference.

[printable details](#)

License Number	4344340444880
License date	May 08, 2018
Licensed Content Publisher	Springer Nature
Licensed Content Publication	Journal of Materials Science: Materials in Electronics
Licensed Content Title	Efficient growth of aligned SnO ₂ nanorod arrays on hematite (α-Fe ₂ O ₃) nanotube arrays for photoelectrochemical and photocatalytic applications
Licensed Content Author	Gao Yue, Hongwei Ni, Rongsheng Chen et al
Licensed Content Date	Jan 1, 2013
Licensed Content Volume	24
Licensed Content Issue	9
Type of Use	Thesis/Dissertation
Requestor type	academic/university or research institute
Format	print and electronic
Portion	figures/tables/illustrations
Number of	2

<https://s100.copyright.com/AppDispatchServlet>

1/2

The copyright permission for figure 2.13 is below.

5/10/2018 RightsLink® by Copyright Clearance Center

 **Copyright Clearance Center** RightsLink® [Home](#) [Create Account](#) [Help](#) 

 **ACS Publications** Most Trusted. Most Cited. Most Read.

Title: General Strategy for Doping Impurities (Ge, Si, Mn, Sn, Ti) in Hematite Nanocrystals

Author: Jun Liu, Changhao Liang, Hemin Zhang, et al

Publication: The Journal of Physical Chemistry C

Publisher: American Chemical Society

Date: Mar 1, 2012

Copyright © 2012, American Chemical Society

LOGIN

If you're a [copyright.com](#) user, you can login to RightsLink using your [copyright.com](#) credentials.

Already a [RightsLink](#) user or want to [learn more?](#)

PERMISSION/LICENSE IS GRANTED FOR YOUR ORDER AT NO CHARGE

This type of permission/license, instead of the standard Terms & Conditions, is sent to you because no fee is being charged for your order. Please note the following:

- Permission is granted for your request in both print and electronic formats, and translations.
- If figures and/or tables were requested, they may be adapted or used in part.
- Please print this page for your records and send a copy of it to your publisher/graduate school.
- Appropriate credit for the requested material should be given as follows: "Reprinted (adapted) with permission from (COMPLETE REFERENCE CITATION). Copyright (YEAR) American Chemical Society." Insert appropriate information in place of the capitalized words.
- One-time permission is granted only for the use specified in your request. No additional uses are granted (such as derivative works or other editions). For any other uses, please submit a new request.

If credit is given to another source for the material you requested, permission must be obtained from that source.

[BACK](#)

[CLOSE WINDOW](#)

Copyright © 2018 [Copyright Clearance Center, Inc.](#) All Rights Reserved. [Privacy statement](#). [Terms and Conditions](#).
Comments? We would like to hear from you. E-mail us at customer-care@copyright.com

<https://s100.copyright.com/AppDispatchServlet>

1/2

The copyright permission for figure 2.14 is below.

5/8/2018 Rightslink® by Copyright Clearance Center

Copyright Clearance Center RightsLink® Home Account Info Help



Title: Fabrication of 3D quasi-hierarchical Z-scheme RGO-Fe₂O₃-MoS₂ nanoheterostructures for highly enhanced visible-light-driven photocatalytic degradation

Author: Lixia Chen, Fang He, Naiqin Zhao, Ruisong Guo

Publication: Applied Surface Science

Publisher: Elsevier

Date: 31 October 2017

© 2017 Elsevier B.V. All rights reserved.

Logged in as: HUSSEIN ALROBEI
Account #: 3001284122
LOGOUT

Order Completed

Thank you for your order.

This Agreement between 17921 TROPICAL COVE DR ("You") and Elsevier ("Elsevier") consists of your license details and the terms and conditions provided by Elsevier and Copyright Clearance Center.

Your confirmation email will contain your order number for future reference.

[printable details](#)

License Number	4344321502165
License date	May 08, 2018
Licensed Content Publisher	Elsevier
Licensed Content Publication	Applied Surface Science
Licensed Content Title	Fabrication of 3D quasi-hierarchical Z-scheme RGO-Fe ₂ O ₃ -MoS ₂ nanoheterostructures for highly enhanced visible-light-driven photocatalytic degradation
Licensed Content Author	Lixia Chen, Fang He, Naiqin Zhao, Ruisong Guo
Licensed Content Date	Oct 31, 2017
Licensed Content Volume	420
Licensed Content Issue	n/a
Licensed Content Pages	12
Type of Use	reuse in a thesis/dissertation
Portion	figures/tables/illustrations
Number of figures/tables/illustrations	2
Format	both print and electronic

<https://s100.copyright.com/AppDispatchServlet>

1/2

+

The copyright permission for figure 2.15 is below.

5/8/2018

Rightslink® by Copyright Clearance Center

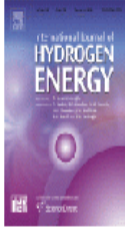


RightsLink®

Home

Account Info

Help



Title: Zn-doped hematite modified by graphene-like WS₂: A p-type semiconductor hybrid photocathode for water splitting to produce hydrogen

Author: Dongmei Chu, Kezhen Li, Aijuan Liu, Jie Huang, Chunyong Zhang, Ping Yang, Yukou Du, Cheng Lu

Publication: International Journal of Hydrogen Energy

Publisher: Elsevier

Date: 12 April 2018

© 2018 Hydrogen Energy Publications LLC. Published by Elsevier Ltd. All rights reserved.

Logged in as:
HUSSEIN ALROBEI
Account #:
3001284122

LOGOUT

Order Completed

Thank you for your order.

This Agreement between 17921 TROPICAL COVE DR ("You") and Elsevier ("Elsevier") consists of your license details and the terms and conditions provided by Elsevier and Copyright Clearance Center.

Your confirmation email will contain your order number for future reference.

[Printable details](#)

License Number	4344330212906
License date	May 08, 2018
Licensed Content Publisher	Elsevier
Licensed Content Publication	International Journal of Hydrogen Energy
Licensed Content Title	Zn-doped hematite modified by graphene-like WS ₂ : A p-type semiconductor hybrid photocathode for water splitting to produce hydrogen
Licensed Content Author	Dongmei Chu, Kezhen Li, Aijuan Liu, Jie Huang, Chunyong Zhang, Ping Yang, Yukou Du, Cheng Lu
Licensed Content Date	Apr 12, 2018
Licensed Content Volume	43
Licensed Content Issue	15
Licensed Content Pages	10
Type of Use	reuse in a thesis/dissertation
Portion	figures/tables/illustrations

<https://s100.copyright.com/AppDispatchServlet>

1/2